8-9-2019

Advanced data analytic methodology for quality improvement in additive manufacturing

Mojtaba Khanzadehdaghalian

Advanced data analytic methodology for quality improvement in additive manufacturing

By

Mojtaba Khanzadehdaghalian

A Dissertation
Submitted to the Faculty of
Mississippi State University
in Partial Fulfillment of the Requirements
for the Degree of Doctor of Philosophy
in Industrial and Systems Engineering
in the Department of Industrial and Systems Engineering

Mississippi State, Mississippi

August 2019

Advanced data analytic methodology for quality improvement in additive manufacturing

By

Mojtaba Khanzadehdaghalian

Approved:

_____

Linkan Bian
(Major Professor/Graduate Coordinator)

_____

Jonathan R. Woody
(Committee Member)

_____

Kamran Paynabar
(Committee Member)

_____

Wenmeng (Meg) Tian
(Committee Member)

_____

Mohammad Marufuzzaman
(Committee Member)

_____

Jason M. Keith
Dean
Bagley College of Engineering

Name: Mojtaba Khanzadehdaghalian

Date of Degree: August 9, 2019

Institution: Mississippi State University

Major Field: Industrial and Systems Engineering

Major Professor: Linkan Bian

Title of Study: Advanced data analytic methodology for quality improvement in additive manufacturing

Pages in Study: 164

Candidate for Degree of Doctor of Philosophy

One of the major challenges of implementing additive manufacturing (AM) processes for the purpose of production is the lack of understanding of its underlying process-structure-property relationship. Parts manufactured using AM technologies may be too inconsistent and unreliable to meet the stringent requirements for many industrial applications. The first objective of the present research is to characterize the underlying thermo-physical dynamics of AM process, captured by melt pool signals, and predict porosity during the build. Herein, we propose a novel porosity prediction method based on the temperature distribution of the top surface of the melt pool as the AM part is being built. Advance data analytic and machine learning methods are then used to further analyze the 2D melt pool image streams to identify the patterns of melt pool images and its relationship to porosity.

Furthermore, the lack of geometric accuracy of AM parts is a major barrier preventing its use in mission-critical applications. Hence, the second objective of this work is to quantify the geometric deviations of additively manufactured parts from a large data set of laser-scanned coordinates using an unsupervised machine learning approach. The outcomes of this research are: 1)

quantifying the link between process conditions and geometric accuracy; and 2) significantly reducing the amount of point cloud data required for characterizing of geometric accuracy.

DEDICATION

This dissertation work is dedicated to my parents, Hossein Khanzadeh, and Sakineh Bordbar, who have been constant sources of love and encouragement in my entire life.

ACKNOWLEDGEMENTS

I would like to thank individuals who helped me during the preparation of this dissertation work. First and foremost, I am thankful to Dr. Linkan Bian, the chair of my Ph.D. Committee, whose guidance and trust lead me through almost four years of research that created this dissertation. In addition, I would like to thank the other Ph.D. Committee members, Dr. Kamran Paynabar, Dr. Mohammad Marufuzzaman, Dr. Jonothan Woody and Dr. Wenmeng Tian, whose comments and questions always opened new horizon of concepts.

I am grateful to Dr. Mark A. Tschopp for his comments' and supports in drafting and publishing Chapter II and III.

TABLE OF CONTENTS

LIST OF TABLES

LIST OF FIGURES

CHAPTER I

INTRODUCTION

1.1 Introduction

The recent decades have witnessed a rapid growth in metal additive manufacturing (AM) processes for functional parts production within many industrial sectors (such as aerospace, tooling, and biomedical applications [1]). According to the most recent Wohlers' report, the sale of AM systems and corresponding services is projected to reach 5.5 billion USD by the year 2019 [2]. Ranging from customized to large-scale manufacturing, AM parts manifest unique geometries and functionally-graded, or custom-tailored structures with light weight that can be impractical or burdensome for traditional manufacturing processes [3]. Despite of the advancements of AM in non-structural applications, the lack of understanding of its fundamental process-structure-property relationship is identified as a primary hurdle for industrial adoption of metal AM systems [3-7].

The inadvertent defects of Additive Manufacturing (AM) parts result in low repeatability of AM products. One of the more detrimental microstructural properties associated with AM is porosity within final parts. The existing methods of defect detection/characterization mainly rely on *post-manufacturing* methods, such as X-ray computed tomography (CT), ultrasonic inspection, and many more. However, these post-manufacturing techniques are extremely expensive and time-consuming. Hence, improving the quality and repeatability of additively manufactured parts is essential to fulfill the demanding requirements and certification constraints for applications with high quality requirements such as healthcare and aerospace. Therefore, there is an imperative need

to develop methods for online detection/control of defects during the build. Establishing a quantitative relationship between the characteristics of melt pools and the formation of porosity in the as-built parts during the fabrication provide a rational solution to this predicament.

Besides, AM enables the fabrication of complex geometry parts for a broad range of materials including metals, ceramics, and polymers [6, 8-10]. However, AM parts are afflicted by low geometric accuracy and poor surface integrity. The poor geometry of AM parts prevents their use in industries, where precision is important [6]. The prevalent approach for quantifying the geometric accuracy of Additively Manufactured (AM) parts is to assess critical geometric dimensioning and tolerance (GD&T) characteristics, such as flatness, cylindricity, circularity, and more [11] based on several sample points (tens to hundreds) taken on certain part features.

In Chapter 2, we present an *in-situ* signal processing methodology for characterizing the thermo-physical dynamics of directed energy deposition (DED) melt pool signals, which can be used to further predict process anomalies during the build. We propose an imaging processing method, based on functional data analysis, to characterize the thermal distribution of the top surface of the melt pool. Subsequently, we correlate the extracted melt pool characteristics to the locations of pores based on a Self-Organizing Map (SOM) clustering algorithm. Furthermore, we propose a methodology to quantify the geometric deviations of additively manufactured parts from a large data set of laser-scanned coordinates. This is an important research area; recent developments in non-destructive scanning techniques, such as laser, structured light, and computer tomography engender point-by-point coordinate measurements of AM parts. These techniques can generate millions of coordinate points (three-dimensional (3D) point cloud). However, new analytical methods for quantifying the geometric accuracy of AM parts from these large scan datasets are required. Accordingly, the objective of this work is to use an unsupervised machine

learning (ML) algorithm called self-organizing map (SOM) to overcome this open research challenge.

With the motivation of gaining beneficial insights about the significance of melt pool thermal characteristics in detection of anomalies, we extended our study in Chapter 2 to investigate the relationship between the melt pool characteristics and the defect occurrence in an as-built additive manufacturing part in Chapter 3. In Chapter 3, supervised learning methods are utilized to identify the patterns of melt pool images and build a black-box model for the probability distribution of class labels (namely, porosity) based on data characteristics of predictors (e.g., melt pool characteristics). The resultant model does not depend on specific design of specimens with varying material properties; and can be effectively developed as long as thermal-porosity data can be obtained.

In Chapter 4, the research objective is to develop an online monitoring technique to quickly detect and diagnose anomalies during the build of AM parts. Based on the features extracted from thermal image streams using multilinear principal component analysis (MPCA), we propose a dual statistical process monitoring approach, which combines image feature extraction and dimension reduction methods to identify the local defects/anomalies (i.e., porosity) in AM processes. Ultimately in chapter 5, we develop an efficient thermal history prediction of AM processes in a layer-wise manner using thermal image streams, which can subsequently be used to characterize the microstructure and mechanical properties of the AM parts. Most of the existing physics-based models are not able to provide comprehensive understanding of AM processes, hence we utilize a prediction model to establish a layer-wise relationship in the thermal history of the AM part. We propose a network-tensor structure for freeform shapes created in direct laser deposition processes. Subsequently, solving the equations for network-tensor structure of freeform shapes based on the

input and output flow for each node leads to tensor regression model. Generalized multilinear framework, called higher-order partial least squares (HOPLS) is used to estimate the parameters of tensor regression model. The proposed approach can precisely calculate the high-dimensional thermal history of parts in a computationally efficient manner. Last, chapter 6 discusses the conclusions and the potential directions for future research.

CHAPTER II

IN-SITU MONITORING OF MELT POOL IMAGES FOR POROSITY PREDICTION IN DIRECT ENERGY DEPOSITION PROCESSES

2.1 Introduction: Unsupervised learning of melt pool signals

Our objective is to develop an *in-situ* signal processing methodology for characterizing the thermo-physical dynamics of directed energy deposition (DED) melt pool signals, which can be used to further predict process anomalies during the build. Metallic AM parts are now used as functional parts within many industrial sectors such as tooling, dental, medical, and aerospace. This popularity is driven by virtue of its unique feature of generating complex-shaped, functionally-graded or custom-tailored parts that can be utilized for a variety of engineering and industrial applications [12]. According to the most recent Wohlers' report, the sale of AM systems and corresponding services is projected to reach 5.5 billion USD by the year 2019 [2]. Although AM has experienced tremendous growth and success in non-structural applications, variations in the quality and mechanical properties of AM parts, due to the presence of defects, can limit its use in load bearing or mission-critical applications. Mission-critical application refers to the applications of manufactured parts where tough performance standards and requirements must be fulfilled before they can be used in real world.

The existence of porosity is a major quality issue for AM parts. A few of the hypothesized causes of porosity in parts are the rapid solidification of AM parts, entrapped gas, incomplete powder melting, and lack of fusion [5, 6]. The existing approaches for porosity detection are based on x-ray computed tomography (CT), ultrasonic scanning, and other **post-manufacturing**

characterization, which can be expensive and time-consuming. Considering all these, the next generation AM monitoring/control system needs the capability for *in-situ* monitoring and predicting process defects via analysis of process signals [13].

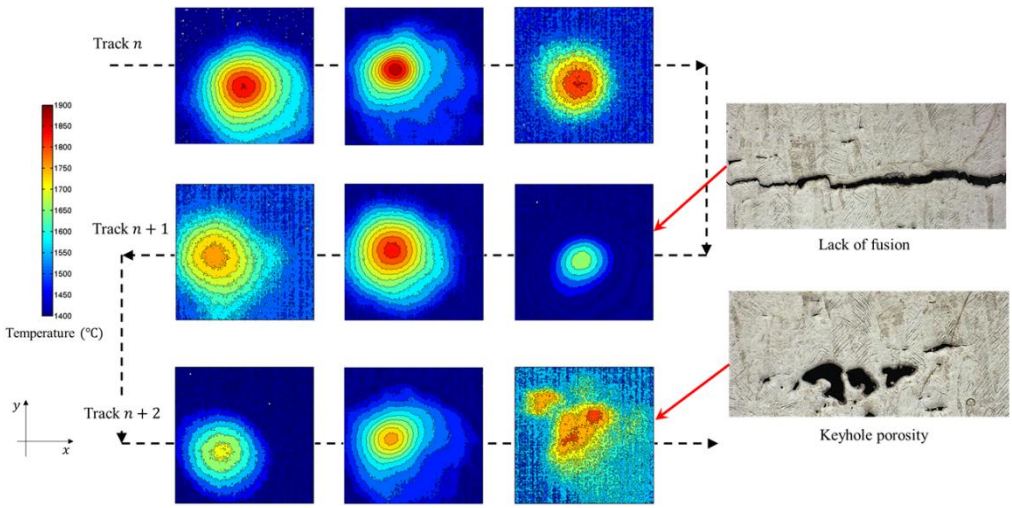

Figure 2.1 Relationship between melt pool characteristics and porosity. The image colors represent the temperature of melt pool in ℃.

The melt pool, or otherwise referred to as molten pool, is the region of superheated molten metal in proximity to the laser/material interface- typically in the form of a spherically shaped droplet that moves at the traverse speed [6]. Melt pool is the initiation of the solidified part, its morphology and thermal distribution are eminent indicators of the fabricated part microstructure, and thus final quality. Figure 2.1 demonstrates the potential relationship between characteristics of melt pool images and porosity, based on experimental data generated by the Additive Manufacturing Laboratory at Mississippi State University. When the thermal distribution of melt pools exhibit abnormal behaviors, various types of pores may be generated. Melt pool behaviors are directly related to formation of porosity in the parts. For instance, the fundamental origin of lack-of-fusion porosity is caused by insufficient overlap of successive melt pools. Moreover, the

key-hole effect results from generating a deep V-shape melt pool and vaporizing elements within the melt pool, which can cause gas/vapor to get trapped as porosity within the material. Once the melt pool behaviors are correlated to the porosity of fabricated parts, control/correction actions can be taken to reduce the porosity during the build. Extracting the melt pool characteristics and correlating the extracted features to microstructure anomalies will lead to real-time, non-destructive detection of part defects. Most of the existing studies for modeling the time-varying melt pool can be broadly categorized into two groups: (1) characterizing melt pool based on the morphological characteristics and (2) capturing melt pool thermal characteristics. The former group of studies focus on capturing the changes in the size, length, depth, area, and other geometric features of melt pools during the build (see [14, 15]), whereas the latter focuses on the temperature measurements over the melt pool, such as peak temperature, average temperature, etc.(see [16, 17]). Most of these methods are developed based on physics-based differential equations that govern the underlying thermo-physical process [18, 19]. However, such methods may not accurately capture the uncertainty associated with the process, and the resulting simulated thermal history tends to deviate from reality [20].

There is an urgent need for developing an efficient methodology for extracting features based on thermal imaging data streams during the actual build of parts that can be used to signal the formation of porosity. We propose an imaging processing method, based on functional data analysis, to characterize the thermal distribution of the top surface of the melt pool. Note that characterization of melt pool signals is challenging because of large data volume, low signal-to-noise ratio, ill-structured data (e.g., different melt pools varying in sizes), and missing data measurements. To address these challenges, we apply a spherical transformation and convert melt pool thermal distributions with different sizes/shapes to temperature measurements with the

identical support in the spherical domain. The reason of using a spherical transformation of the data instead of other transformations is that the position of melt pool in our study is specified by three numbers, the radial distance of that point from a fixed origin that denotes its temperature, and it's polar and azimuth angle that define the pixels of melt pool images. Hence, spherical transformation is a suitable option to convert melt pool thermal distributions with different sizes/shapes to temperature measurements with identical support in the spherical domain. Subsequently, smoothing techniques, such as bi-harmonic transformation, is applied to convert discrete temperature measurements to continuous functions, so that missing data measurements can be estimated. The bi-harmonic transformation has been widely used for the interpolation of 3-D discrete data with irregular boundary conditions [21-23]. We further correlate the extracted melt pool characteristics to the locations of pores based on a Self-Organizing Map (SOM) clustering algorithm. We focus on abnormal melt pool behaviors satisfying either of the two key assumptions: (1) the thermal distribution of melt pool causing porosity tends to exhibit different characteristics from other normal melt pools; or (2) the number of abnormal melt pools is small compared to normal melt pools. The output of SOM groups the melt pool images into clusters based on similarity of thermal distributions. The melt pools belonging to groups dissimilar to the others tend to cause outliers of microstructure, such as mini-cracks and pores as shown in Figure 2.1. We validate our method by comparing the predicted locations of pores based on the melt pool temperature distribution and the actual locations of pores obtained via x-ray tomography scanning. Results show high prediction accuracy and low false alarm rate. One key issue is that, the thermal images/history are related to porosity in the fabricated part in this study. For instance, if superheated or low input energy melt pools are observed during the build, corrective actions can be performed before the next layer is built on. This identification reduces product cost as the

percentage of product waste will significantly decrease. Note that the choice of process variables is not explicitly considered to link with the thermal history/images. It can be argued that different set of process variables can also have a significant effect on thermal history. Nevertheless, it is beyond the scope of this study and will be investigated in future studies. However, a number of studies are available in literature for investigating the control procedure for correcting defects and stabilizing the temperature distribution. Interested readers can read the work by Mireles et al. [24] and Kruth et al. [25] for more information.

Section 1.2 provides a detailed literature review on the existing porosity detection techniques as well as on the characterization of melt pool characteristics.

2.2 Review on melt pool characterization and porosity detection

We survey the papers pertaining to melt pool monitoring and characterization as well as the existing porosity detection techniques. This section is divided into two subsections: (1) methods for porosity characterization, and (2) melt pool monitoring and modeling.

2.2.1 Literature on porosity characterization

2.2.1.1 Porosity prediction techniques based on post-manufacturing characterization

Ultrasonic and x-ray computed tomography have been used extensively for porosity detection in materials such as stones [26], ceramic materials [27], and so forth. Ultrasonic methods are primarily used for analyzing the porous structure, mechanical strength, and to detect internal defects such as voids, cracks, delaminations, etc.[28-32].

Three different ultrasonic approaches have been applied by Eren et al. [27] for characterizing porosity as well as for detection and imaging of different types of defect in ceramic materials. Air-coupled ultrasound can be implemented for non-contact detection and the imaging of defects in ceramic tiles despite having a relatively high impedance of ceramic materials.

Frequency dependence of attenuation can be used for the quantification of porosity, which is an important practical task in the ceramic industry. One interesting finding of this study is that, measurements of ultrasonic wave velocity have been found to be reliable tool for the characterization of porosity in ceramic materials. Through experiments, the authors have observed that 5% porosity change in ceramic tiles results in about 20% reduction of ultrasonic wave velocity. However, the accuracy of ultrasonic characterization of porosity is sensitive to the selective layers of samples. It is thus not capable of capturing pores between two consecutive sampled layers.

The majority of studies on porosity detection focus on post-manufacturing characterization using x-ray computed tomography. Among the studies that discuss x-ray tomography, Kowaluk and Wozniak [33] investigate the measurement of pore volume in cast aluminum using a METROTOM 800 Carl Zeiss computer tomography system. The benefits of using flash thermography against other approaches such as ultrasonic attenuation estimation have been discussed by Meola and Toscano [34], where the authors' state that through flash thermography a part can be inspected while viewing the smooth or the rough side indifferently. It is non-contact, cost-effective, and fast. Wells [35] has showed x-ray computer tomography modality using advanced Volume Graphics StudioMax (VGSM) voxel analysis and visualization software for 3-D defect characterization, analysis, and visualization. Defects of interest in this study are primarily porosity and some inclusions with a total defect level is 1.11% of the total casting volume. Cai et al. [36] propose an x-ray computed tomography method that involves image enhancement and ring artifact removal before image segmentation. By using x-ray computed tomography, the authors investigate the effect of process parameters on material porosity. Moreover, the obtained results are compared with conventional Archimedes testing method and experimental results show the superiority of x-ray computed tomography.

The *limitation* of the post-manufacturing characterization approaches is that they are usually expensive and time-consuming. The accuracy of ultrasonic characterization depends on the selected layers of inspection. Moreover, post-manufacturing characterization of porosity does not leverage the unique, layer-by-layer building mechanism of additive manufacturing that allows for in-process correction/control of defects before the next layer is built.

2.2.1.2 Visual based porosity detection techniques

Visual based porosity detection techniques refer to the detection of anomalies while building the part, which allows to take steps to correct them in real time. Tajeripour and Ershad [26] propose an approach for porosity detection in stones by using enhanced version of local binary pattern features. In this approach, a threshold is calculated from porosity-free images during training phase. Using this threshold value, porosities are detected from the test images. Schwerdtfeger et al. [37] investigate the possibility of *in-situ* anomaly detection for powder bed, beam based AM process. Ti-6Al-4V parts have been built in a selective electron beam melting system and during the fabrication of the parts, a number of infrared (IR) images are taken of different layers. Similarly, metallographic images of the same layers are taken from destructive material investigation. The authors have observed good correlation between the patterns visible in IR images and metallographic images. This correlation specifies that regions with higher heat radiation (lighter color in images) corresponds to an anomaly in the part. Every anomaly visible in the IR images have also been found in the metallographic images. This provides a unique procedure for *in-situ* quality control for selective electron beam melting system as anomalies can be repaired in real time using appropriate repair methods such as re-melting of the compromised area or a combination of additional powder deposition and re-melting of the compromised area. Fan et al. [38] propose an image processing methodology and uses optical system design to develop

an online surface defect detection system. They also develop an analysis algorithm for auto defect classification technique. This algorithm removes noise from porous images, detects object edges, and uses hybrid-based method to determine the defects (i.e., crevice, scratch, broken corner, and dent) in the parts. From the experiments conducted in this study, authors have found the maximum miss rate can be controlled to less than 5.65%. Clijsters et. al [39] have developed an *in-situ* monitoring system on the Selective Laser Melting (SLM) that consists of a photodiode and a near-infrared thermal camera coupled with the data capturing and processing system. This set-up enables the user to log morphological data of melt pool that are used to classify vectors into different zones of varying heat flow situation and/or parameter sets. The effectiveness of this method is validated using experimental data after manufacturing Ti-6Al-4V, AlSi10Mg, and NiTinol parts.

The *limitation* of visual-based detection of porosity is that they are usually applied to detect pores with large sizes (e.g., diameter at the scale of hundreds of microns). The detection accuracy tends to be low for the detection of pores with small/medium sizes. Most of the visual-based detection approaches are based-on the images obtained from IR cameras, the accuracy of which is subject to emissivity and reflection. Extra efforts are required for the purpose of calibration.

2.2.2 Melt pool monitoring and modeling

A number of studies are available in literature that discuss melt pool modeling in DED with varying degree of detail. For instance, closed form equations have been developed by Hunt to map material solidification boundaries by leveraging multiple solidification parameters and material composition [40]. Although this classical approach was originally developed for metal casting, Kobryn et al. have shown that the maps are capable of predicting the microstructure obtained in Ti-6Al-4V via a laser AM process[41, 42]. Gockel et al. have expanded on Hunt's curves to

produce solidification morphology curves for Ti-6Al-4V in the process parameter space [43]. Furthermore, Gockel et al. have compared their results with a previously-developed process map for melt pool geometry that shows that maintaining a constant melt pool cross sectional area yields a constant grain size. Additionally, the grain morphology boundaries have been found similar to curves of constant melt pool aspect ratio. Khairallah et al. [44] have developed a mesoscopic model to investigate how the strong dynamical melt flow generates pore defects, material spattering (sparking), and denudation zones using the ALE3D multi physics code. Surface tension, Marangoni effect, and recoil pressure are incorporated in the model. The study also explains in detail how three kinds of pore defects (depression collapse, lateral pores, open and trapped pores) are generated and discusses strategies to avoid them. Shiomi et al. [45] have developed a finite element model to calculate the weight of the solidified part made of metallic powder. Authors have reconstructed meshes after each heating cycle by several laser pulses and have assumed the physical properties to be independent of temperature. Experimental and simulated results have showed that the amount of the solidified part after a pulse is affected by the peak power of the laser rather than the duration of laser irradiation. Hu and Kovacevic [46] have developed a three-dimensional (3-D) heat transfer model using ANSYS in order to study the thermal behavior of the melt pool in building a single-bead stainless steel wall via a closed loop-controlled LBPD process. The model provides the magnitude of laser power required to maintain a constant molten pool width.

On the other hand, Boddu et al. [47] have presented a review of control of laser cladding for rapid prototyping. Authors have demonstrated that dimensional analysis can be used as a modeling tool for predicting deposited layer thickness in direct metal deposition technique. Apparatus with a laser light source has been used by Vetter et al.[48] in a study of the laser cladding

parameters. This study has identified the position of phase changes in the powder, but has not explicitly measured powder concentrations, inferring the position of the maximum concentration from power transmission along the axis. Nassar et al. [49] and Siddique et al. [50] both have presented defect location and pore size data that is measured using XCT with optical cross-sectional metallography. Nassar et al. [49] have compared their data to another method of *in-situ* defect detection using optical emission spectroscopy. On the other hand, Siddique et al. have critiqued the two methods demonstrated by Nassar et al. [51] where authors have identified that due to the lack of significant difference between the techniques, the XCT data must be favored due to its non-destructive nature. However, a discrepancy between data sets is observed if XCT data is chosen and the acquisition process is substantially more expensive compared to cross-sectional optical microscopy. Ding et al. [52] provide a solution to the challenges of process reliability and the repeatability of finished components by developing a sensing and control system for the robotically controlled 8-axis Laser-based direct metal addition (LBDMA) system. It comprises sensing and control units for the powder flow rate (via optoelectronic sensor) and the melt pool size. Moreover, an infrared imaging setup is installed on the laser head to monitor the top full-field view of the melt pool. To build a closed-loop control system for achieving a uniform melt pool size, a simple proportional integral derivative (PID) controller coupled with feed-forward compensation is used. A thermo-mechanical model of directed energy deposition AM for Ti-6Al-4V is developed by Heigel et al. [53] that utilizes measurements of the surface convection generated by gasses flowing during the deposition. More specifically, this work emphasizes on having a detailed knowledge of the surface heat transfer to produce more accurate finite element analysis (FEA) results. Moreover, an additional model is proposed that uses the assumption of free

convection on all surfaces. Numerical results show that a measurement-based convection model is required to generate error free simulation results.

2.2.2.1 Melt pool characterization based on morphological characteristics

Among the methods that focus on melt pool morphological features (e.g., size, length, area, etc.), Birnbaum et al. have investigated the issues related to control of melt pool size in LBAM based on a process map approach that relate process parameters to the melt pool size in LBAM [54]. Also, Qi et al. have investigated various morphological features of melt pool and studied physical phenomena related to melt pool. They have proposed a model for motion of melt pool's free surface in uninterrupted cladding, and finally they have benchmarked their findings against practical results according to melt pool's width, length, and the height of solidified cladding track [15]. Similar approaches can be found in [14, 18]. Ahn et al. [55] have proposed a novel method for evaluating the characteristic length of the melt pool. The efficacy of two evaluation methods are analyzed and the method using the gap between the two centers of neighboring scans is experimentally found to be more efficient due to the averaging effect. Wang et al. have taken a unique approach where they have developed a physics-based multivariable model for directed energy deposition. Using the same conceptual framework provided by Doumanidis and Kwak [56], these authors have parameterized the material transfer rate in the deposition as a function of the process operating parameters. This in turn has improved the characterization of the interdependence between melt pool height and laser power[57]. Clijsters et. al. [39] have developed an *in-situ* monitoring system on the Selective Laser Melting (SLM) that leverage morphological features such as melt pool area, length, width, and intensity. Li et al. [58] provide a comparative study of the laser AM of Inconel 718 using the pulsed-wave and continuous-wave laser modes by both simulations and experiments. A three dimensional (3-D) numerical model is

developed and investigated to simulate the transient melt pool motion, heat transfer, and fluid flow for pulsed-wave laser AM. There are two essential findings of the study: (1) that simulated single track melt pool geometries and average temperatures under both laser modes are in good agreement with measured results in the study and (2) that the solidification front in the pulsed-wave case is about 15˚ more tilted to the laser scanning direction compared to the continuous-wave case. The result is finally compared with a relative steady value in the continuous-wave case, a periodic fluctuation of temperature pulsed-wave with the same frequency of the laser pulse in the pulsed-wave case.

2.2.2.2 Melt pool monitoring based on thermal characteristics

Another stream of research utilize the thermal characteristics for the purpose of monitoring and control closed-loop control [17]. Chandrasekhar et al. apply IR-thermal images of weld pool to find a smart method to model the weld beams' penetration. More specifically, authors in this study develop hybrid intelligent models combining image processing with soft computing techniques such as adaptive neuro fuzzy inference system and artificial neural network for estimating the weld bead width and the depth of penetration from the thermal image of the weld pool [16]. Bi et al. have investigated the deposition of thin walls with constant laser power and different process control strategies. They have primarily focused on the emitted signals of melt pool from IR-temperature, and have found that both the size and temperature of the melt pool influence the dimensional accuracy of the deposited sample. The authors have concluded that these signals can be used for closed-loop and part quality control as well as for process monitoring [59]. Hua et al. have investigated the effects of laser processing parameters on the temperature of melt pool. The investigation output is the relationship between melt pool and thickness of cladding layer [12]. They also discuss the relationship between the molten pool and the thickness of cladding

layer that results in a scheme to achieve *in-situ* accurate control for the layer thickness. This is achieved by using an analytical model based on temperature measurement of the molten pool. Song et al. apply hybrid control system to reinforce the quality and precision of geometrically complex parts in accordance with melt pool temperature. The cladding height controller developed in this study is a rule-based controller whereas the melt pool temperature controller is a generalized predictive controller with input constraints. These two controllers are connected in series with the height controller given a higher priority compared to the temperature controller [60]. Picasso and Hoadley [19] present a Finite Element Method (FEM) to analyze effects of powder injection and thermocapillary on melt pool shape and fluid movement.

The *limitation* of the existing melt pool models is that they are primarily developed based on deterministic physics-based differential equations. These equations don't capture the variations and uncertainty associated with the underlying thermo-physical process during the build, and thus tend to deviate from the reality. The existing melt pool monitoring/modeling approaches focus on simple metrics, such as the size, length, peak temperature, and others. There is a lack of comprehensive characterization for the distribution of temperature over the melt pool top surface. As a result, the extracted features may be limited. Porosity prediction based on such simple metrics may not be accurate.

In summary, the technical contributions of this study to the existing literature are as follows:

- We develop a novel methodology to investigate thermal-porosity relationship from a data mining perspective. This work is significant since the existing approaches for porosity detection mainly rely on post-manufacturing approaches, which can be expensive and time-

consuming. More importantly, post-manufacturing characterization does not allow for the detection and correction of porosity during the build, resulting in lower product quality.

- We develop a novel data processing procedure that converts each thermal image to a function, which can be processed using advanced statistical analysis tools. Compared to the existing literature that mainly utilize simple metrics of the melt pool, our proposed study provides a new tool for leveraging the comprehensive thermal distribution.
- The proposed methodology is among the handful of studies available in literature that provides a theoretical foundation for qualification and certification of AM products via temperature distribution of the melt pool.

2.3 Modeling of melt pool thermal images

2.3.1 Characteristics of melt pool image data

We focus on modeling the thermal image data streams obtained during the fabrication of parts using a Laser Engineering Net Shaping (LENS) system. LENS is a means to build metallic prototypes/parts by combining the material and energy delivery for simultaneous deposition and part forming. LENS does not rely on a pre-deposited layer of metallic powder, and thus may be used as a means to repair or coat parts via cladding. In addition, due to the combined material/energy delivery method, LENS can be readily utilized for creating functional graded/composed parts with varying material/alloy concentrations. Finally, preform mixing can be accomplished with LENS – such as coaxial powder delivery [6].

Melt pool images are captured, in real time, using a high-resolution Stratonics ThermaViz multi-sensor system, including a two-wavelength imaging pyrometer for melt pool monitoring and an IR thermal imaging sensor for global heat flow monitoring. The data is recorded in an image format where each pixel corresponds to a discrete measurement of melt pool temperature. An

example of the melt pool image is shown in Figure 2.2. Figure 2.3 shows the scatter plot of temperature measurements.

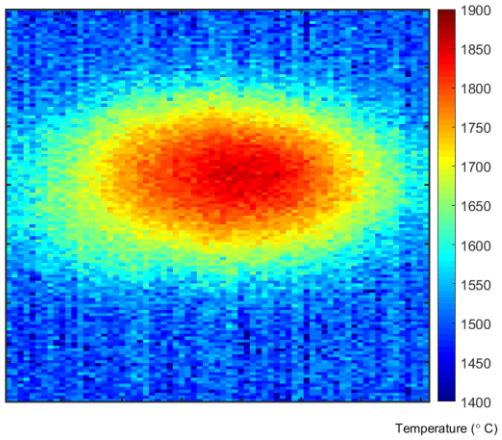

Figure 2.2 The contour plot of melt pool in pixels.

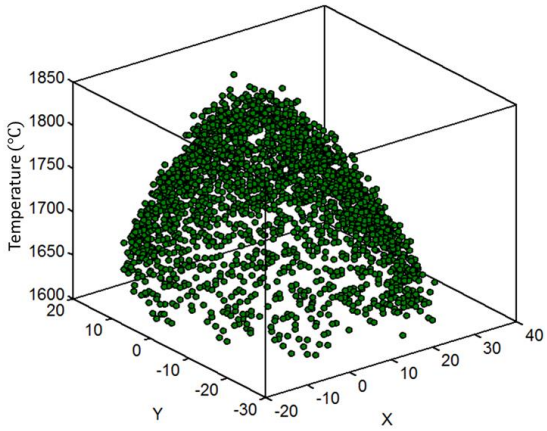

Figure 2.3 Thermal distribution of the top surface of the melt pool.

The width and depth of the melt pool are expected to affect porosity caused by lack of fusion. The area of the melt pool may also affect the concentration of porosity caused by oxides. The melt pool depth is also crucial to the thickness of deposited layers, the microstructure evolution, and the pore formation. High layer thickness tends to result in lack of fusion between

successive layers and adjacent tracks. This has been studied by Tang et al. [61], Cunningham et al. [62], Dilip et al. [63] and many more. More specifically, Cunningham et al. [62] and Dilip et al. [63] demonstrate that melt pool width and depth have significant impact on the formation of porosity in the fabricated part. Cunningham et al. show that the ratio of hatch spacing to melt pool width can be important. Too small a ratio can induce keyhole porosity, even if power and velocity values are not sufficient to induce keyhole porosity by itself. However, too large a ratio can yield lack of fusion porosity due to fluctuations in melt pool dimensions, even in cases where the overlap depth would otherwise be sufficient. On the other hand, Dilip et al. [63] focus on the evolution of single-track melt pools and porosity in parts made using SLM of alloy Ti-6Al-4V. The single-track deposits are made using varying laser power and scan speeds, and their effects on the melt pool morphology are studied. Microstructural studies on the melt pool cross-section show that at a low power level and high scan speed the width of the track reduces, gradually becomes discontinuous, and eventually results in balling. The depth of penetration of the melt pool is observed to increase with the lower scan speed. At higher power levels, in some cases a keyhole effect is observed. Figure 2.1 shows the formation of pores due to different melt pool characteristics. The quantitative thermal-porosity relationship is essential to identifying operation conditions and in-process control/diagnosis of AM processes for better part quality [6, 43, 64].

Processing and modeling the thermal image data is very challenging: (1) The thermal imaging system generates a tremendous amount of data. A small single track thin wall may result in over 10 GB of thermal image data. (2) The signal-to-noise level is so low that the boundary of the melt pool is not clear in the thermal images, as shown Figure 2.2. (3) The size and center of melt pools vary during the build. Extra efforts are needed to align the melt pools and account for various melt pool sizes. (4) Temperature measurements may be missing during data acquisition.

2.3.2 Modeling the thermal distribution of melt pools

We propose a modeling procedure that converts melt thermal images to continuous temperature models with the identical function support. Image processing is applied to extract temperature distribution of top surface of each melt pool from the captured melt pool images. Extracted data points are converted to spherical coordinates. Subsequently, a non-parametric surface interpolation method is implemented on the extracted temperature distribution of the top surface of each melt pool. The resulting continuous temperature models with identical function supports will be used as input for melt pool clustering in Section 1.4. The details of the melt pool modeling are shown below.

Data rescaling. Data captured by the system contains, a columns and b rows which is determined the resolution of captured image. We denote the row and column by X and Y, respectively, where (X, Y) represents coordinates in the melt pool image that correspond to temperature measurement T(X, Y). The melting temperature is denoted by T_γ , which is pre-specified according to material properties. The points (X, Y) with temperatures greater than T_γ are extracted. The resulting temperature measurements define the region of the melt pool surface, i.e., $M = \{(X,Y): T(X,Y) \geq T_\gamma\}$.

Next, we rescale the data within the melt pool according to the melting temperature T_γ and peak temperature, denoted by T_{max}. Assume that the coordinates of the peak temperature is denoted by (X_p, Y_p). We define the range of temperature by $R=T_{max}-T_\gamma$ for the melt pool. We centralize the melt pool shape in peak temperature and also scale temperature between 0 and 1 (Eq. 2.1).

$$(X^c, Y^c, T^s) = (X - X_p, Y - Y_p, \frac{T-T_\gamma}{R}) \text{ for } (X,Y) \in M \quad (2.1)$$

Here, c represents centralized melt pool in peak temperature and s accounts for scaled temperature to the interval between 0 and 1.

Spherical transformation. To apply to the tool of functional data analysis, we convert the triplet of (X^c, Y^c, T^s) to the spherical domain (θ, φ, ρ), where θ and φ represent the angles within the X-Y plane, and the T-XY plane, respectively. ρ represents the radius. The mathematical expressions of the spherical transformation, denoted by s, is shown below:

$$(\theta, \varphi, \rho) = s(X^c, Y^c, T^s) =$$

$$\left(arctan\left(\frac{Y^c}{X^c}\right), arccos\left(\frac{T^s}{\sqrt{(X^c)^2+(Y^c)^2+(T^s)^2}}\right), \sqrt{(X^c)^2 + (Y^c)^2 + (T^s)^2}\right) \quad (2.2)$$

The visualization of the temperature distribution of the top surface of the melt pool boundary with spherical coordinates is shown in Figure 2.4. Once the spherical transformation is applied, all temperature measurements are converted to function values defined in the region of $(\theta, \varphi) \in [-\pi, \pi] \times [0, \frac{\pi}{2}]$.

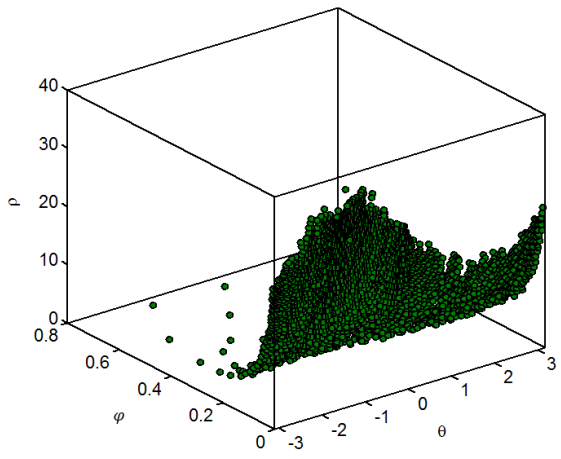

Figure 2.4 Plot of the temperature distribution at the top surface of the melt pool in spherical coordinates.

Interpolation via bi-harmonic surface interpolation method. The bi-harmonic surface fitting method is applied for data interpolation and smoothing, which converts the discrete data points to a continuous function as shown in Figure 2.5. Subsequently, an equally spaced grid (e.g., 50×50) on (θ, φ) is defined to obtain discretized measurements of the melt pool temperature.

The proposed data processing procedure transforms melt pool thermal images, containing missing values and ill-structured data, to standardized vectors of temperature measurements of the same length and defined on the identical function support, denoted by $\mathbf{m_i}$ for i=1,…,N. In the next section, the Self-Organizing Map (SOM) clustering algorithm is applied to $\mathbf{m_i}$'s to identify the anomalies of melt pools by capturing the similarity and dissimilarity.

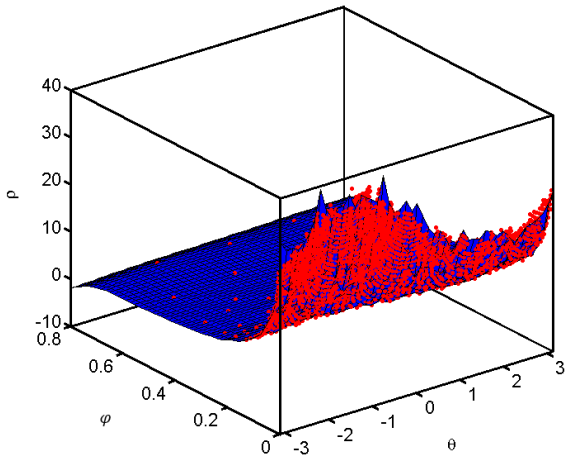

Figure 2.5 Plot of the interpolated temperature distribution of the melt pool using the bi-harmonic surface interpolation method in spherical coordinates.

2.4 Porosity prediction using SOM clustering

We apply a SOM model with size z× z to the set of standardized melt pool vectors **M** = $\{\mathbf{m_i} : i= 1,\ldots, N\}$ obtained in the previous section. SOM is a type of an unsupervised machine

learning neutral network that uses a procedure called competitive learning to discern patterns [65]. The SOM maps high-dimensional input data into a 2-D space, while preserving the topological interrelationship between data. Note that the mapping does not change the relative distance or similarity among data points [66]. The clustered data reduces the dimensionality and intuitively characterizes the similarity among data points. In essence, the method works best for unsupervised learning tasks and its superiority lies in its visual presentation of the data. Since we have multidimensional data, which dimensions need to be reduced as well as similarity among them need to be captured and characterized, SOM is the perfect fit for this study. Note that SOM has been used as a linking step between image data pre-processing and porosity prediction. Moreover, in this study leveraging the SOM maps, a correlation matrix is created based on the centroid vector that identifies the level of correlation with each cluster to all the others. Afterwards, the correlation and the number of melt pools in each cluster determine whether the cluster consists normal or abnormal melt pools.

The SOM clustering outputs z^2 clusters with the center of each cluster as well as melt pools belonging to each cluster. The algorithm provides a brief overview the SOM algorithm. More detailed discussion can be found in [67, 68].

Algorithm. Melt pool clustering via SOM

Input data. Set of interpolated features $\mathbf{M} = \{\mathbf{m_i} : i= 1,\ldots, N\}$

Steps.

Initialization. At iteration e=0, randomly generate a weight coefficient vector for each cluster using a uniform distribution. The resulting weight coefficient vectors, at iteration e=0, are denoted by $\mathbf{w}_j(0)$ for $j=1,\ldots, z^2$. We also specify a decreasing, non-

negative learning rate function $\alpha(e)$, which controls the convergence of the SOM algorithm.

Model training.

For each iteration e, update weight coefficient vectors $\mathbf{w}_j(0)$'s according to Steps 1-5 below.

1. Randomly sample a melt pool thermal vector $\mathbf{m_i}$ from the thermal data set **M** without replacement.

2. Calculate the Euclidean distance between $\mathbf{m_i}$ and all weight coefficient vectors $\mathbf{w}_j(e)$ as shown below:

$$\delta_j = \left|\left|\mathbf{m_i} - w_j(e)\right|\right| \qquad j = 1, \ldots, z^2 \tag{2.3}$$

3. Choose the best matching cluster by minimizing distance δ_j. That is, $\delta_{j^*} = \min_{j=1,\ldots,z^2} \delta_j$, where j^* is the index of the best matching cluster. The melt pool image represented by $\mathbf{m_i}$ is assigned to the best matching cluster j^*.

4. Update the weight coefficients in the neighborhood of cluster j^*, denoted by $V(j^*)$, according to the formula below

$$\mathbf{w}_j(e) \leftarrow \mathbf{w}_j(e) + \alpha(e)[\mathbf{m_i} - \mathbf{w}_j(e)] \; j \in V(j^*) \tag{2.4}$$

5. If all the melt pool vectors in **M** have been sampled, set $e \leftarrow e+1$. Otherwise, go to Step 1.

Stop when the vectors of weight coefficients converge. That is, $\mathbf{w}_j(e) \rightarrow \mathbf{w}_j$ for j=1,..., z^2. Specifically, the process is stopped if the absolute difference between the weight vector at iteration e+1 and e is small, typically less than 1% [69].

The output of SOM is a z× z 2D map that illustrates the number of melt pools in each cluster and the distance among adjacent clusters. Figure 2.6 provides an example of SOM hit map demonstrating the population size of each cluster. Figure 2.7 indicates neighbor weight distances among these clusters. The darker color in Figure 2.7 means cluster dissimilarity whereas lighter color means the opposite. We can also estimate the correlation between all the pairs of clusters.

$$\text{Corr} = \begin{bmatrix} d_{1,1} & \cdots & d_{1,z^2} \\ \vdots & \vdots & \vdots \\ d_{z^2,1} & \cdots & d_{z^2,z^2} \end{bmatrix}$$

where $d_{r,w} = \text{Corr}\left(w_i, w_j\right)$ for $i, j = 1,2,\cdots, z^2$. (2.5)

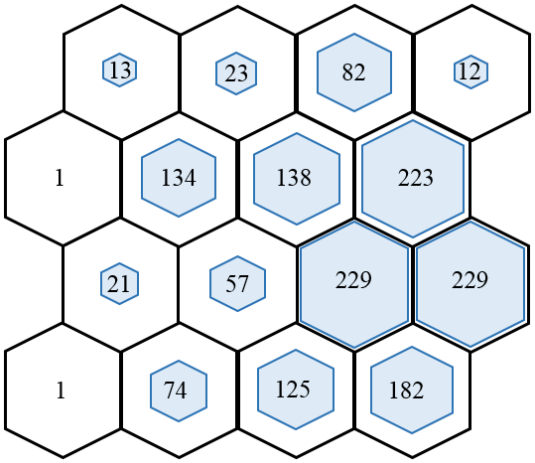

Figure 2.6 Self-organizing map for the proposed melt pool model, which includes mapping each melt pool profile into a different cluster.

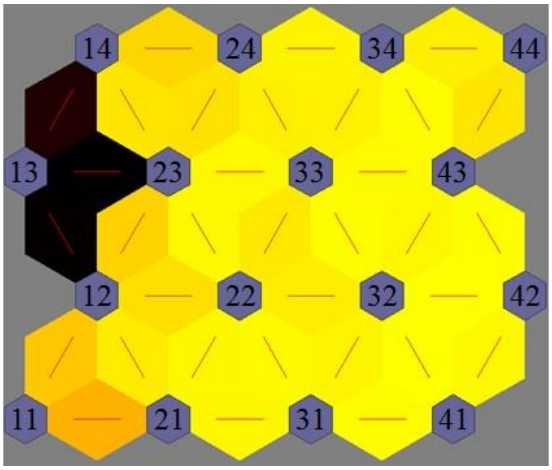

Figure 2.7 Weighting the distances between neighboring clusters.

An abnormal cluster satisfies two conditions: (1) it is not highly correlated with other clusters, and (2) the number of melt pools belonging to this cluster is low. We use the median value to characterize the correlation of a cluster to the others (the median of each row of the correlation matrix). We identify a cluster as an anomaly when its median correlation and the percentage of melt pools are low.

2.5 Case study

In this section, we aim to validate the accuracy of the proposed porosity prediction methodology based on melt pool anomalies. A single-track Ti-6Al-4V thin wall is built using an OPTOMEC Laser Engineered Net Shaping (LENS) 750 system with the thermal history recorded. The predicted distribution of porosity of the as-built part, based on melt pool characteristics, is compared to the results of x-ray CT characterization. We examine the accuracy of porosity prediction by investigating the percentage of pores successfully predicted based on melt pool clustering, as well as the false alarm rate by looking into the percentage of normal melt pools that are predicted to cause porosity. A discussion about the model selection of SOM is also provided to determine the size of SOM models.

2.5.1 Experimental set-up

OPTOMEC LENS 750 machine equipped 1 kW Nd:YAG laser, pyrometer and in-chamber thermal camera (Figure 2.8) is used to fabricate single track Ti-6Al-4V thin walls (Figure 2.9). LENS has become a popular means to accomplish powder-based Direct Laser Deposition (DLD) due to its capability of creating functionally graded materials [5]. Processing conditions of the LENS machine, used to manufacture the Ti-6Al-4V thin-wall, are provided in Table 2.1.

Table 2.1 LENS processing parameters for AM thin wall

Power	300 W	Substrate (stainless steel)	3.175 mm
Scan speed	30 rpm	Starting offset from substrate	130.391mm
Powder feed rate	0.9 rpm	Determination of layer thickness	0.508 mm
Determination of hatch spacing	0.508 mm	Nozzle diameter	0.889 mm

Figure 2.8 LENS machine used to fabricateTi-6Al-4V thin wall.

Figure 2.9 Fabricated Ti-6Al-4V thin wall using LENS machine.

The time-varying evolution of melt pool behaviors is captured by the built-in thermal imaging system, and then used to predict the porosity distribution based on melt pool clustering. A dual-wavelength pyrometer (Stratonics, Inc.) and an IR camera (Sierra-Olympic Technologies, Inc. Viento320) have been used to capture temperature distribution of the top surface and side view of the melt pool during manufacture (see Figure 2.10). Since we are using the information from top surface of the melt pool in this study, data obtained from only dual-wavelength pyrometer is used for porosity prediction. The advantage of using the pyrometer sensor is that it reduces the risk of motion blur since the pyrometer has a specified exposure time (2.0274ms) that occurs at a specified collection rate. The scan rate of the laser is 12.7 mm/s meaning that during the exposure time the build moves approximately at 26μm[70]. The IR camera is typically used to capture the characteristics of the melt pool from the side view. Hence, collecting melt pool data from IR camera and its calibration are not needed in this study. The pyrometer is mounted above the OPTOMEC LENS™ 750 machine, outside of the inert environment of the chamber and aligned so as to view down the laser shaft via a series of three, broadband metallic mirrors. A CMOS detector has been used in the pyrometer with array size and pixel pitch being 752×480 and 6.45μm, respectively. The temperature range in the pyrometer varies from 1000-2500°C. Exposure time

and pixel clock are set to be 2.0274 ms and 5 MHz, respectively. The nominal image collection rate of the pyrometer is approximately 6.4 Hz (see Figure2.10 (b)). The IR camera is oriented at approximately 45° with respect to the sides of the CNC stage and is tilted in such a way that the focal plane is rotated 10°from a line normal to the substrate. The thin wall is constructed at an orientation such that one of its sides was fully in-view by the IR camera. The nominal image collection rate of the IR camera is approximately 12.58 Hz. This allows for capturing the melt pool images in real time. Each melt pool image has a 1.7MB file size. Hence, with such high image resolution and monitoring frequency, a single thin-wall build (length = 47.81mm, height =27.56mm, thickness = 1.78mm) results in 4.7GB of image stream data [70].

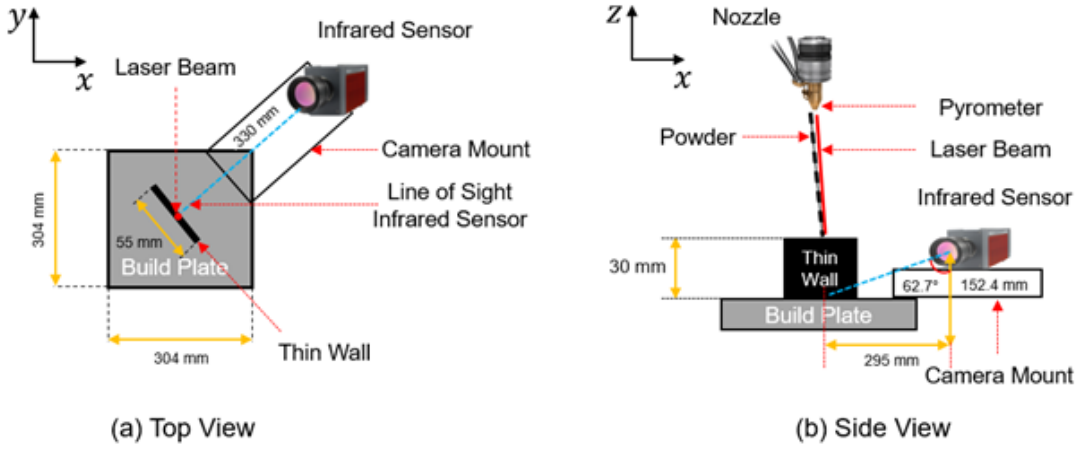

Figure 2.10 Images of (a) top view of IR camera and (b) side view of the pyrometer and their orientation with respect to the substrate and thin wall within the build chamber [70].

The microstructure is also characterized using x-ray CT, which captures numerous x-ray images around an axis of rotation and reconstructs a digital 3D model of the part. The CT method used in this study utilizes a full 3D cone of x-rays with a 2D detector. This cone beam scanner irradiates the part as it moves in a 360 ° circle around the part, acquiring data throughout the scan.

After the data are collected, a radon transform is applied to reconstruct using the acquired x-ray intensity readings for each of the detector elements. The individual slice images can then be accumulated into a 3D reconstruction [71]. Despite the long processing time, x-ray CT is capable of accurately identifying the sizes and locations of pores [72, 73]. Therefore, we use the outcomes of x-ray CT characterization as the benchmark of our prediction method. Moreover, Scanning Electron Microscopy (SEM) (FEG SEM Zeiss SUPRA™ 40) has been used to detect pore surfaces of the thin wall that are Au/Pd sputter-coated to determine the crack initiation sites and crack propagation characteristics. Instances of x-ray CT scan and SEM micrograph is provided in Figure 2.11.

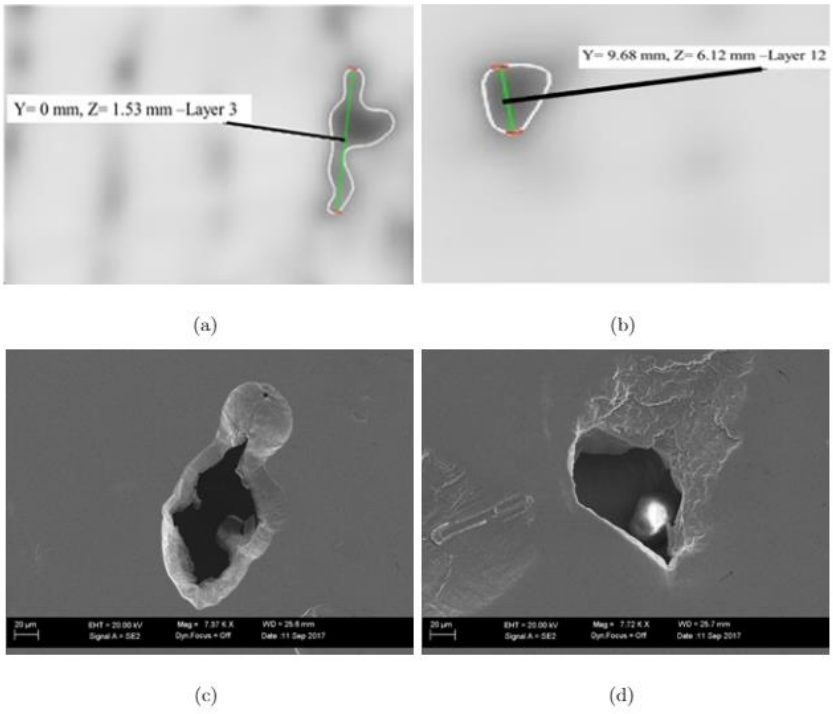

Figure 2.11 Illustrating instances of x-ray CT scan (a and b) and SEM micrograph (c and d).

2.5.2 Porosity prediction using melt pool temperature distribution characteristics

The thermal image data is processed and stored in N=1564 thermal image files, each of which contains 480×752 cells of information. In other words, N=1564 represents to the number of captured melt pools in thermal history of the thin wall. The area of the melt pool is extracted based on the melt pool temperature of Ti-6Al-4V (T_γ=1636 ℃). Each melt pool is centralized and scaled using the coordinates of the peak temperature. According to the data processing procedure described in the previous section, each melt pool image is converted to a continuous thermal distribution model defined in the spherical domain of $(\theta, \varphi) \in [-\pi, \pi] \times [0, \frac{\pi}{2}]$. SOM clustering is then applied to the resulting thermal distribution models to obtain the clusters of melt pools.

Recall that we assume that (1) an abnormal melt pool has low correlation with the others, or (2) the percentage of abnormal melt pool is much small compared with normal melt pools. Normal clusters should include a large number of melt pools that are similar to each other. We first examine the correlation between any two clusters represented by a correlation matrix. An example of the correlation matrix of a 4×4 SOM map is shown in Figure 2.12, which is a 16×16 symmetric matrix. The horizontal and vertical axes represent the labels of clusters. The red color represents higher correlation, whereas the blue color corresponds to lower correlation. A cluster with low correlation to the others is considered anomaly and porosity tends to occur at the corresponding locations. Cluster C21 demonstrates an example of normal melt pool cluster, which includes a large number of melt pools highly correlated with other clusters. On the other hand, cluster C13 and C44 have low correlations with the other clusters. A melt pool in cluster C13 shows higher temperature and irregular shape. Similar overheating is observed in the melt pool images belonging to cluster C44.

We calculate the median correlation of each clusters with the other clusters and percentage of melt pools belonging to each clusters. The results are summarized in Table 2.2. Clusters C13, C14, C24, and C44 have the lowest median values as well as the lowest percentage of melt pools. Also, the percentage of melt pools belonging to each of these clusters is below 1.5% of all melt pools. We also note that, although the median correlation between cluster C11 and the other is not low, this cluster includes one melt pool only with a percentage of 0.06%. This cluster is also considered as an anomaly because there is no other melt pool sharing similar characteristics. Low energy input is observed from melt pool images from cluster C11, which tends to results in lack of fusion. As a result, these five clusters are considered to be anomalies. The other clusters have relatively correlation (above 0.9) and include a larger number of melt pools; and thus considered normal.

Table 2.2 Cluster correlation and percentage of melt pool in each cluster in 4×4 SOM model.

Melt Pool Cluster	**C13**	**C44**	**C24**	**C14**	C34	**C11**	C33	C23
Median Correlation	**0.41**	**0.67**	**0.86**	**0.88**	0.93	**0.95**	0.97	0.97
Percentage of Melt Pool	**0.06**	**0.77**	**1.48**	**0.84**	5.28	**0.06**	8.88	8.62
Melt Pool Cluster	C43	C41	C31	C42	C21	C12	C22	C32
Median Correlation	0.97	0.97	0.98	0.98	0.98	0.98	0.99	0.99
Percentage of Melt Pool	14.35	11.71	8.04	14.74	4.76	1.35	3.67	14.74

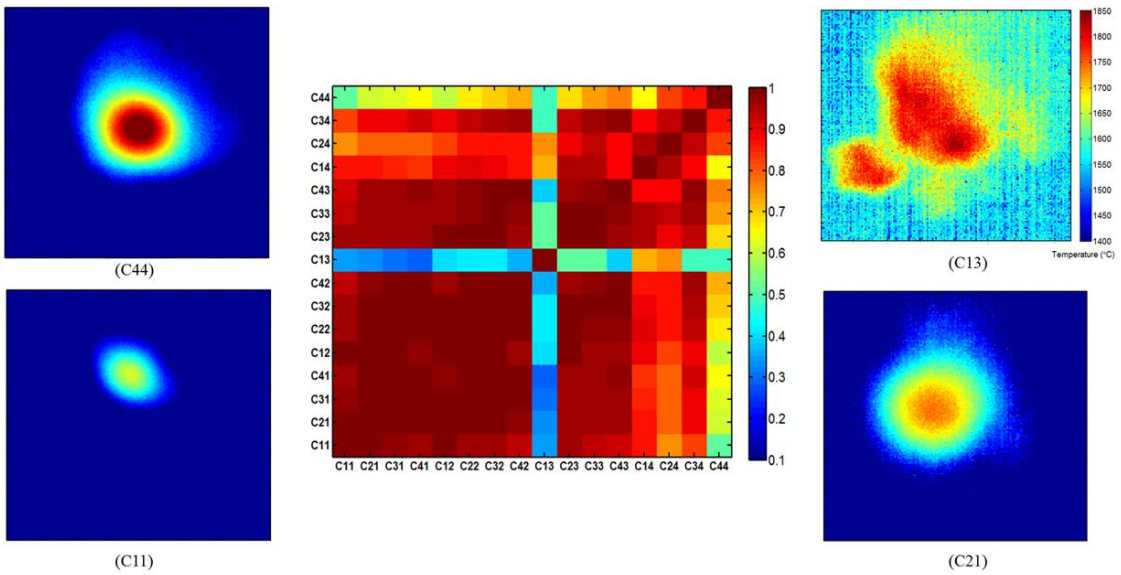

Figure 2.12 Correlation matrix (Cor) showing how pores were identified in the present methodology for the 16 clusters (Corr) of the 4×4 SOM map. Thermal profile images are shown with (C13, C44, and C11) are the porosity clusters (poor correlation with other melt pool profiles) and the (C21) regular melt pool (more normal melt pool profile).

The locations of predicted abnormal melt pools are compared to x-ray CT characterization, as shown in Figure 2.13. Each dot represents a pore characterized via x-ray CT and each square represents a pore predicted via the proposed melt pool based method. The size of the dot/square indicates the actual size of the pore, the diameter of which ranges from 0.05 mm to 0.93 mm. The x-ray CT characterization identifies a total of 51 pores in the thin wall build, 47 of which are successfully predicted based on our proposed melt pool clustering method using a 4× 4 SOM, resulting in a 92.16% prediction accuracy. Our prediction only results in 3 false alarms out of 1554 melt pools, resulting in a false alarm rate of 0.193%. In other words, only 3 melt pools out of 1554 are identified as anomalies without resulting in pores at the corresponding location. The false alarm may be partially attributed to the small sizes of potential pores that cannot be detected by x-ray CT used for characterization.

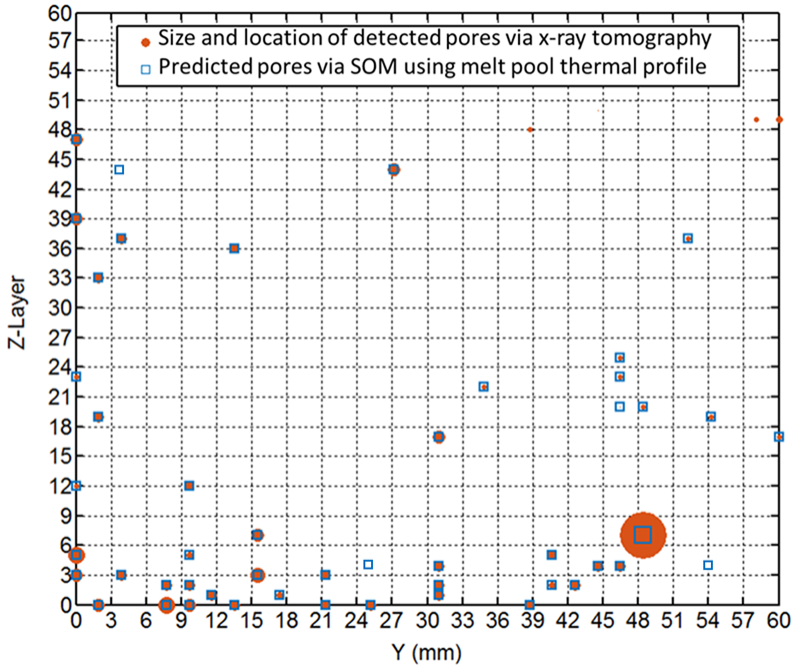

Figure 2.13 Plot of the various pores as a function of position within the AM thin wall. The predicted pores using the melt pool temperature distribution is shown against pores detected with x-ray tomography. The sizes of circle/square represent the sizes of pores.

We fabricated 9 additional samples to validate the efficiency of our proposed method as well as to show its generality. We employ the same methodology to those 9 thin walls, but here we only show an example of those parts. Results show that when the same methodology is applied with 4×4 model, it demonstrates the same behavior as before in detecting anomalies (see Figure 2.14 and Table 2.3). Highest percentage of abnormal melt pools in a single cluster is 1.33% for 4×4 SOM model whereas median of correlation is less than 0.9. This is similar to the results obtained in Table 2.2. However, results of SOM models for this thin wall could not be validated via x-ray tomography as it is expensive, time consuming, and often times not readily available. However, the pattern of SOM maps obtained through the proposed methodology for the new thin wall follows the same trend as observed for the original thin wall in the study. Hence, it can be stated that the developed methodology is suitable for different thin walls.

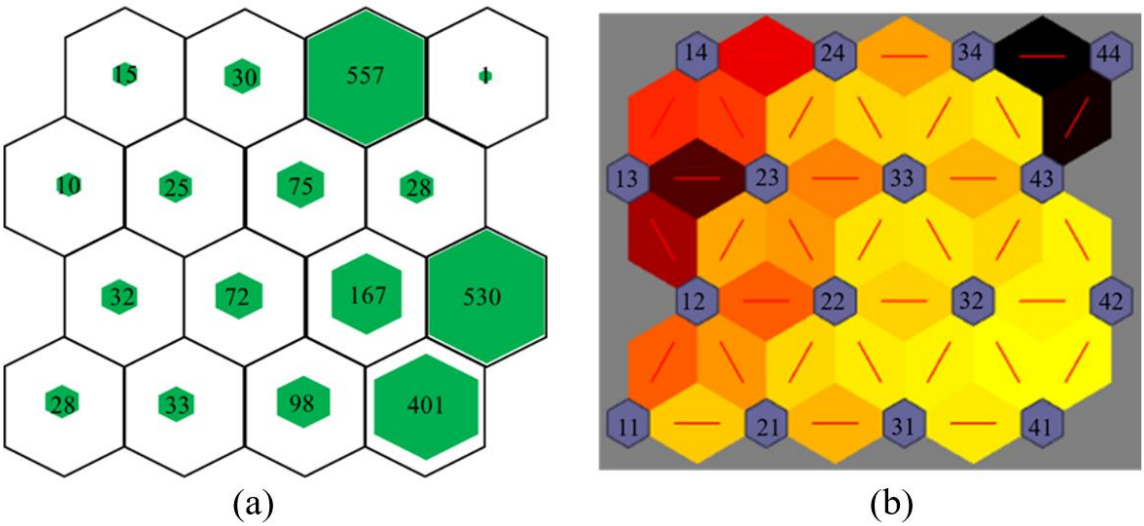

Figure 2.14 Self-organizing map of melt pool thermal profile for 4×4 model with new thin wall.

2.5.3 Model selection of SOM

We investigate various sizes of SOM models in terms of prediction accuracy and false alarm rate for 4×4, 5×5, 6×6, and 7×7 SOM models. The results are summarized in Table 2.4. With the same anomaly detection criteria, these four models result in 92.16%, 92.16%, 96.07%, and 80.39% prediction accuracy, coupled with 0.193%, 0.000%, 0.128%, and 0.000% false alarm rate, respectively. The 6×6 model results in the highest prediction accuracy of 96.07%. The prediction accuracy decreases with when the model size increases. The false alarm rate is generally low (less than 0.2% for all four models). As a result, we recommend to use a 5×5 or 6×6 model, which will further improve the performance of the porosity prediction as presented in Figure 2.13.

Table 2.3 Cluster correlation and percentage of melt pool in each cluster in 4×4 SOM model with new thin wall.

Melt Pool Cluster	**C44**	**C43**	**C13**	C11	C14	C12	C33	C24
Median Correlation	**0.35**	**0.88**	**0.88**	0.92	0.93	0.93	0.93	0.93
Percentage of Melt Pool	**0.05**	**0.48**	**1.33**	1.33	0.71	1.52	3.57	1.43
Melt Pool Cluster	C42	C43	C31	C34	C41	C21	C32	C22
Median Correlation	0.94	0.94	0.95	0.96	0.96	0.96	0.97	0.97
Percentage of Melt Pool	25.21	1.19	4.66	26.50	19.08	1.57	7.94	3.43

Table 2.4 Calculation of the pore detection accuracy rate and the false positive rate for melt pool temperature distribution.

SOM Model	Number of pores predicted accurately	Number of false positives	Pore detection accuracy rate	False positive rate
4×4	47	3	92.16	0.193
5×5	47	0	92.16	0.000
6×6	**49**	**2**	**96.07**	**0.128**
7×7	41	0	80.39	0.000
Number of actual pores				**51**
Number of melt pools in thermal history of thin wall				**1554**

2.6 Summary and conclusions

Inadvertent microstructure anomalies, such as porosity and mini-cracks, have detrimental effects on the mechanical properties of additively manufactured components. This hinders the wider adoption of AM technologies in strategic industrial sectors. We propose to predict porosity of as-built parts using the thermal distribution of melt pools during the build. Major findings of this study are summarized below:

1. Existing methods for porosity characterization mainly rely on post-manufacturing approaches, such as x-ray computed tomography or ultrasonic scanning, which can be expensive and time-consuming. More importantly, post-manufacturing characterization does not allow for the detection and correction of porosity during the build, resulting in lower product quality. We propose an *in-situ* monitoring tool for porosity prediction based on the similarity of melt pool thermal distributions. Our central hypothesis is that the similarities

among melt pools are directly correlated to the formation of pores in as-built parts. Thus, the anomalies of melt pool thermal distribution can be used as a process signature that signals the anomalies of microstructure.

2. Capturing the similarity among melt pool images is challenging due to different size/shape of melt pools, missing data measurements during data acquisition, and the tremendous volume of data. To address these challenges, we develop a novel data processing procedure that is capable of converting ill-structured melt pool image streams to continuous thermal distribution models with the identical function support. Once melt pool images are defined in the same domain, the clustering algorithm of Self-Organizing Map is applied to group melt pool thermal distributions based on similarity, so that melt pools belonging to the same cluster share similar thermal distributions and tend to yield similar microstructure. On the other hand, melt pools from different clusters may exhibit different thermal behaviors. The dissimilarity between two clusters is characterized by their correlation. A cluster that has low correlation with the others or includes only a small number of melt pools is considered an anomaly, which is predicted to result in porosity at the corresponding location.
3. We validate the proposed porosity prediction method by benchmarking against the x-ray CT characterization of a Ti-6Al-4V thin-wall build fabricated using a LENS system. The results show over 96% of prediction accuracy and less than 0.02% false alarm rate. In other words, if the proposed prediction method is implemented during the build and the corresponding correction actions are taken before the subsequent layers are built, the porosity level of the as-built part can reduce to lower than 5% of the current level (without implementing our proposed *in-situ* monitoring). This is expected to significantly enhance the durability and reliability of AM parts to a higher order of magnitude.

4. The comparison with a previous work [74] that focuses on the morphological features of melt pools (e.g., area, length, width, etc.) shows significant improvement of prediction accuracy. SOM clustering based on morphological features only do not form distinct clusters. This means that process monitoring solely based on such simple features is not sufficient for anomalies identification. The thermal distribution within the melt pool should be taken into account.
5. Although the proposed *in-situ* monitoring methodology is validated based on experimental data generated from a LENS process, the developed framework can serve as a "real-time x-ray CT" for other AM processes sharing similar energy-material interactions (e.g., Powder Bed Fusion, Electron Beam Melting, etc.), as long as the material is deposited via the solidification of a melt pool. By capturing the melt pool anomalies, our method can potential capture the microstructure anomalies in real time.

Our work provides a theoretical foundation for the online certification and qualification of AM products. Future work is needed to enable and facilitate real-time processing of thermal images, which is extremely challenging considering large data volume and high data acquisition rate. Extra efforts are also needed to account for parts with complex geometries. Although the "thermo-physical dynamics" for the DED process is not comprehensively investigated, this study is the first step in achieving this. The focus of this study is relating thermal history of thin wall builds with microstructure. In the future studies, the goal is to investigate the effect of process parameters (e.g., powder feed rate, transverse speed, laser power, scanning pattern) and material properties on the thermal history, which in turn, affect the mechanical properties of the final product. Another possible extension of this work is to consider the re-melt phenomenon of AM fabrication.

2.7 Using self-organizing map for quantifying geometric accuracy in fused filament fabrication additive manufacturing parts

Additive Manufacturing (AM) enables the fabrication of complex geometry parts for a broad range of materials including metals, ceramics, and polymers [6, 8-10]. However, AM parts are afflicted by low geometric accuracy and poor surface integrity. The poor geometry of AM parts prevents their use in industries, such as aerospace, healthcare, automotive, etc., where precision is important [6]. The prevalent approach for quantifying the geometric accuracy of Additively Manufactured (AM) parts is to assess critical geometric dimensioning and tolerance (GD&T) characteristics, such as flatness, cylindricity, circularity, and more [11] based on several sample points (tens to hundreds) taken on certain part features. Although GD&T characteristics provide insights into feature-based geometric errors, the sampling strategy required for the extraction of GD&T characteristics needs to be carefully defined for parts with complex geometries. In AM, each combination of material, design and machine may create parts with specific types of geometric deviations in terms of direction and magnitude. We substantiate these assertions with experimental data from a fused filament fabrication (FFF) AM process in Sec. 3. Therefore, there is a need for developing methods that can efficiently characterize the geometric accuracy of AM parts with complex shapes.

2.7.1 Objective and significance

The goal of this work is to quantify the geometric deviations of additively manufactured parts from a large data set of laser-scanned coordinates. This is an important research area; recent developments in non-destructive scanning techniques, such as laser, structured light, and computer tomography engender point-by-point coordinate measurements of AM parts. These techniques can generate millions of coordinate points (three-dimensional (3D) point cloud). However, new analytical methods for quantifying the geometric accuracy of AM parts from these large scan

datasets are required. Accordingly, the objective of this work is to use an unsupervised machine learning (ML) algorithm called self-organizing map (SOM) to overcome this open research challenge. The SOM is used for demarcating or categorizing the point cloud measurements into limited number (tens) of clusters such that measurement points within the same cluster have similar shape deviations in terms of their severity (magnitude) and direction. Next, the clusters are ranked as per the severity (magnitude) of geometric deviations; contained in these few top-level clusters represent the most severe types of geometric defects associated with the part. The central hypothesis is that each SOM-derived cluster represents a unique type of geometric deviation specific to the process-material combination associated with the part, and thus the clusters are surrogate signatures of the part geometric accuracy. Experimental results with Fused Filament Fabrication (FFF) AM process indeed corroborate this hypothesis; it is shown that process conditions can be chosen to reduce the geometric errors by analyzing the number of clusters and the magnitude of deviations within a few important clusters (critical clusters).

The remainder of this chapter is organized as follows. Section 2.2 introduces the existing methods and their limitations. Section 2.3 describes the experimental measurement procedure and FFF process conditions that are used to print the parts along with the sample data, along with an introduction of the SOM approach. Section 2.4 applies the SOM algorithm to experimental 3D point cloud data and discusses the applications of SOM for geometric accuracy characterization and data reduction. Section 2.5 highlights the conclusions of this study and avenues for future research. The significance of this research is that the SOM-based unsupervised ML approach resulted in less than 3% of over 1 million data points being required to quantify the part geometric accuracy.

2.7.2 Existing state-of-the-art and research gaps

Typically, characterizing the geometric accuracy of a part relies on one of the following approaches: evaluation based on visual assessment [75], measurement based on specific landmarks on the part [76], and GD&T measurements using coordinate measuring machines (CMM) [77]. These approaches provide only limited information of the overall geometric accuracy of the part, and may not be capable of capturing the subtle difference parts of complex shapes fabricated using AM [8]. The existing literature pertaining to the characterization and optimization of geometric accuracy in AM can be divided into three groups: (1) data science (empirical modeling), (2) physics-based modeling (mostly finite element analysis), and (3) shape compensation.

2.7.3 Data science approaches (Empirical modeling of geometric accuracy in AM)

Measuring part geometric accuracy is typically performed with various approaches, including ultrasonic, x-ray tomography, and laser scanning [77-81]. The resulting data are typically analyzed using statistical models (e.g., response surface regression and analysis of variance [82-85]) to develop an empirical mapping of the relationship between input process parameters and geometric accuracy. For example, Wang et al. [86] used least squares regression to correlate shrinkage of fabricated parts and process parameters (e.g., laser power, layer pitch, scanning speed) in the stereolithography (SLA) process. Zhou et al. [82] used a 3-D coordinate measuring machine and surface profilometer to capture geometric accuracy, and surface roughness of parts in SLA process. Through Taguchi experimental designs, Zhou et al. [82] found that by adjusting process parameters, such as layer thickness, hatch spacing, overcure, blade gap, and position on build plane, the part errors can be controlled to be less than 0.0013 mm/mm. Furthermore, Noriega et al. [87] used an Artificial Neural Network (ANN) model coupled with an optimization algorithm to improve GD&T characteristics such as distance between parallel faces in FFF fabricated parts.

However, these previous works only use limited number of samples with simple geometries to model GD&T characteristics such as cylindricity and flatness; thus, these works cannot capture the critical features for the parts with complex shape [88, 89].

These previous works use limited number of samples with simple geometries to model GD&T characteristics such as cylindricity and flatness; and thus cannot capture the critical features for the parts with complex shape [90]. The work presented herein goes one step further by examining multiple features, but is nonetheless also based on a test artifact composed of elementary geometries. The authors will extend this research to more complex AM geometries, such as thin walls and steep overhangs in their forthcoming works.

2.7.4 Physics-based modeling approaches (Finite element modeling of geometric accuracy in AM)

Thermomechanical modeling has been proposed to account for thermal-related deformation and the geometric accuracy of AM parts. These methods consider the effect of process parameters, such as slice thickness, part orientation, scanning speed, and material properties [90]. The advantage is that finite element models can be used to simulate a build without actual fabrication, and to investigate the relationship between process parameters and geometric accuracy [91, 92] (given that the models are validated over the applicable process parameter range). Pal et al. [91] proposed a 3D dislocation density-based model to capture the relationship between thermal contours and residual stresses. They controlled the layer-by-layer geometrical errors in the prebuild stage by adjusting AM process parameters, including scan pattern and build orientation. This method accurately predicts the mechanical properties (e.g., residual stress) as a function of process parameters, leading to less post-printing rework.

Paul et al. predicted part shrinkage in powder based AM processes by modeling the powder-to-liquid- and liquid-to-solid-state changes [92]. FE modeling is used to track the

temperature gradient history in various layers and compute the overall shrinkage in the part. Subsequently, the authors use virtual geometric models to characterize thermal deformation in terms of GT&D characteristics. Jiang et al. proposed a simulation model to examine the inaccuracy of the Mask Exposure Scanning Stereolithography (MESS) process[93]. Based on the simulation results, the authors suggested an optimal scan path and exposure time. Analysis of the scanning pattern indicated that the sharp corners on the part shrink faster than rounded edges. While useful at the design phase, FE-designed process plans tend to deviate from the actual build geometry due to the inability to accommodate the uncertainty stemming from materials or process parameters. The errors in the printing process accumulate over several layers and can eventually result in significant deviations.

2.7.5 Shape compensation

Researchers have suggested approaches to enhance geometric accuracy of AM parts via shape compensation [84, 85, 92]. In particular, deformation may occur during the solidification of each layer and accumulate over layers, eventually resulting in distortion [86, 94]. A procedure developed by Huang compensates for the two-dimensional (2-D) shape deformation in SLA [94]. The proposed method provides a minimum area deviation (MAD) norm to rectify the 2-D shape deformation. However, the model considers shrinkage in layers to occur independently and does not capture the interaction between layers; therefore, this method is limited to simple shapes.

2.7.6 Research gap

Very few of the existing studies are dedicated to the analysis of point cloud data for the characterization of AM geometric integrity. A recent study by Rao et al. [81] applies spectral graph theory (SGT) to point cloud data generated parts based on different process parameters to rank/classify the geometric accuracy of parts. The proposed approach ranks the overall quality of

AM parts based on the spectral graph Fiedler number, a criterion commonly used in graph theory to assess connectivity. However, the type of geometric deviation (i.e., direction and magnitude) associated with a specific design of parts cannot be obtained from this approach. The method proposed in the current study addresses this issue from a fundamental level. Instead of using only one absolute value to evaluate the geometric accuracy of part, the approach outlined herein identifies candidate features based on the shapes of designs, enabling automated certification of geometric accuracy in the future.

2.8 Methodology

It is noted that the test parts used for this work are made on a consumer-grade FFF printer (Makerbot2X) and relatively inexpensive laser scanner (NextEngine). The authors acknowledge that although the choice of a desktop machine constrains the experimental scope of this paper; however, the mathematical concepts are independent of the hardware and manufacturing process. The native software on the FFF machine was used for slicing and toolpath planning under default conditions.

2.8.1 Characteristics of point cloud data

Test part: The test artifact used for experimental studies is a simplification of the NAS 979 standard artifact. The NAS 979 artifact is traditionally used to test the accuracy of machining centers [95-97]. Recently, Cooke and Soons at NIST used the NAS 979 part to assess AM process performance [96, 97]. GD&T characteristics, such as squareness, size (length, breadth, and thickness), and circularity were used to compare the quality of parts produced using electron beam melting and direct metal laser sintering metal AM processes. For the experimental tests reported in the current work, the NAS 979 standard test artifact was simplified so that it was easier to make

in terms of build time and feature complexity; this simplified design is called as circle-square-diamond. A schematic of the test part used in this study is shown in Figure 2.15(a).

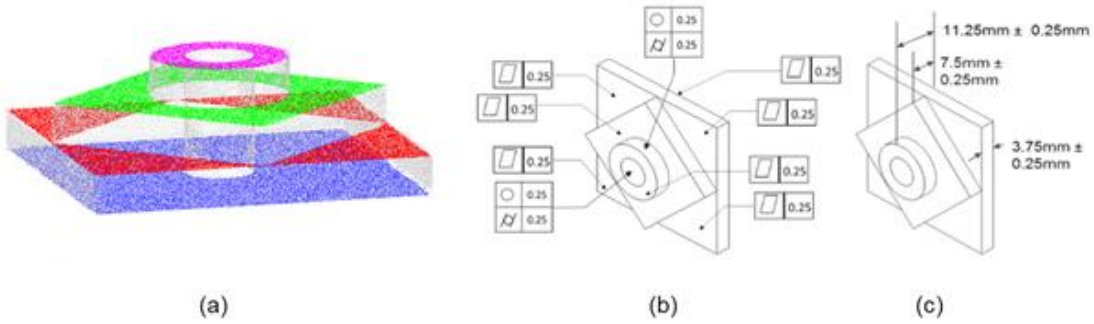

Figure 2.15 The design part used to measure GD&T. Sub-figure (a) shows the 3D view of the fabricated test part using FFF process. Sub-figure (b) shows the faces used to measure flatness (⏥), circularity (⌾), and cylindricity (⌭); and (c) shows the planes used to measure the thickness – three thickness measurements are taken on each plane. Different colors represent the various plane and the point cloud data.

Data acquisition: A desktop 3-D laser scanner (NextEngine) is used to scan the surface of FFF test parts and obtain point-by-point coordinate measurements of the geometry, referred to as a 3-D point cloud. The laser scanner records reflected light from the part surface as a point in the 3-D space, with a maximum volumetric deviation. The scanner uses eight 10-mW Class 1 red lasers at 650 nm in two arrays of four diodes. These arrays rotate together and project lines onto the object and two 3.0 megapixel cameras capture the reflection of the lasers over the part. This desktop scanner was used in Macro mode, which is capable of scanning objects up to 130 mm × 10 mm in a single scan at ± 0.127 mm accuracy. The scans and measurements generate a large volume of data (e.g., 110 Mb for a small part with volume 7911 mm^3).

Geometric deviations of the fabricated parts can be calculated by comparing the point cloud data to the original CAD model. A sample of data is shown in Table 2.5. (X, Y, Z) represents the coordinates of measurement point, and (Δ_x,Δ_y, Δ_z) represents the corresponding measurement of

geometric deviation in the (X, Y, Z) directions, respectively. For the test part shown in Figure 2.15, the scanning results in over 1 GB of point cloud data in the ASCII text format, consisting of 18,098,301 rows with each row representing a measurement of geometric deviation.

We note that laser scanning consists of several steps, such as point cloud extraction from the CAD design, alignment of the measured scan to CAD, and the subsequent analysis, each of which has its own literature [98-104]. In practice, laser scanning requires a careful part alignment procedure to obtain consistent results. The alignment step requires matching of (at least 4) points from the raw point cloud data with CAD model. The following method, which has been described in our previous works, showed the least variability. Four points each on the square and diamond portions are used to align the part as depicted in Figure 2.16. Scanning was conducted on a sturdy table in a dark room and by coating the part with a thin layer of anti-reflective gray modeling paint.

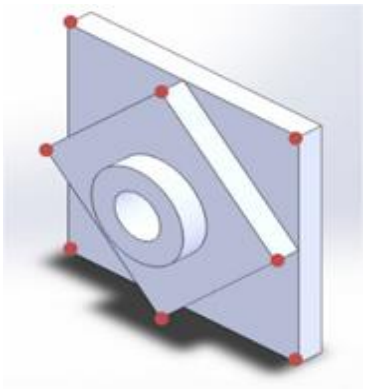

Figure 2.16 The eight points used for alignment of the scan points with the CAD model [105-108].

Experimentation: The experimental conditions are shown in Table 2.5 along with the typical number of point cloud data points obtained at each condition. Two process parameters are varied in these experiments, namely, the infill percentage (I_f) and the extruder temperature (t_e) The experimental procedure is described in depth in by Dsouza et al. [108] and in a recent

publication by the authors [107]. The dataset has 12 distinct discrete experimental treatment conditions with different characteristics. In this design of experiments plan, no experimental data was obtained under certain treatment conditions because of repeated failure to print. Two parts were printed (left and right side of the print bed) at each experimental run.

Table 2.5 Example of point cloud datasets acquired from the 3-D laser scanner (mm).

Measurement Point	X	Y	Z	Δ_x	Δ_y	Δ_z
1	23.73	28.31	1.68	0.07	-0.18	0.00
2	23.73	28.35	1.59	0.06	-0.14	0.00
⋮	⋮	⋮	⋮	⋮	⋮	⋮
2,999,999	33.01	16.91	8.82	0.00	0.00	0.16
3,000,000	33.11	16.82	8.82	0.00	0.00	0.16
⋮	⋮	⋮	⋮	⋮	⋮	⋮
9, 999, 999	43.65	37.11	1.73	0.00	0.00	0.57
10, 000, 000	43.99	37.24	1.58	0.24	0.00	0.41

Table 2.6 Different process conditions obtained by changing Infill (%) (I_f) and extruder temperature (°C) (t_e) in FFF where values in each cell accounts for the number of geometric deviations (point cloud data).

	Infill (I_f, %)			
Temperature (t_e,°C)	70 %	80 %	90 %	100 %
220 °C	No experiment		1,233,867	No experiment
225 °C	No experiment	1,712,653	1,107,267	685,961
230 °C	1,233,867	1,250,357	1,619,690	1,796,948
235 °C	No experiment	1,795,849	1,758,031	1,692,290
240 °C	No experiment	No experiment	2,211,521	No experiment

Rationale for selecting the infill percentage (I_f) levels: Four levels of infill percentage (I_f), namely, 70%, 80%, 90%, and 100% are investigated. Infill percentage (I_f) determines the amount of material in the inside of the part; 70% infill percentage implies the part has 30% void volume. Lower infill percentage reduces the weight of the part, while affecting the strength. At higher infill

values it is observed (in the authors' preliminary experiments (see Figure 2.17), that the geometric integrity deteriorates, while strength improves. The reason for selecting an infill percentage range of 70% to 100% is based on longitudinal fracture test results (Figure 2.17) with FFF-printed ASTM 638D-Type V specimens. The samples were built face down on the platen, the load was applied parallel to the long edge of the sample (i.e., perpendicular to the build direction). The samples built at I_f = 100% showed significantly higher fracture strength compared to other levels. Pertinently, the specimen fracture strength was statistically indistinguishable with infill percentages at and below 90% ($I_f \leq 90$). Hence, a balance between strength and geometric integrity must be sought. Accordingly, the lowest infill percentage level was set at 70% considering the inevitable tradeoff between strength and geometric integrity.

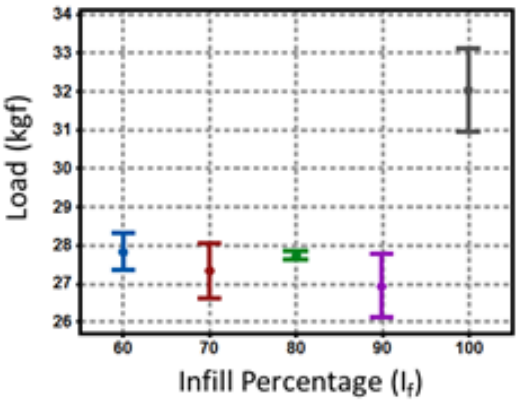

Figure 2.17 Fracture strength of ASTM 638D-Type V samples under different infill percentages. The error bars are ± 1 standard deviation (eight samples at each infill percentage level).

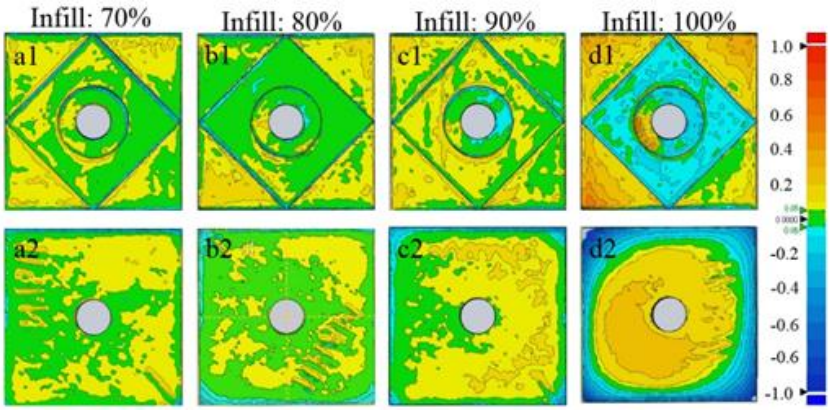

Figure 2.18 Flooded contour plots of the benchmark part used in FFF experiments detailed in Sec. 2.1. The material is ABS polymer. The first row (1) shows the top-views and the second row (2) contains the bottom-views of the parts. Figures a-d represent different parts, printed under 70%, 80%, 90%, and 100% infill percentages at 230 °C, respectively. The color scale is in mm [1–4].

For instance, Figure 2.18 shows the flooded contour plot for four different test parts fabricated under different infill percentages, at 230 °C extruder temperature. It is visually evident that different infill percentage (I_f) results in different part geometric accuracy; the first three parts ($I_f = 70, 80 \text{ and } 90\%$) are better than $I_f = 100\%$. The effect of infill percentage (I_f) on the internal morphology of the part can be hypothesized by examining the micrographs shown Figure 2.19. Previous studies provide ample evidence to the presence of thermal residual stresses in FFF parts. For instance, Chang and Zhou [109] modeled the residual stresses resulting from cyclical heating and cooling in FFF and subsequently used their validated model to assess effects of feed rate (or velocity of extruder movement), road width, and layer thickness. At lower infill percentages (70%, 80%) the thermal residual stress has an avenue to be relieved given the gap between adjacent roads; the gap allows for shrinkage without warping. In contrast, at 100% infill, the lack of gap between roads prevents stress relief, leading to warpage and deleteriously affecting the geometric integrity.

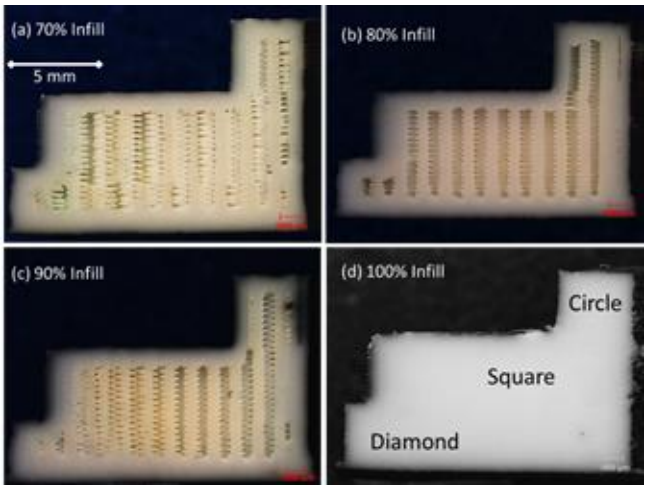

Figure 2.19 Micrograph showing the effect of infill percentage on the internal morphology of the circle square diamond part at 230 °C extruder temperature. Shown is the quarter cross-section of the part, the circular section is at the top end. At 100% infill the thermal residual stresses cannot be accommodated without deleteriously affecting the geometric integrity, since there is no vacant space for stress relief.

Rationale for selecting the extruder temperature (t_e) levels: In case of extruder temperature (t_e), the recommended printing temperature for ABS material is 230°C. Exploratory tests showed that at lower temperatures (< 215°C) the nozzle fails to extrude the material consistently, and at higher temperature (> 245°C), the filament vaporizes. Accordingly, five levels of extruder temperature (220°C, 225°C, 230°C, 235°C, and 240°C) are chosen to study the effect of temperature on geometric integrity.

GD&T data analysis: Geometric dimensioning and tolerancing (GD&T) characteristics can be ascertained based on the sampling of point cloud data, including flatness, thickness, circularity, cylindricity, concentricity, and others as shown in Figures 2.15(b-c). In Figure 2.20, two GD&T characteristics (thickness and flatness) are mapped against the two FFF process conditions (infill percentage [I_f] and extruder temperature [t_e]) with three replications. In a recent work by the authors [106, 108], it was shown that some GD&T characteristics defined based on simply shapes may not capture major geometric defects of specific part shapes, and may even be

negatively correlated ($\rho < 0$). A negative correlation between flatness and thickness is evident in Figure 2.20; the process conditions resulting in lower deviation in thickness may lead to high deviations in flatness ($\rho \sim -0.2$). The size of the circle represents the ratio between the deviation in thickness and deviation in flatness. For example, at 90% infill, there is no clear trend about the effects of temperature on the ratio between thickness and flatness. Hence, it is difficult to use the GD&T data to ascertain what the optimal set of processing conditions are, given that some of the GD&T measures contradict one another.

2.8.2 Profiling geometric deviations based on SOM analysis

Traditional GD&T characteristics may not be sufficient to capture the geometric accuracy of AM parts. Herein we use unsupervised ML based on neural networks to recognize and identify new geometric deviations. The chosen unsupervised ML approach is the concept of SOM, which clusters the various geometric deviations into multiple classification types according to their directions and magnitudes. Parts within each SOM-identified cluster are similar in magnitude and direction of geometric deviations. Thus, each cluster represents a unique type of geometric deviation. This is useful to identify the different types of geometric deviations associated with specific process conditions. By focusing on the critical types of geometric deviations, the proposed method is robust to noise in the data. Thus, the volume of the overall dataset can be significantly compressed. This will speed adaptation of the 3-D laser scanning in industrial application and enhance the scanning speed of parts and reducing the data size.

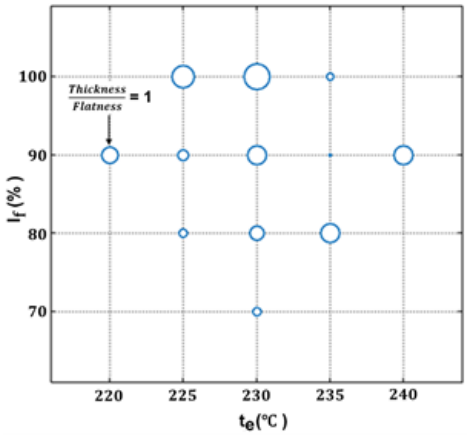

Figure 2.20 Comparing the flatness and thickness of GD&T characteristics using various set of process conditions (Infill (I_f), Extruder temperature (t_e)). The circle size represents the ratio between thickness and flatness.

As an introduction to SOM, it is a type of an unsupervised ML neutral network that uses a procedure called competitive learning to discern patterns [65, 67]. The SOM maps high-dimensional input data into a 2-D space, while preserving the topological interrelationship between data; the mapping does not change the relative distance or similarity among data points [68]. The clustered data reduces the dimensionality and intuitively characterizes the similarity among data points. The 2-D map resulting from SOM is called a space membership map.

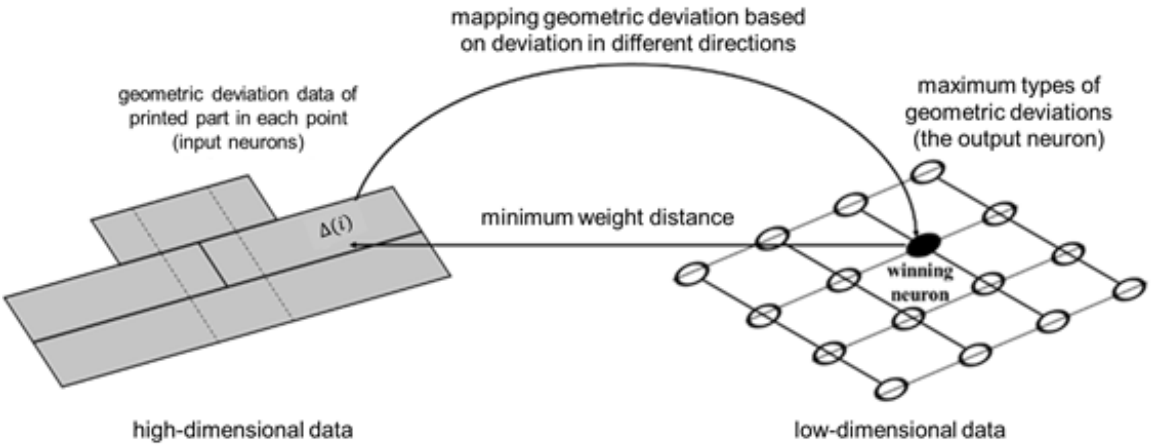

Figure 2.21 Clustering point cloud data according to the direction and magnitude of geometric deviations using SOMs to a 4 × 4 quadrilateral space membership map.

Figure 2.21 is a schematic SOM network for a dataset with 3 attributes. This structure of the network could address a clustering challenge on a dataset with three attributes and 16 possible clusters. As shown in Figure 2.21, each structure of the SOM network contains three types of entities: input neurons, connecting vectors, and output neurons. The vectors connect the input neurons to the output neurons and neighboring output neurons to each other. Each vector has a weight that is produced randomly in the initialization procedure and updated in the training process. Based on the nature of connections in the output layer, two types of SOM maps exist: quadrilateral or hexagonal. The network in Figure 2.21 yields a quadrilateral map with at most four connections for each neuron with its neighbors.

Deviations in the part (Figure 2.15) are denoted by the vector $\Delta(i)=(\Delta_x^{(i)},\Delta_y^{(i)},\Delta_z^{(i)})$ where *i* represents each data point in point cloud data of the fabricated part, and $\Delta_x^{(i)}$, $\Delta_y^{(i)}$,and $\Delta_z^{(i)}$ are deviations in x,y, and *z* direction for a measurement point i. We apply a SOM with 5 × 5 hexagonal structure to the point cloud data, which yields 25 clusters (cells). These 25 hexagonal cells represent different types of geometric deviations and captures the discrepancy in various types of

geometric deviations in terms of the magnitude and directions. The number n_k in each cell is the number of deviation data points associated with cell k (e.g., n_1 is the number of point measurements in cluster 1). Some cells can be empty and others may be combined into one if they are highly correlated; this is done in an unsupervised fashion by the SOM algorithm. In the end, low correlation between points in adjacent cells results from a difference in the magnitude and/or direction of deviation. An example of the SOM output can be found in Figure 2.22.

The size of the SOM model, characterized by the number of cells, governs the accuracy and efficiency of the clustering algorithm. A higher-order model with larger number of cells is capable of capturing the subtle differences amongst various types of geometric deviations. However, it also results in longer computation time, and tends to over-fit the data, making the results sensitive to noise. By contrast, a lower-order model is faster and captures the major types of geometric deviations. However, subtle changes in geometric deviations may not be captured with a lower order model. The selection of SOM models depends on availability of computational resources and the application. In this work, we choose a 5×5 hexagonal SOM, resulting in a maximum number of 25 (=5×5) clusters. This resolution is reasonable for identifying the major types of geometric deviations and does not cause a significant computational burden. For instance, increasing the number of clusters to 36 (=6×6) increases the computation time to 1200 seconds compared to 800 seconds for 25 clusters, this further increases to 1800 seconds when 49 (=7×7) clusters are implemented. Using a 7×7 SOM also leads to spurious segmentation of the data.

The training of the SOM model is influenced by the structure of the point cloud data. Selecting the data samples to initiate the SOM network is difficult, because the current dataset is too large to process data points for each treatment condition at once and the dataset has 12 distinct experimental point clouds (i.e., 12 processing conditions/parts) with different characteristics.

Existing approaches for SOM training recommend exposing the network to each of the data from the start to the end. This approach suffers from the following drawback: the first incoming rows of data (data-rows) have an advantage, because the SOM is vulnerable to initial exposures. Another approach is to randomly pick the data for each and every data-row being presented to the network. This approach suffers from the disadvantage of uncertainty resulting from not exposing the data-rows in an equitable manner. To overcome these challenges, the network is exposed to 200 batches of 5000 data-rows drawn randomly from one of the process condition (also selected randomly) in Table 2.5.

2.9 Results: Clustering am point cloud data using self-organizing maps

2.9.1 Characterizing deviations types

Each cell in Figure 2.22 represents a type of geometric deviation, and the numbers in each cell are the number of data points belonging to that cell. The results of the SOM clustering for two combinations of process parameters is shown in Figure 2.22. We apply a 5 × 5 SOM to the point cloud data to profile the types of geometric deviations for each fabricated part. Figure 2.22 illustrates that the fabricated part with process condition (t_e= 225 °C, I_f=100%) has more clusters than process condition (t_e= 230 °C, I_f = 80%), this means that processing condition (t_e= 225 °C, I_f=100%) results in more types of deviations in terms of direction and magnitude. The significance of this result is two-fold: (1) SOM can provide an informatics indicator about the overall geometric accuracy of the part fabricated using each combination of process parameters; and (2) The deviations of a part associated with specific combination of process parameters can be characterized by the critical types of deviations, which can significantly reduce the amount of data needed.

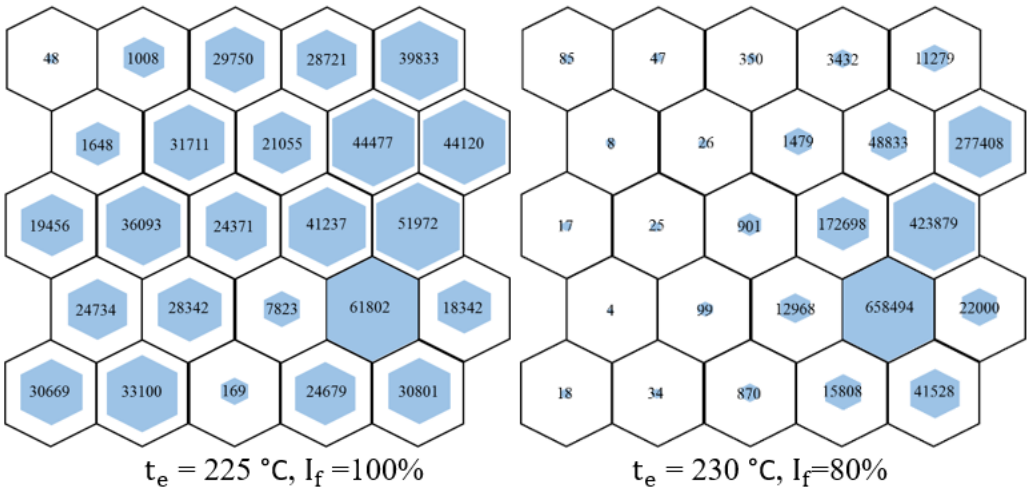

Figure 2.22 SOM-based deviation clustering method applied to different FFF process conditions. (left) t_e = 225 °C, I_f =100%; (right) t_e = 230 °C, I_f =80%.

SOM results provide an intuitive representation of the types of deviations for each combination of process parameters. Figure 2.23 (a) depicts the different types of geometric deviations, based on SOM clustering, from parts fabricated using two sets of process conditions: circle denoting the process condition (t_e = 225 °C, I_f = 100%), and square for the process condition (t_e= 230 °C, I_f= 100%). The horizontal and vertical axes represent the deviation in x and y build directions, respectively. The size of the markers represents the magnitude of deviation in the *z* direction; the larger the marker the worse the part consistency. Figure 2.23 (a) shows that the process condition (t_e= 225 °C, I_f = 100%) leads to shrinkage in the x direction and expansion in the y direction because multiple clusters have been observed in the second quadrant (i.e., negative and positive), whereas process condition (t_e= 230 °C, I_f = 100%) results in the part being larger in the *x* direction (closer to nominal).

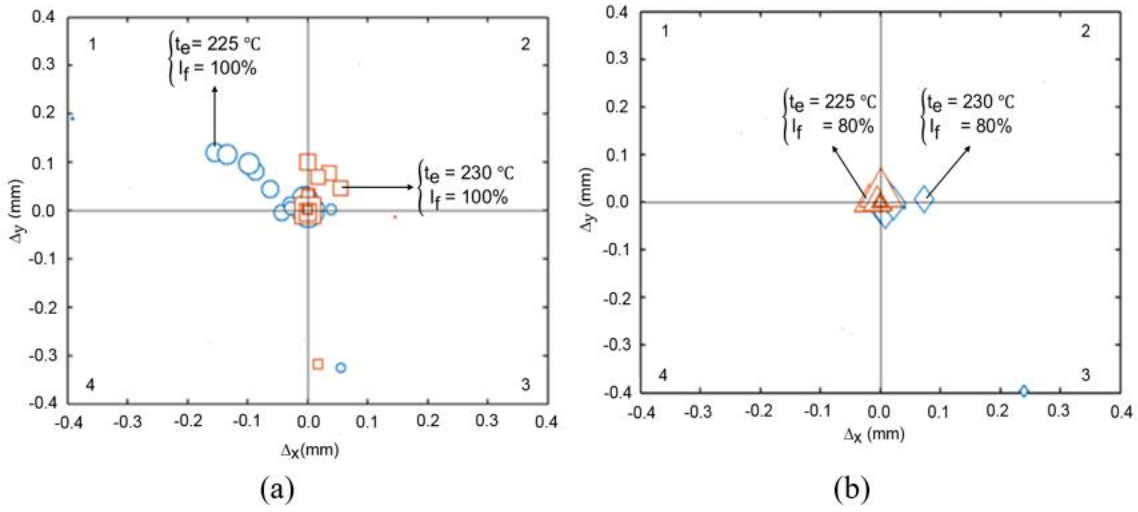

Figure 2.23 (a) Comparing magnitudes of various type of deviations for two distinct parts in the direction in their corresponding x-direction and y-direction where circles and squares illustrate the magnitude of deviation in z-direction (t_e= 225 °C, I_f =100%) and (t_e= 230 °C, I_f = 100%) respectively. (b) Comparing magnitude of various type of deviations for two distinct part in z-direction in their corresponding x-direction and y-direction where triangles and diamonds illustrate the magnitude of deviation in the z-direction for (t_e= 225 °C, I_f = 80%) and (t_e= 230 °C, I_f = 80%) respectively.

The outcome of such an analysis is that once the types of geometric deviations for specific processing conditions are profiled, actions such as CAD compensation, machining, etc., can be taken to improve the geometric accuracy. For instance, to improve the geometric accuracy of parts fabricated using the process condition associated with t_e = 225 °C and I_f = 100%, the users can provide an allowance in the CAD model in the x direction and scale down in the y direction to compensate for the shrinkage and expansion in the respective directions; for t_e= 230 °C and I_f = 100%, the CAD file can shrink in the y direction. We also note that both process conditions result in an outlier cluster in the fourth quadrant caused by minor expansion in the x direction and significant shrinkage in the y direction. Similarly, Figure 2.23 (b) demonstrates the profiles of geometric accuracy for parts printed using process condition associated with (t_e = 225°C, I_f = 80%) (circle), and (t_e = 230 °C, I_f= 80 %) (diamond). The quality of the part printed using the

process conditions depicted in Figure 2.23 (b) is better compared to the process conditions in Figure 2.23 (a), because in general the geometric deviations are more consistent in all directions. While the SOM-based analysis in Figure 2.22 was able to clearly identify the types of geometric deviations, the visual characteristics could not distinguish subtle differences in the geometric deviations of those parts. This corroborates our hypothesis that SOM-based analysis of data links geometric accuracy to specific process conditions that is not possible with traditional approaches. Furthermore, the SOM clustering approach identifies the types of geometric deviations specific to the part designs.

2.9.2 Characterizing overall geometric accuracy

We next characterize the overall geometric integrity of a part by taking into account the number of data points in each cluster. For any cluster C_j, we define the weighted cluster deviation as $\overline{\Delta}_j = \frac{n_j}{N} \|\Delta_j\|$, for j=1,…,m, where Δ_j represents the center of cluster C_j. Hence, $\overline{\Delta}_j$ captures the deviation magnitude of cluster C_j weighted by the number data points in the cluster. If a relatively high $\overline{\Delta}_j$ value for a certain cluster is observed, the implications are twofold: (1) the magnitude of the corresponding type of geometric deviation is significantly high, and (2) the number of points with this type of geometric deviation is relatively large, compared to geometric deviations in other directions. The average magnitude of deviation for the whole part is calculated as $\xi = \frac{1}{m} \sum_{j=1}^{m} \frac{n_j}{N} \|\Delta_j\|$, which can be used as an indicator of the part geometric accuracy.

We plot the $\overline{\Delta}_j$'s values for various combinations of process parameters (t_e=225°C, 230°C, and I_f = 80%, 90%, 100%) as shown in Figure 2.24. The values of $\overline{\Delta}_j$'s are represented by different colors. The lighter colors denote lower values of $\overline{\Delta}_j$ with a minimum value of 0, whereas the darker colors represent higher values. For example, process condition (t_e = 225 °C , I_f = 100%)

yields a larger number of clusters with significant values of $\overline{\Delta}_j$ (yellow blocks). This means that parts fabricated using this combination of process parameters results in multiple types of major deviations, each of which includes a large amount of data points. However, process condition with a lower infill percentage (I_f = 90%) results in much fewer number of clusters with significant $\overline{\Delta}_j$ values. Therefore, the overall geometric accuracy of parts printed using process condition (I_f = 90%) is comparatively higher than (I_f = 100%). The average magnitude of geometric deviation, ξ is also presented. The value of ξ is much higher for process condition (I_f = 100%), compared to process condition (I_f = 90%).

Comparing $\overline{\Delta}_j$ maps (as shown in Figure 2.24) across various combinations of process parameters allows to establish a relationship between processing conditions and the geometric accuracy of the part. The process condition (t_e = 230 ℃ , I_f = 80%) yields the minimum number of clusters signifying different type of deviations. Besides, the process conditions (t_e = 225℃ , I_f = 80%) and (t_e = 225℃ , I_f = 90%) are close to the best process condition. The geometric accuracy of as-built parts for each processing condition can also be ordered according to the ξ values. The processing condition (t_e = 230℃ , I_f = 80%) results in the lowest ξ value among the six combinations of process parameters and thus results in the highest geometric accuracy. This finding is remarkably consistent with Tootooni et al. where the authors assessed the geometric integrity of parts based on Spectral Graph theory (SGT) [107]. The SGT method provides an overall description of the geometric accuracy using graph theoretic quantifiers. The presented approach additionally characterizes the profiles of the different parts in terms of types and magnitude of deviation as shown in Figure 2.24. This information is not captured in the recent work by Tootooni et al. [107].

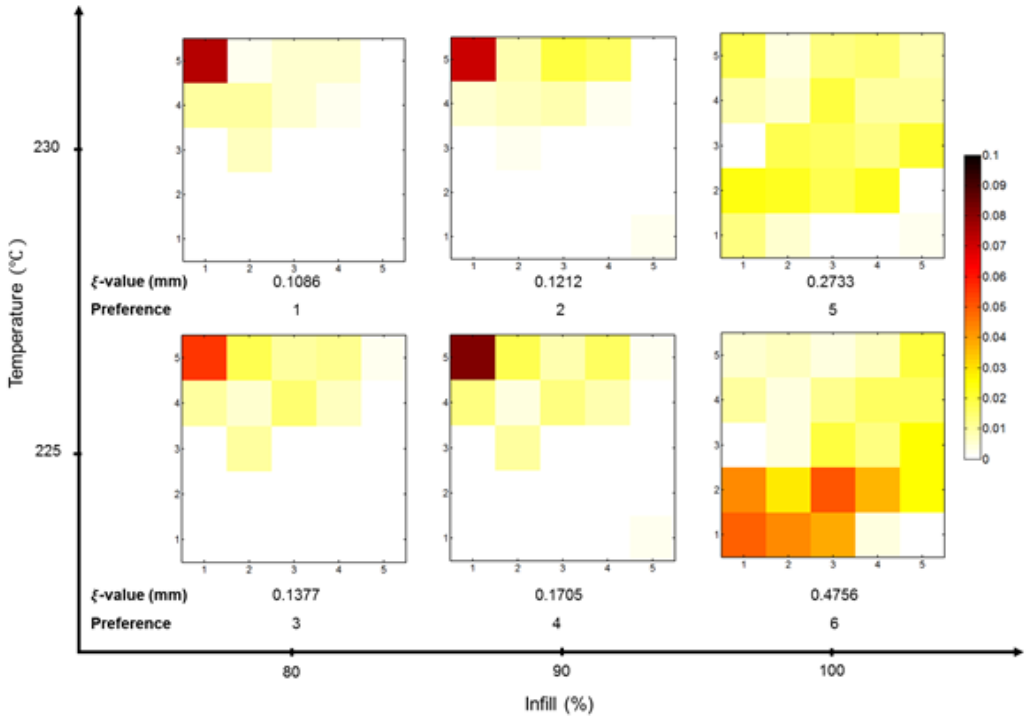

Figure 2.24 Comparing the geometric quality of printed parts using FFF where two-levels of (t_e= 225 °C and 230 °C) and three-levels of (I_f = 80, 90, and 100%) are selected.

2.9.3 Data reduction based on critical clusters

We reduce the amount of point cloud data needed to characterize the part geometric accuracy based on the top-k critical clusters, i.e., the clusters with highest magnitude of deviations. We denote by τ the threshold of deviation magnitude for the top-k clusters, which selects clusters whose deviation magnitude is higher than τ, i.e., $\|\Delta_j\| \geq \tau$ for $j=1,\ldots,m$. Figure 3.10 shows the deviation magnitude of all SOM clusters ordered from the highest to the lowest. The horizontal axis shows the label of SOM clusters. The vertical axis shows the magnitude of deviation (mm). When τ = 0 mm, all the clusters are selected. On the other hand, when τ=4mm, no clusters are selected. The choice of τ depends on the need of data compression and the requirements of geometry tolerance. We choose τ=1.5mm (green line) as a threshold for data reduction, which selects the top-4 clusters, namely clusters 21, 16, 22, and 11.

We find that (1) the selected clusters consist of only 2.4% of the total data points; and (2) the ranking of geometry accuracy based on the top-4 clusters is completely consistent with the ranking based on the full data set as shown in Figure 2.25. Due to the limited length of the manuscript, we do not present the ranking of parts based on the top-4 clusters here. This result (Figure 2.25) means that we only need 2.4% of the data points to accurately characterize the geometric accuracy of a part. This will tremendously accelerate the process of part scanning by focusing on the areas associated with the top-4 clusters.

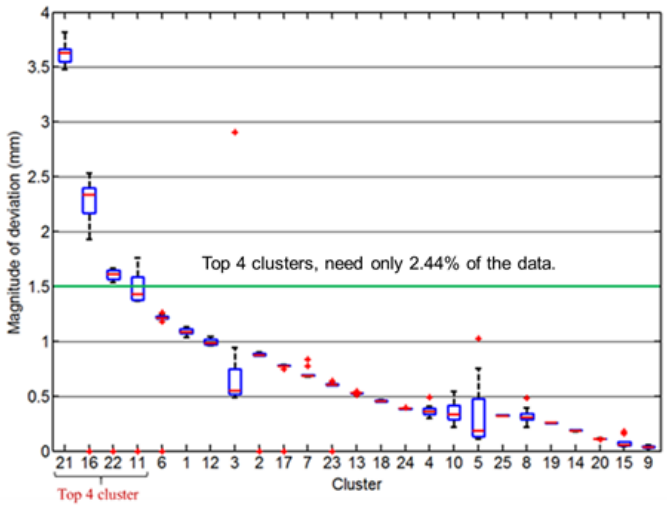

Figure 2.25 Selecting the top k clusters based on estimated minimum magnitude of deviation.

We find that the selected top-4 clusters correspond to critical locations of the part, such as corners, edges, interface between two structures, and others. The areas identified by top-4 clusters are shown in Figure 2.26. Figure 2.26 (a) illustrates the deviation points in an exponentially shaped curve for cluster 22, heights of which ranges from -0.45 mm to 1.5999 mm, which is illustrated in front view by the red line. Figure 2.26 (b) demonstrates the deviation points in circular shaped curve for clusters 16 and 21 with heights varying from 7.3959 mm to 7.5834 mm. For cluster 11,

deviation points are recommended to scan in the pattern as shown in Figure 2.26 (c). In this case, height value ranges from 3.6544 mm to 4.9834 mm. This analysis significantly reduces scanning time and cost in AM process. Only 2.4% of the areas of the part need to be scanned for capturing the difference between parts produced under different conditions. Surface scanning focusing on such critical locations identified by top-4 clusters will significantly improve the speed of quality inspection, while capturing the main geometric deviations associated with the fabricated parts.

2.9.4 Verification with K-means unsupervised clustering

We applied the K-Means unsupervised clustering method to validate the efficiency SOM clustering technique. The training procedure for the K-means model is similar to the SOM; the model is exposed to 200 batches of 5000 data-rows drawn randomly from one of the (randomly) selected process condition. Subsequently, the trained model of K-means is applied to each process condition to generate the clustering map, which contains different type of geometric deviations. The clustering map for two combinations of process parameters is illustrated in Figure 2.27, similar to the obtained results from SOM, parts printed using process condition (t_e=230 °C , I_f = 90%) yield the minimum overall geometric deviation. Moreover, the preference ranking of parts contingent on the geometric integrity remains unchanged. However, the geometric deviations assessed by K-means is larger than those estimated from SOM clustering. This is because K-means clustering is more sensitive to noise in the data compared to SOM; in that K-means clustering assigns the noisy observations (outliers) to the main clusters, which causes an increase in the magnitude of deviation ($\overline{\Delta}_j$), which in turn is directly related to overall geometric deviation (ξ) [110]. Furthermore, the amount of point cloud data needed to characterize the part geometric accuracy based on the top-k critical clusters is slightly larger with K-means clustering. The top 9 clusters require ~3% of the total data points compared to ~2.4% for SOM.

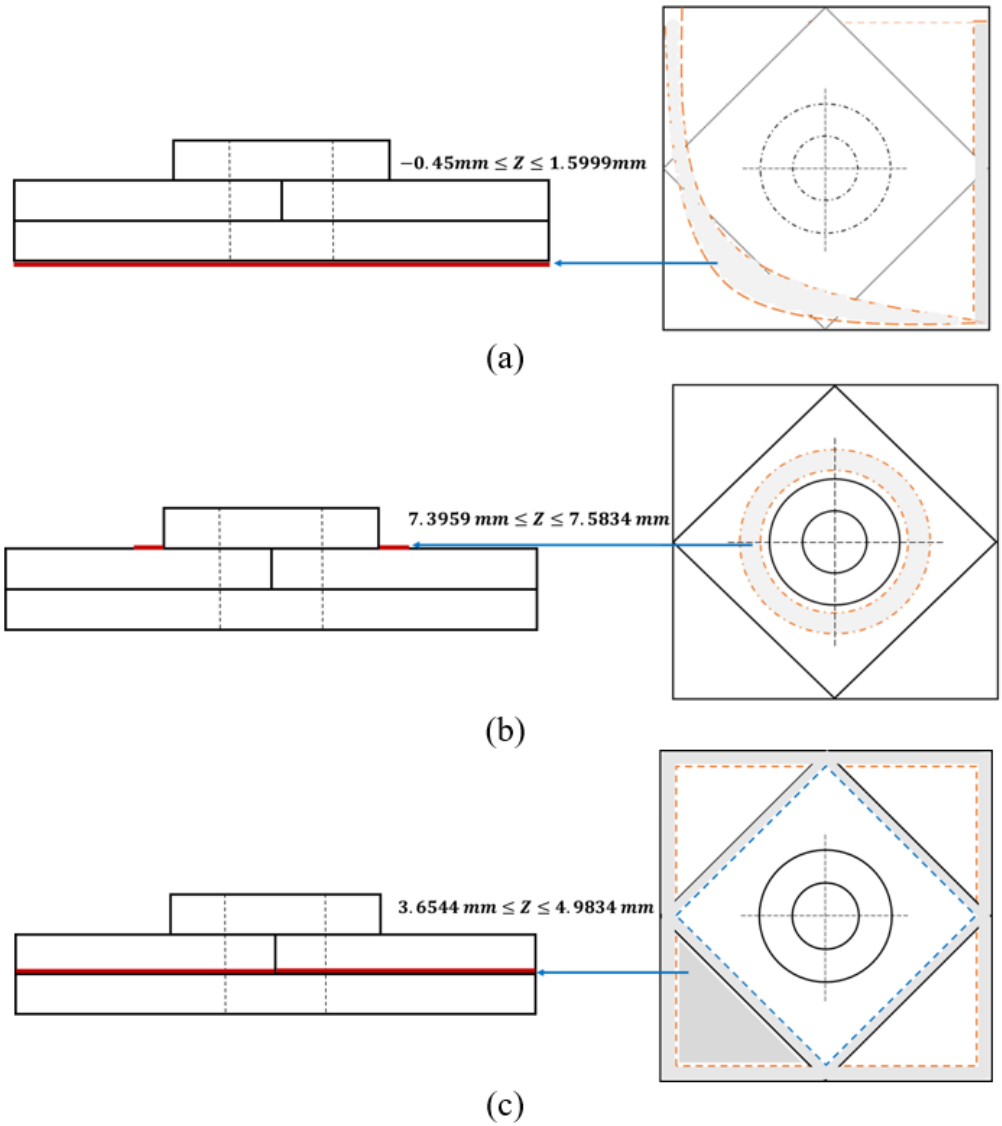

Figure 2.26 Identifying the new scanning areas based on location of point cloud data in top 4 clusters where (a) illustrates thin-exponentially shaped scanning pattern for designed part using point cloud data based on deviations from cluster 22, (b) demonstrates thin-circular shaped scanning pattern for designed part using point cloud data form on deviations in cluster 16 and 21, and (c) shows thin-cubic shaped scanning pattern for designed part using point cloud data depend on deviations of cluster 11. (The scanning pattern demonstrated from top and view in right for (a) and (b) and bottom and right view for (c) respectively.

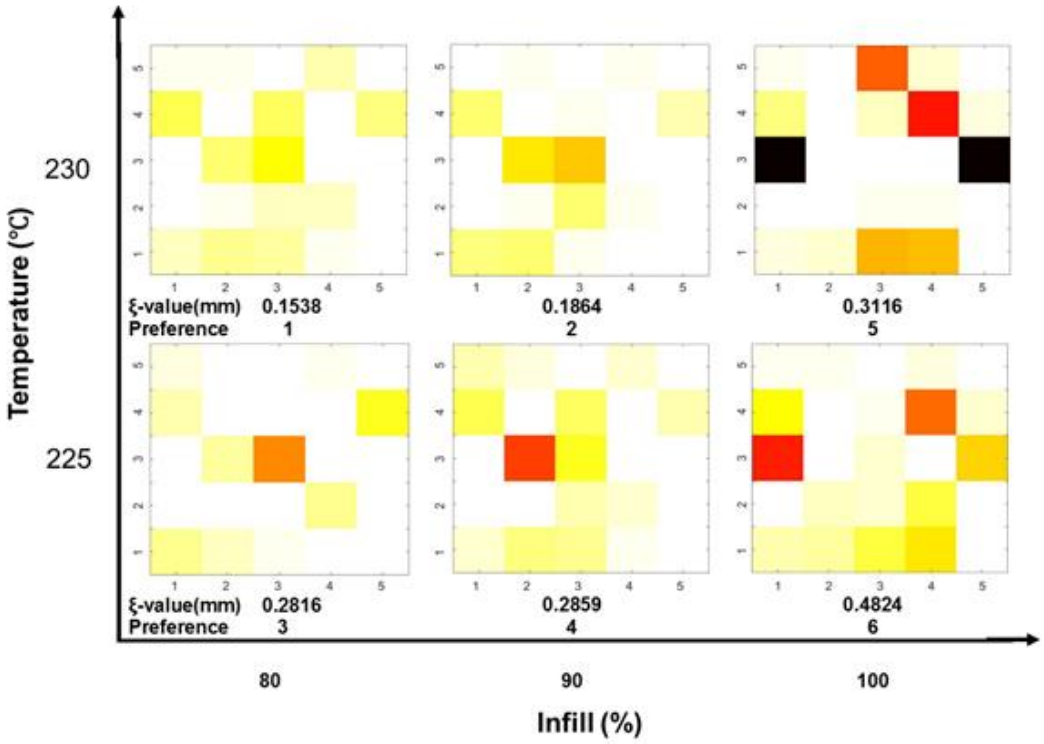

Figure 2.27 Comparing the geometric quality of printed parts using FFF where two-levels of (t_e= 225 °C and 230 °C) and three-levels of (I_f = 80, 90, and 100%) are selected using K-means clustering method.

2.10 Summary and conclusion

This chapter proposes using an unsupervised machine learning approach called self-organizing map to assess the geometric accuracy of AM parts from a large dataset of laser-scanned 3-D coordinates. The laser-scanned data is compared to the original CAD, and the resultant difference is used to characterize the geometric deviations of the as-built part. The central idea is that the clusters identified by the SOM are indicative of the magnitude (severity) and direction of geometric deviations. The approach was tested with experimental data obtained from laser-scanning of parts made with the Fused Filament Fabrication (FFF) AM process by varying infill percentage (I_f) and extruder temperature(t_e). The key findings of this work are summarized as follows:

(1) Laser-scanned 3-D point cloud data was used to assess the part geometric accuracy. Thus far, geometric dimensioning and tolerancing (GD&T) characteristics have been primary used to quantify the geometric accuracy of AM parts; this traditional approach was shown to be ineffective. GD&T characteristics need to be carefully customized to distinguish between parts made using different Fused Filament Fabrication (FFF) AM process conditions. Our approach provides a data-driven framework to profile the types of geometric deviations, which are uniquely defined by the design and process conditions. The overall geometric accuracy of the part is represented by a SOM map, extracted based on millions of data points.

(2) The SOM-derived clusters were able to discriminate between parts made with different FFF process conditions. The SOM-based analysis also recognized the magnitude and direction of deviations. It was observed that the geometric accuracy of FFF parts becomes worse with increase in infill percentage (I_f). This approach helps to advance the understanding about the effects of process parameters on not only the geometric accuracy of the whole part but also specific types of deviations. This is crucial for establishing the causal relationship between process/design parameters and geometric deviations of as-built parts. Once a specific type of deviation is identified during quality inspection, its root cause in the design space can be immediately pinpointed and adjusted to improve the part quality.

(3) The major clusters of SOM analysis only accounts for 2.4% of the total data points. In other words, instead of scanning the entire part and process the whole dataset of point cloud coordinates (millions of data points), which may be expensive and time-consuming, a small portion of the surface area recommended by critical clusters can be scanned and analyzed. This will drastically increase the scanning and processing speed (up to 50 times faster) of the AM specimens. This will also result in higher rate of quality inspection, without reducing the

accuracy of geometric integrity characterization, and eventually improve the quality and repeatability of AM parts.

Although the proposed clustering-based method is tested based on parts fabricated using a FFF system, the developed method for the profiling of geometric deviations can be applied to characterize the geometric accuracy of parts fabricated based on other AM systems, such as laser powder bed fusion (LPBF) and directed energy deposition (DED), or even other manufacturing processes. The insights from this work, open the following avenues for future research:

(1) Understanding not only the effect of process parameters on geometric accuracy after the build, but also prescriptive compensation and design rules to avoid shape deviation. Furthermore, the analysis presented herein must be extended to more complex shapes and finer features.

(2) Incorporating in-situ monitoring and assessment of geometric integrity using sensors, such as structured light scanners built into the machine.

(3) Integrating machine learning techniques, such as those proposed in this work with process modeling to understand why geometric inaccuracy occurs in additive manufacturing.

CHAPTER III

POROSITY PREDICTION: SUPERVISED-LEARNING OF THERMAL HISTORY FOR DIRECT LASER DEPOSITION

2.11 Introduction

The inadvertent defects of Additive Manufacturing (AM) parts result in low repeatability of AM products, which prevents wider adoption of AM technologies. One of the more detrimental microstructural properties associated with AM is porosity within final parts. The existing methods of defect detection/characterization mainly rely on *post-manufacturing* methods, such as X-ray computed tomography (CT), ultrasonic inspection, and many more [15, 18]. However, these post-manufacturing techniques are extremely expensive and time-consuming. Hence, there is an imperative need to develop methods for online detection/control of defects during the build. Establishing a quantitative relationship between the characteristics of melt pools and the formation of porosity in the as-built parts during the fabrication provide a rational solution to this predicament.

The characteristics of melt pools are expected to be highly correlated to abnormalities of microstructure, and thus defects in the fabricated parts[54]. Finite Element Modeling (FEM) has been developed to characterize the underlying thermo-physical process of AM, and predict the evolution of microstructure [56, 109]. These methods are mainly developed according to the specific part designs (e.g., cube, thin wall). Hence, tremendous efforts are needed to model the thermo-mechanical process while fabricating parts with complex geometries. Moreover, due to the

deterministic nature of most FEMs, process uncertainty is not taken into consideration. The predicted microstructure and mechanical behaviors tend to deviate from the actual manufacturing. Last but not least, FEMs usually require high computational costs, which will be difficult to implement for real-time monitoring/control.

To circumvent the challenges of modeling the complex thermo-physical process, supervised machine learning can be utilized to identify the patterns of melt pool images and its relationship to porosity. Melt pool morphological characteristics play a crucial role in determining the thickness of deposited layers, the microstructure evolution, and the pore formation. This has been studied extensively in [61-63]. Supervised learning builds a black-*box* model for the probability distribution of class labels (namely, porosity) based on data characteristics of predictors (e.g., melt pool characteristics). The class labels are defined as binary random variables that give the value of 1 if the melt pool is identified as porosity, and 0 otherwise. The resultant model does not depend on the specific design of specimens of material properties and can be effectively developed as long as thermal-porosity data can be obtained. To establish an accurate supervised learning model, a major challenge must be addressed: melt pool signals are represented by high-resolution images with varying sizes and shifting centers due to the dynamic thermal process. Using such ill-structured melt pool signals as predictors directly causes issues such as co-linearity and curse-of-dimension, which affects the prediction accuracy. Hence, dimension reduction and feature extraction procedures are needed to develop a structural predictor that captures the critical characteristics of melt pools. To address this challenge, we develop a methodology based on Functional Principle Component Analysis (FPCA), which extracts key characteristics of melt pools and converts it to smooth functional curves. The first few Principle Components (PCs) of these curves represent the major sources of variation in the thermal history, and thus are used as

the predictor of porosity. It is shown in Section 3 that Principle Components (PCs) of melt pool images can potentially distinguish normal melt pools from abnormal ones.

Once the melt pools are labeled via X-ray tomography, we apply multiple classification methods (i.e., Decision Tree (DT), K-Nearest Neighbor (KNN), Support Vector Machine (SVM), Linear Discriminant Analysis (LDA), and Quadratic Discriminant Analysis (QDA)) to establish the relationship between the PCs of melt pool images and the binary response that indicates the formation of porosity at the corresponding location. Cross validation is used for parameter tuning and model validation. In particular, the classification models are trained based on a randomly selected subset of the data and tested based on the remaining dataset. This procedure is repeated for multiple times to ensure that each data point is selected for both model training and testing. Figure 3.1 accounts for overall machinery of the supervised learning methods for porosity prediction.

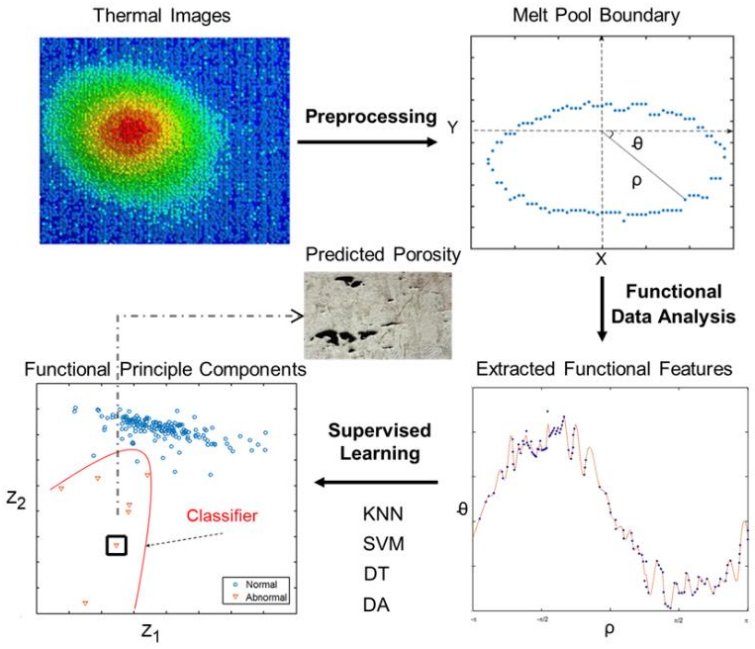

Figure 3.1 Demonstration of porosity prediction procedure using supervised machine learning.

We compare the accuracy of the proposed method that utilizes comprehensive melt pool characteristics with simple metrics of the melt pool such as length, width, peak temperature, area, etc. [15, 111]. Results show that porosity prediction using the simple metrics of the melt pool produces very poor accuracy measures compared to the morphological characteristics of the melt pool.

In summary, the technical contributions of this study to the existing literature are as follows:

1. We develop a novel data processing method for reducing the dimension of the thermal image data and extracting features relevant to the generations of porosity in the as-built parts.
2. The proposed method is compared with the studies in the literature, which mainly use the simple characteristics for thermal monitoring and control. Although such characteristics provide general information about the stage of the process, our comparison shows that using such simple characteristics are not sufficient for porosity prediction.
3. The proposed machine learning method for porosity prediction results in high recall value (98.44%), which provides a means to circumvent time-consuming porosity characterization.
4. Five supervised learning classification methods (i.e., Decision Tree (DT), K-Nearest Neighbor (KNN), Support Vector Machine (SVM), Linear Discriminant Analysis (LDA), and Quadratic Discriminant Analysis (QDA)) have been investigated. The most suitable classification methods for thermal-porosity relation have been identified and recommended.

2.12 Literature review

In this section, we survey the papers that discuss the existing porosity detection techniques.

2.12.1 Existing porosity detection techniques

The existing literature on porosity detection techniques can be broadly classified into three major areas: (1) porosity detection techniques based on post-manufacturing characterization, (2) visual based porosity detection techniques, and (3) simulation based porosity detection techniques.

2.12.1.1 X-ray computed tomography and ultrasonic

X-ray computed tomography or ultrasonic techniques have been the major mechanisms that are extensively used for post manufacturing characterization while detecting porosity. Many researchers have provided a higher level overview on the operations of the machine and how it can contribute to detect porosity in the parts. For instance, the benefits of using flash thermography against other approaches such as ultrasonic attenuation estimation have been investigated by Meola and Toscano [34] ,where the authors show that flash thermography is non-contact, cost-effective, and fast compared to other approaches. Through experiments, the authors have also found that by flash thermography, a part can be inspected while viewing the smooth or the rough side indifferently. For three-dimensional (3-D) defect characterization, analysis, and visualization, Wells has showed X-ray computed tomography modality using advanced Volume Graphics StudioMax (VGSM) voxel analysis and visualization software [35]. Porosity and some inclusions have been found in this study and the total defect level has been found to be 1.11% of the total casting volume. X-ray computed tomography method, involving image enhancement and ring artifact removal prior to image segmentation, has been proposed by Cai et al. [36], where the authors investigate the effect of process parameters on material porosity. The authors validate the

superiority of X-ray computed tomography over other conventional methods through several experiments.

Ultrasonic methods are primarily used for analyzing the porous structure, mechanical strength, and to detect internal defects [31]. Kim et al. [111] have investigated the procedure for estimating the porosity content of composite materials, which relies on the decomposition of the original ultrasonic pulse-echo signal into a sum of elementary wavelet contributions. This results in the reduction of complicated functions into several simpler ones, which are studied separately later. Eren et al. [27] propose three different ultrasonic approaches for characterizing porosity as well as for detection and imaging of different type of defects in the ceramic materials. Among the three approaches, the A-scan analysis has been found to be better suited for the detection of different type of defects in the ceramic tiles with a contact high-frequency longitudinal wave transducer. Air-coupled ultrasound is suitable for non-contact detection and the imaging of defects in ceramic tiles. Finally, frequency dependence of attenuation is the most appropriate one for the quantification of porosity. Interested readers can review the works by [28-30, 32] for details about ultrasonic inspection of AM parts.

Few researchers have investigated the possibility of detecting anomalies while building the parts and taking steps to correct them in a real time manner. Among these studies, Fan et al. [38] have proposed an online surface defect detection system with in-built image processing methodology leveraging the optical system design. Simultaneously, the authors also have developed an analysis algorithm that removes the noise from porous images, detects object edges, and uses hybrid-based method to determine the defects in the parts. Schwerdtfeger et al. [37] have investigated the possibility of in situ anomaly detection for Ti-6Al-4V parts, where the authors have observed strong correlation between the patterns visible in infrared images and

metallographic images. This correlation specifies anomalies through variation in color density in images. This provides a unique procedure for in situ quality control as anomalies can be repaired in real time using appropriate repair methods (e.g., re-melting of the compromised area, additional powder deposition and re-melting of the compromised area, and many more).

Apart from these studies, a stream of simulation based methods are available in the literature that have been developed to predict anomalies (e.g., [61, 112-114]). However, these methods require integrating X-ray computed tomography to validate the results obtained via simulation methods.

Limitations of the existing post-manufacturing porosity detection methods lie in the high cost associate with the process, longer process time, and the lack of capability to characterize pores during manufacturing. On the other hand, outputs from the visual and simulation based porosity detection methods can be far from actual yields because they are often incapable of taking into account the uncertainty that results from material or process parameters.

2.13 Data characterization and processing

To label the melt pool data, 3-D CT is used to empirically locate the defects in the part. By doing so, we can validate the efficiency of the proposed method against real results. Note that the 3-D CT is an advanced X-ray inspection technique that forms three-dimensional (3-D) representations of an object by capturing numerous X-ray images around an axis of rotation and using algorithms to reconstruct a 3-D model [73]. The CT method used in this study utilizes a full 3-D cone of X-ray with a 2-D detector. This cone beam scanner irradiates the whole object throughout the scan. It moves through 360˚to obtain data for the entire object [71]. This technique identifies the shape and size of the pores within the thin-wall specimen, which cannot be identified individually. More specifically, the system can detect pores with the size ranging from 0.05 mm

to 1.00 mm. However, pores with a diameter less than 0.05 mm are difficult to identify. Such small size pores tend to have less impact on the mechanical strength and fatigue of parts.

2.13.1 Functional Principle Component Analysis (FPCA) of melt pool images

Although the Cartesian coordination of the data (shown in Figure 3.2(a)) is analogous to real melt pool shape, it cannot be represented in a functional form. Hence, polar transformation is applied to the morphology of top surface of the melt pool to obtain the value of θ_i and ρ_i that is shown in below, i.e.,

$$(\theta_i, \rho_i) = p(X_i, Y_i) = \left(arctan\left(\frac{Y_i}{X_i}\right), \sqrt{(X_i^2) + (Y_i^2)} \right) \qquad i = 1,2, \dots, n \qquad (3.1)$$

n is the total number of points in the circumference of the melt pool. The morphological melt pool model after polar transformation is shown by the blue dots in Figure 3.2(b). More specifically, we extract the boundary of the melt pool and represent it using the polar coordination system. Existing studies have demonstrated that the characteristics of the boundary (e.g., size, depth, length, width, and many more) are crucial for the formation of microstructure anomalies [14, 15, 115]. Hence, each melt pool contour can be represented using a function. Let us define $\rho = \rho(\theta)$ where $\theta \in (-\pi, \pi)$. As shown in Figure 3.2 below, ρ represents the distance between the center of the melt pool (defined based on the peak temperature) and the melt pool boundary.

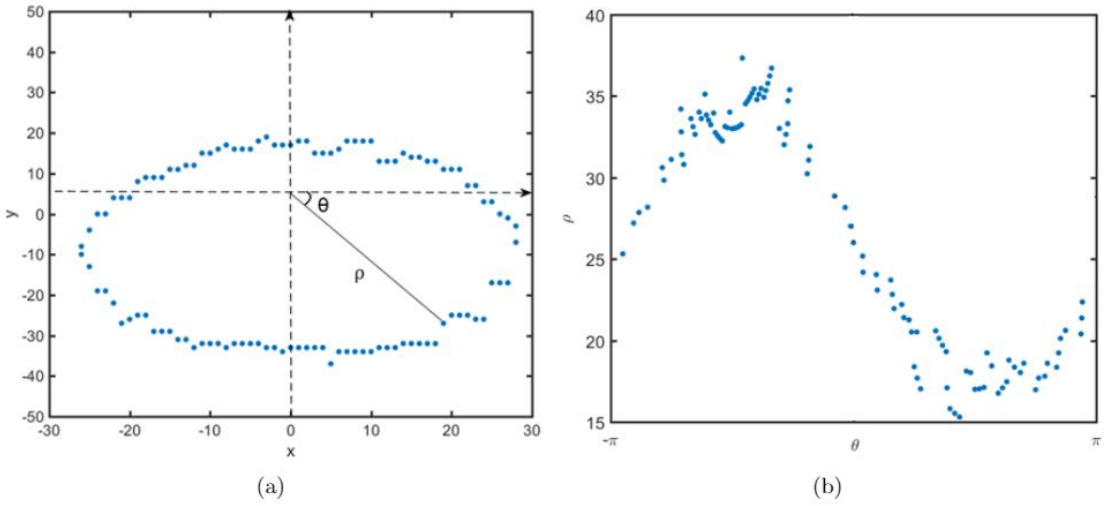

Figure 3.2 Polar transformation of melt pool boundaries (a) shows the Cartesian Coordinates of the melt pool boundary and (b) shows the morphological model after polar transformation.

Functional Principle Component Analysis (FPCA) is applied to $\rho = \rho(\theta)$ to fit a smooth functional curve and extract critical features. This essentially comprises of two steps: (1) Curve fitting via cubic spline smoothing that connects discrete data points with piecewise cubic functions while guaranteeing the smoothness of the function [116, 117]. This method has been applied commonly for phase field computations in chemicals [118], image processing in disease detection [119], and many more. Thus, this method can be considered as a suitable tool to handle the melt pool data. (2) Identifying the principle components using FPCA. FPCA is applied to extract the pattern of variation exhibited in $\bar{\rho}(\theta)$. FPCA reduces the functional data to a given number of components such that the representation is optimal in terms of its $\mathcal{L}^2$(Hilbert space) accuracy. It can handle functional data that cannot be analyzed directly using PCA. Details of these steps are provided below.

Step 1: *Curve fitting via cubic spline smoothing*

Assume that a melt pool boundary consists of $n + 1$ (θ_i, ρ_i) pairs.

$$\bar{\rho}(\theta) = \begin{cases} \bar{\rho}_1(\theta) & \theta_0 < \theta < \theta_1 \\ \bar{\rho}_i(\theta) & \theta_{i-1} < \theta < \theta_i \\ \bar{\rho}_n(\theta) & \theta_{n-1} < \theta < \theta_n \end{cases} \quad (3.2)$$

For any $i = \{1,2, \dots, n\}$, $\bar{\rho}_i(\theta)$ is a cubic function represented as follows:

$$\bar{\rho}_i(\theta) = a_i + b_i\theta + c_i\theta^2 + d_i\theta^3 \quad (3.3)$$

To determine the spline, coefficients a_i, b_i,c_i, and $d_i$for each i must be estimated. Note that since there are n intervals, $4n$ coefficients need to be estimated using the following three key conditions,

- Spline has to be exact at the data points, i.e.,

$$\bar{\rho}_i(\theta_{i-1}) = \rho_{i-1}\,, \bar{\rho}_i(\theta_i) = \rho_i \quad (3.3)$$

- Continuity of first and second derivative must be maintained, i.e.,

$$\bar{\rho}_i'(\theta_i) = \bar{\rho}_{i+1}'(\theta_i)\,, \bar{\rho}_i''(\theta_i) = \bar{\rho}_{i+1}''(\theta_i) \quad (3.4)$$

- The natural boundary condition must be maintained, i.e.,

$$\bar{\rho}_1''(\theta_0) = \bar{\rho}_n''(\theta_n) \quad (3.5)$$

Cubic spline curve fitting, including the estimation of coefficients (a_i, b_i,c_i, and d_i) can be performed using MATLAB.

Step 2: *Identifying the components of $\bar{\rho}(\theta)$ using FPCA*

The method of FPCA is summarized as follows:

Let us assume $\bar{\rho}_j(\theta)$ accounts for profile of the melt pool j after spline curve fitting is applied. Simultaneously, $f_{j,1}$ represents the first principle component score function for melt pool j, which can be calculated as follows:

$$f_{j,1} = \int \varepsilon_1(\theta)\bar{\rho}_j(\theta)d\theta \quad (3.6)$$

$\varepsilon_1(\theta)$ is a weight function. The first step in FPCA is to maximize $\sum_j {f_{j,1}}^2$ that is subject to $\int {\varepsilon_1}^2(\theta)d\theta = 1$. Next, we need to compute the weight function $\varepsilon_2(\theta)$ that satisfies the orthonormal property (i.e., $\int {\varepsilon_2}^2(\theta)d\theta = 1$ and $\int \varepsilon_2(\theta)\varepsilon_1(\theta)d\theta = 0$). Following these properties, $\sum_j {f_{j,2}}^2$ has to be maximized and the process continues. The resultant equation is an eigenequation that can be expressed as follows:

$$\int v(\theta', \theta)\varepsilon(\theta)d\theta \quad = \quad \lambda\, \varepsilon(\theta') \tag{3.7}$$

where $v(\theta', \theta)$ is the sample variance-covariance function, λ is an eigenvalue, $\varepsilon(\theta')$ is an eigenfunction of variance-covariance function. There are different methods to solve the eigenequation such as discretization of the functions, basis function expansion of the functions, general numerical quadrature, and Gaussian quadrature [120]. In this study, discretization of the functions method is utilized from the FPCA package in MATLAB to solve the eigenequation. Subsequently, the components that account for the majority of the variation in data are determined.

In our study, it has been found experimentally that the first nine components accounts for 99.52% of the variation in data (see Figure 3.3(a)). Moreover, as evident from Figure 3.4(a)-3.4(d), it is obvious that using up to two components accounts for majority of the variation (i.e., 89.57%). Figure 3.4(a) shows the original melt pool profiles. In Figure 3.4(a), *blue* and *orange* positive (+) signs denote the upper and lower bounds for ρ values, respectively. Figure 3.4(c) and Figure 3.4(d) show the first and second principal components curve, which points are estimated from discretization approach and curves are the estimates from expansion of Fourier series on θ, respectively. Figure 3.4(b) shows morphological model of melt pool using only the first (z_1) and second (z_2) principal components where same as before blue and orange positive (+) signs denote

the upper and lower bounds for ρ values, respectively. More specifically, it explains approximately 89.57% of the variation in data (as shown in Figure 3.3(a)). The rest of the six components account for 9.95% of the variation in the data. From Figure 3.3(b), it is observed that abnormal melt pools are captured by specific range of the first two components (i.e., z_1 and z_2). Generally, lower values in both z_1 and z_2 are associated with abnormal melt pools whereas larger values tend to result in normal melt pools. In the next section, we will investigate multiple classification methods to predict whether a melt pool is abnormal based on its $\{z_1, z_2, \dots, z_9\}$ values. However, only z_1 and z_2 are used for demonstration purposes.

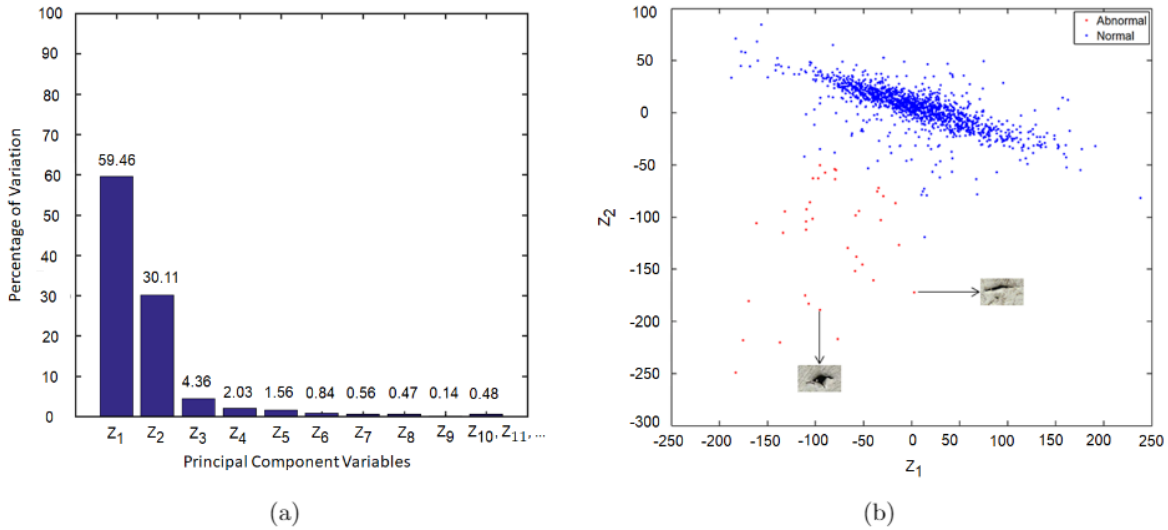

(a) (b)

Figure 3.3 Dimension reduction procedure using FPCA where (a) shows the percentage of variation for the first 10 principle components, and (b) demonstrates the scores for two principle components (z_1 and z_2). The blue dots represent normal melt pools and red dots represent abnormal melt pools that results in porosity of as-built parts.

2.14 Supervised learning for the classification of melt pools

Supervised learning is the machine learning method of inferring a function from supervised training data. Supervised learning algorithms usually contain a set of input samples and

corresponding labels are associated with that data. The goal of a classifier is to find a suitable boundary that can predict correct labels on test data. To explain briefly, in supervised learning, each example can be considered as a pair consisting of an input object and a desired output value. A supervised learning algorithm analyzes the training data and produces an inferred function. This function is called a *classifier* or a *regression function* [121, 122].The inferred function should predict the correct output value for any valid input object.

Four different types of classification methods have been used: K-Nearest Neighbors (KNN), Support Vector Machine (SVM), Decision Tree (DT), and Discriminant Analysis (DA). Although very few classifiers have been used for porosity or anomaly detection purpose for AM parts, various studies are available in the literature that utilize the aforementioned classification methods for several other purposes such as network intrusion detection [115, 123, 124], detection of epileptic seizure in Electroencephalogram (EEG) signals[125], change detection of images [126], disease specification[125], face recognition [127], and many more. This study is one of the introductory studies that uses classification methods for porosity detection in AM parts using melt pool thermal profile characteristics.

We formulate the classification of melt pools as follows:

$$\mathbf{Y} = f(z_1, z_2, \dots, z_9) \tag{3.8}$$

where $\mathbf{Y}$ is the binary random variables that indicates whether the melt pool results in porosity at the corresponding location. More specifically, $\mathbf{Y} = 1$ if the melt pool results in porosity; $\mathbf{Y} = 0$ otherwise. The classifier is represented by $f(\cdot)$ that links melt pool characteristics $(z_1, z_2, \dots, z_9)$ to $\mathbf{Y}$. In what follows, we use four classification methods: (1) K-Nearest Neighbors (KNN), (2) Support Vector Machine (SVM), (3) Decision Tree (DT), and (4) Discriminant Analysis (DA). We also investigate two variants of DA: (1) Linear Discriminant Analysis (LDA) and (2) Quadratic

Discriminant Analysis (QDA). The corresponding results for each approach demonstrated in sections 3.4.1-3.4.4.

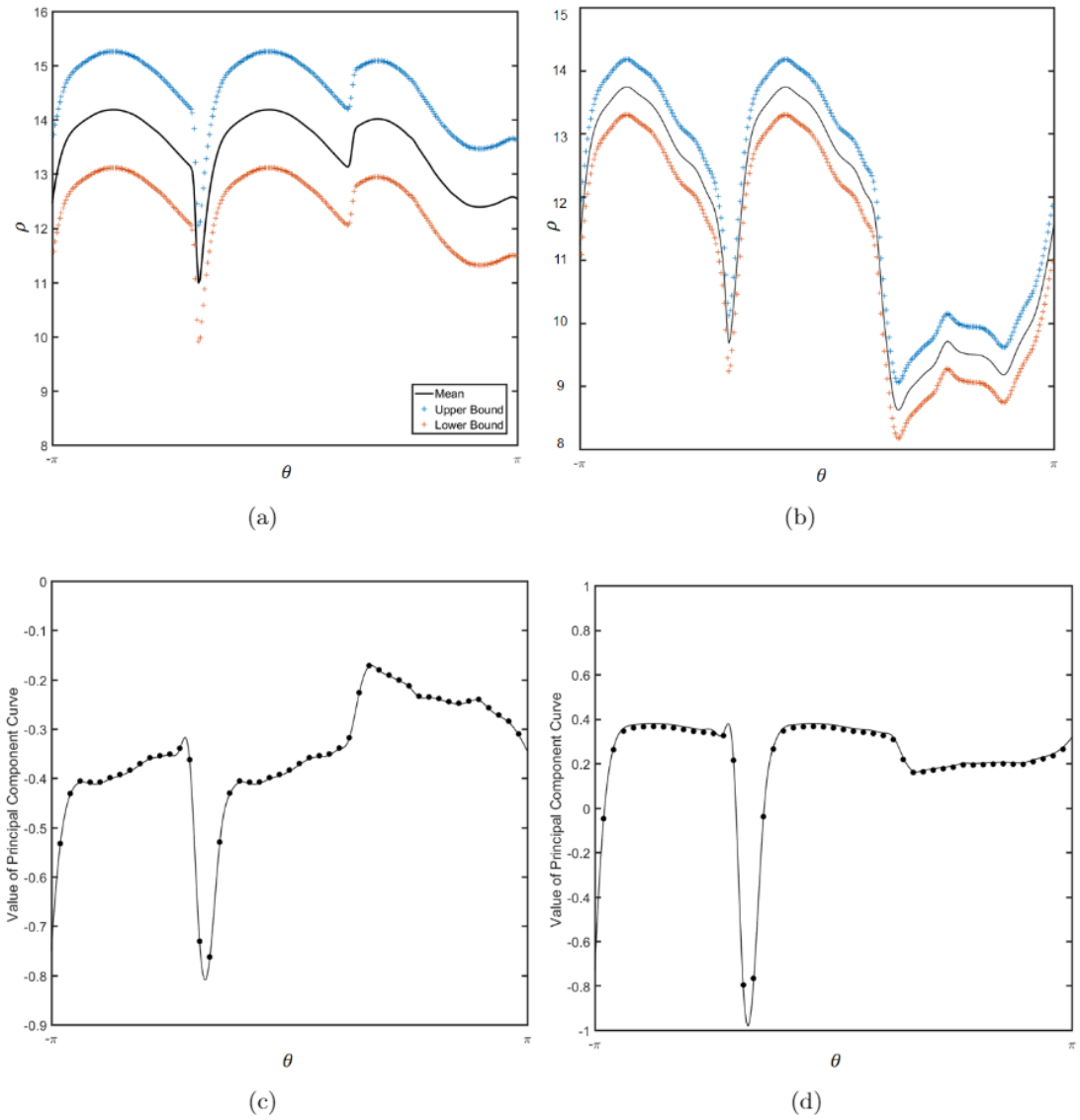

Figure 3.4 Demonstrating melt pool morphological model with first two principal components where (a) shows the original melt pool profiles in polar coordinates, (b) shows morphological model of melt pool using only the first (z_1) and second (z_2) principal components and (c) and (d) show first and second principal components curve. Scattered data points in (c) and (d) are estimated from discretization approach and curves are the estimates from expansion of Fourier series on θ.

2.14.1 K-Nearest Neighbors (KNN)

Figure 3.5(a) and 3.5(b) demonstrate the results of KNN algorithm, where z_1 and z_2 are two PCs that are used to classify melt pools. Query points (*triangle*) are generated that need to be classified into normal (*blue* circle) or abnormal melt pools (*red* circle). Based on the Euclidean and Minkowski distance measure (with $p = 0.8$), nearest data points to the queries are determined (circular region around data points) that are shown in Figure 3.5(a) and 3.5(b). The labels of query points are fixed based on the type of melt pools are closer to them.

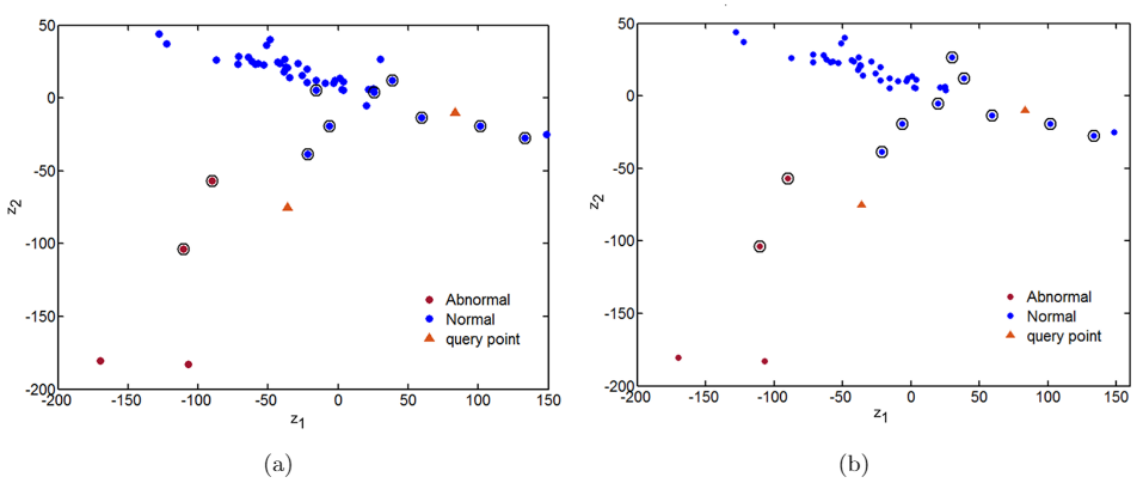

Figure 3.5 K-Nearest Neighbor model for z_1 and z_2 for the different melt pools where (a) the Euclidean distance and (b) the Minkowski distance (with $p = 0.8$) are used to classify melt pools as abnormal or normal.

2.14.2 Support Vector Machine (SVM)

Figures 3.6(a) and 3.6(b) show the SVM classification using a Gaussian kernel and a polynomial kernel. Normal and abnormal melt pools are denoted by *blue* and *red* dots respectively. Support vectors are used (circular region around red or blue dots) to create the hyperplane that are used to classify the entire dataset.

2.14.3 Decision Tree (DT)

Figure 3.7 demonstrates a decision tree that predicts classifications based on two predictors, z_1 and z_2. To predict the melt pool class, start at the top node, which is represented by a triangle. The first decision is whether z_2 is less or more than -56.7957. If z_2 is less than -56.7957, the left branch is followed and it is checked whether the value of z_1 is less or more than 6.34188; otherwise, the right branch is followed. The branches are pruned if a decision can be made regarding the normality or abnormality of melt pool.

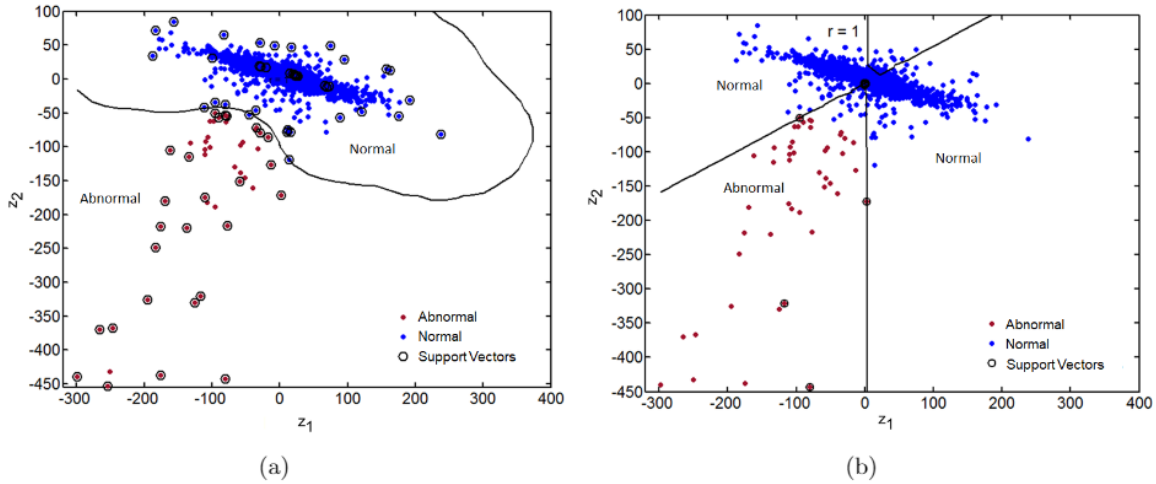

Figure 3.6 SVM classification with (a) Gaussian kernel function and (b) polynomial kernel function.

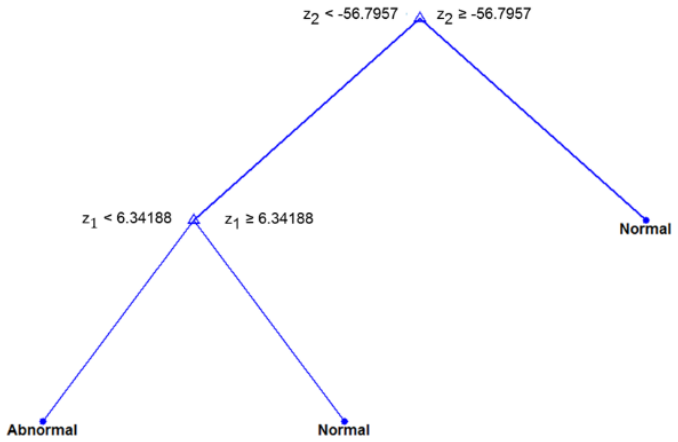

Figure 3.7 An example of classification tree using the first two principle components (z_1 and z_2).

2.14.4 Discriminant Analysis (DA)

Figure 3.8(a) shows the LDA results. A linear classifier is created based on the concept of discriminant analysis. This results in three coefficients K,$L(1)$, and $L(2)$ for the linear boundary between the normal and abnormal melt pool. Finally, a curve is generated (red line in Figure 3.8(a)) that partitions the data into two sets. In Figure 3.8(b), a quadratic discriminant classifier is created. Coefficients for the quadratic boundary between normal and abnormal melt pools are retrieved and a curve is plotted (red line in Figure 3.8(b)) that separates the normal and abnormal melt pools. QDA usually provides better solution compared to LDA as it captures more anomaly due to the shape of the defined boundary. Figure 3.8(a) and Figure 3.8(b) show that abnormal melt pools are more clearly distinguished in QDA.

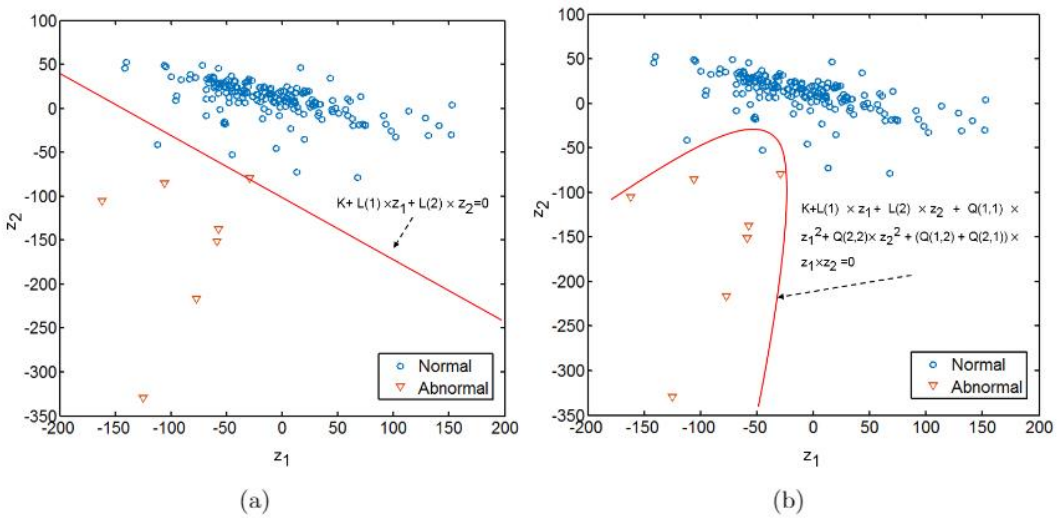

Figure 3.8 Illustration of Discriminant Analysis (DA) classification procedure where (a) indicates the linear score function for DA and (b) the quadratic score function for DA.

2.15 Comparison and benchmark

This section discusses the numerical experiments conducted to predict porosity of AM parts. We first start with implementing the FPCA to reduce the dimensionality of the data. With the FPCA, it has been found experimentally that utilizing up to 9 components (i.e.,$z_1, z_2, \dots, z_9$) accounts for almost 99.52% of variation in the data.

Some of the classification methods contain some sensitive tuning parameters that need to be estimated properly as these parameters significantly affect the efficiency of the classification methods. Hence, obtaining the best possible set of tuning parameters is very crucial, both from the perspective of reducing computational cost and increasing computational accuracy. Afterwards, using the selected parameters, all the classification methods are validated. Finally, the accuracy of the proposed method using morphological model is benchmarked against using melt pool simple metrics.

2.15.1 Model validation

Among the five different classification methods, only KNN and SVM have parameters that need to be tuned since the behavior parameters of SVM and KNN influence their performance.

Hence, we need to perform parameter tuning via k-fold validation, which has been widely applied to identify/select the appropriate types and values of parameters for classification methods (e.g., SVM, KNN). k-fold cross-validation (sometimes referred to as "rotation estimation") is a model validation technique where the dataset Z is randomly split into k mutually exclusive subsets of approximately equal size. Each classification process is trained on $Z \backslash Z_t$ (Z does not includeZ_t),$t \in \{1,2,\dots,k\}$, k times and tested on Z_t. The cross-validation estimate of accuracy is the overall number of correct classifications divided by the number of instances in the dataset [128]. Two different measures (M_1 and M_2) are developed to evaluate the accuracy of the classification approaches. The concept of M_1 and M_2 can be explained from the perspective of True Negative (TN), False Positive (FP), False Negative (FN), and True Positive (TP). If the pores predicted by the proposed method are actually pores, it is denoted by TP. On the contrary, if the pores predicted by the proposed method are actually normal melt pools, it is denoted by FN. If the normal melt pools are incorrectly classified as pores, it is labeled as FP. Last, if normal melt pools are labeled as normal melt pools by the proposed method, it is denoted as TN. The above definitions are summarized in Table 3.1.

Table 3.1 Demonstrating the confusion matrix with model performance measures.

		Predicted	
		Normal	Abnormal
Actual	Normal	TN	FP
	Abnormal	FN	TP

Hence, M_1 is the probability of correctly predicting an abnormal melt pool while M_2 is the probability of incorrectly predicting a porosity.

The tuning process for the classification model is accomplished by randomly selecting 64% of data as train set and 16% as test set. This process is repeated 60 times to select the appropriate distance method as well as the number of neighbors (K) for each query point of the KNN classification method.

Table 3.2 demonstrates the best distance method for KNN. On average, for 60 trials, the Euclidean distance method provides the best values for M_1 and M_2. Higher values for M_1 and lower values for M_2 are preferred. After selecting the distance method, the number of neighbors (K) are chosen. Results from Table 3.3 show that when the number of neighbors is set to 4, the accuracy measures provide the best result.

Table 3.2 Selecting distance method for KNN classification.

Distance	$\boldsymbol{M_1}$	$\boldsymbol{M_2}$
Manhattan ($\boldsymbol{\mathcal{L}^1}$-norm)	0.9588	0.0030
Euclidean ($\boldsymbol{\mathcal{L}^2}$-norm)	**0.9844**	**0.0020**
Minkowski	0.9513	0.0067
Cosine	0.9692	0.0056
Correlation	0.9623	0.0042

Finally, for SVM classification, the *kernel function* is known to provide high quality classification of the data[129] . Hence, three kernel functions are tested and it has been found that *polynomial kernel function* provides the best result in terms of accuracy measures M_1 and M_2, as shown in Table 3.4.

Table 3.3 Number of neighbors (K) for query points based on Euclidean distance method for KNN.

K	M_1	M_2
4	**0.9947**	**0.0027**
5	0.9874	0.0014
6	0.9896	0.0027
7	0.9621	0.0014
8	0.9700	0.0021
9	0.9543	0.0020
10	0.9449	0.0015
11	0.9239	0.0012
12	0.9227	0.0009

Table 3.4 Selecting the appropriate kernel function method used in support vector machine (SVM).

Kernel Function	M_1	M_2
Linear	0.9070	0.0033
Gaussian	0.0000	0.0000
Polynomial	0.9797	0.2215

Leveraging the tuning parameters selected in the previous section and choosing the K-fold cross-validation method, the entire dataset is used for experiment where 80% of the dataset is used for training while the remaining 20% is used for testing. Hence, the value of k is set to be 5. The process is repeated for 60 trials, and the average values for accuracy measures are reported. Figure 3.9 shows the accuracy measures for all the classification methods used in this study. Results indicate that KNN provides the highest value for measure M_1 (98.44%); however, for measure M_2, DT gives the best result with false negative value of only 0.033%.

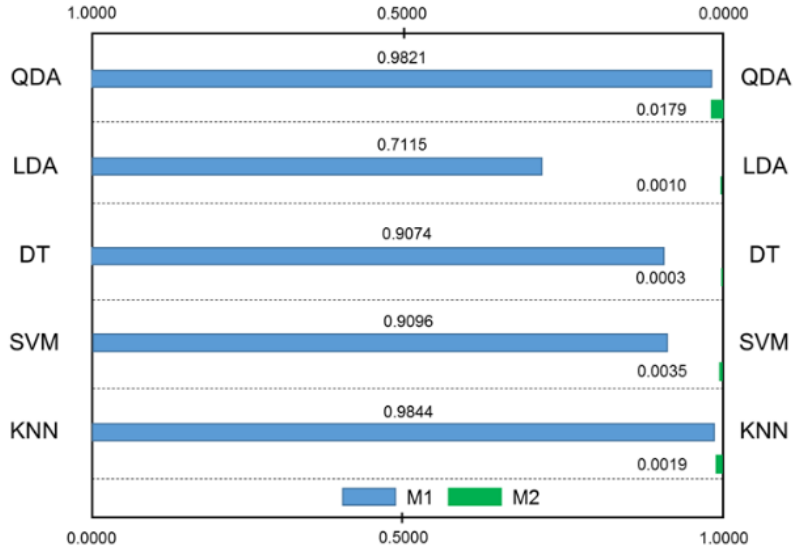

Figure 3.9 Comparing the accuracy measures for the classification methods. The lower horizontal axis is for M_1 and upper horizontal axis is for M_2.

2.15.2 Benchmark against morphological characteristics of melt pools

The majority of the existing melt pool monitoring/modeling approaches focus on simple metrics, such as the size, length, peak temperature, and others [14, 54, 56]. These approaches focus primarily on relating process parameters to the melt pool size, characterizing the interdependence between the melt pool height and laser power, estimating the motion of the melt pool's free surface in uninterrupted cladding, and many others. Hence, these simple metrics are used to demonstrate the advantage of using morphological descriptors for predicting porosity. For the simple metrics of melt pool, the features can be represented in matrix form shown by equations as follows:

$$\Gamma = [\gamma(i)], i = \{1,2, \dots, N\} \text{ where } \gamma(i) = \left(\gamma_1^i, \gamma_2^i, \dots . , \gamma_p^i\right) \quad (3.9)$$

Simple metrics contain a limited number of features as shown in Table 3.5. Graphical representation of the extracted simple metrics is provided in Figure 3.10.

Table 3.6 Simple metrics.

Feature notation	Metric
γ_1	Circumference
γ_2	Length
γ_3	Width
γ_4(TL)	Top Left area
γ_5(TR)	Top Right area
γ_6(BL)	Bottom Left area
γ_7(BR)	Bottom Right area
γ_8	Total Area
γ_9	Longest Axis

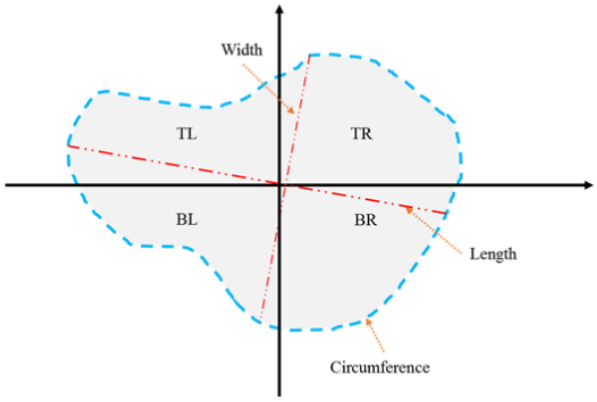

Figure 3.10 Schematic of an example melt pool explaining some of the extracted simple metrics: circumference (dotted line), length, width, total area (shaded), longest axis, and the areas of each of the quadrants (TL, TR, BL, BR).

Nine components are investigated by Principle Component Analysis (PCA) to determine which component or group of components account for the highest proportion of variation in the data. Experimental results show that considering up to four components account for almost 99% of the variability in the data. With these four independent components, different classification approaches are applied to predict the pores in the AM part. Following the same tuning procedure

described in Section 4.5.1, it has been experimentally found that the cosine distance is better for KNN with four neighbors (K=4). Similarly, polynomial kernel function has been found to provide superior performance for SVM.

The selected tuning parameters and the k-fold cross-validation method are simultaneously used for the entire dataset where 80% of the dataset are used for training and 20% are used for testing. Figure 3.11 shows the accuracy measures for all the classification methods with simple metrics. SVM provides the highest value for measure M_1 (28.32%). However, for measure M_2 LDA gives the best result with false negative value of only 0.57%. Although SVM outperforms other classification methods with simple metrics, its performance is worse compared to other classification-based approaches used with the morphological model. For instance, for the measure M_1, the best classification method for morphological model (KNN) provides a much better performance compared to SVM with simple metrics (M_1 of 28.32% with SVM versus M_1 of 98.44% with KNN, approximately a 250% improvement). The same trend is followed by M_2 for the best classification methods for each model. This shows that morphological model captures more sophisticated information compared to simple metrics that can be used for porosity prediction. Table 3.6 provides the comparative quantification of the superiority of the morphological model over the simple metrics.

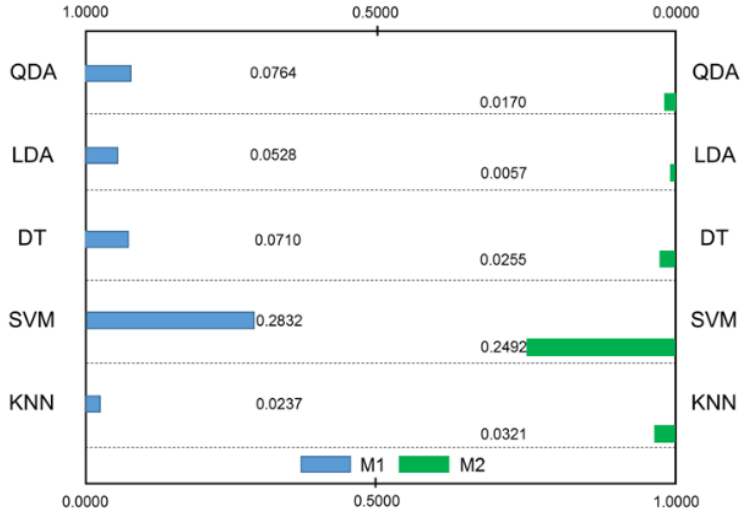

Figure 3.11 Comparing the accuracy measures for the classification methods with simple metrics.

Table 3.6 Comparing best accuracy measures between simple metrics and morphological model.

Melt Pool model	M_1	M_2
Simple metrics	28.32%	0.57%
Morphological model	98.44%	0.03%
(%) Improvement	247.62%	94.15%

2.16 Conclusions

The wider adoption of AM technologies in strategic industrial sectors require techniques that improve the quality of parts, namely, microstructure anomalies, such as porosity and mini-cracks. This study proposes a porosity prediction scheme via supervised machine learning of melt pool thermal image streams for the AM parts. Major findings of this study are summarized below:

(1) Existing porosity prediction/detection methods focus primarily on post-manufacturing approaches that are susceptible to high cost of process, longer process time, and are incapable

of characterizing pores during fabrication. We propose a machine learning framework to establish a relationship between melt pool morphological characteristics and anomalies in the microstructure. Melt pool thermal image streams are first used to develop the morphological model. The central hypothesis is that the morphological model contains significant information regarding the microstructure properties of the part that can be directly correlated to the mechanical properties, which is a major indicator of part quality.

(2) A novel data processing procedure is proposed that is capable of converting ill-structured melt pool image streams to continuous morphological model with the identical function support. Once melt pool images are defined in the same domain, supervised learning techniques are applied to dichotomize the melt pools to predict the anomalies in the part. The melt pool dataset is labeled using the information captured via X-ray tomography. Afterwards, based on the labels (i.e., normal melt pools or pores), accuracy measures are applied to evaluate the performance of the supervised learning methods.

(3) Among the supervised learning techniques, K-Nearest Neighbor (KNN) provides the highest rate of recall (98.44%). However, Decision Tree (DT), gives the least value for incorrectly identifying normal melt pools as pores (0.03%) where corresponding value for KNN is not high (0.19%).

(4) A comparative study is conducted that compares the performance of supervised learning methods leveraging the proposed morphological model and simple metrics of the melt pool. Numerical experiments show that morphological model combined with supervised learning techniques vastly outperform the simple melt pool metrics combined with supervised learning techniques (approximately 250% better performance for correctly predicting abnormal melt pools).

As long as the material is deposited via the solidification of a melt pool, the developed framework can serve as a real-time X-ray CT for other AM processes that share similar energy-material interactions (e.g., Powder Bed Fusion, Electron Beam Melting). By capturing the melt pool anomalies, the method presented herein can potentially capture the microstructure anomalies in real time.

CHAPTER IV

DUAL PROCESS MONITORING OF METAL-BASED ADDITIVE MANUFACTURING USING TENSOR DECOMPOSITION OF THERMAL IMAGE STREAMS

4.1 Introduction

The recent decades have witnessed a rapid growth in metal additive manufacturing (AM) processes for functional parts production within many industrial sectors (such as aerospace, tooling, and biomedical applications [1]). Ranging from customized to large-scale manufacturing, AM parts can have unique geometries, can be functionally-graded, or can be custom-tailored lightweight structures—features that can be impractical or burdensome for traditional manufacturing processes [3]. Despite advancements in AM for non-structural applications, the lack of understanding of its process-structure-property relationships are a primary hurdle for adopting metal AM systems in industry applications [3-7]. Improving the quality and repeatability of additively manufactured parts is essential to fulfill the demanding requirements and certification constraints for applications with high quality requirements (e.g., healthcare, aerospace).

Our objective is to develop an *in situ* monitoring methodology based on thermal image streams for online prediction of anomalies in the internal structure of the AM parts. Understanding different types of anomalies (e.g., porosity, balling, geometric deviations, microstructural heterogeneities and impurities) and their forming mechanisms can facilitate the design of process monitoring and control methodology. The existence of anomalies in the internal structure of AM parts is a critical issue in AM processes, which leads to compromised functional performance of

the final parts. Although post-manufacturing methods can remove some anomalies in the AM parts, *in situ* process monitoring and predicting part anomalies in real time could enable potential corrective actions during the fabrication to reduce the overall AM cost (e.g., equipment, material, post processing, and turnover).

In this study, the thermal image stream is used to develop an *in situ* monitoring methodology because it is regarded as one of the most informative signatures of thermo-physical dynamics in directed energy deposition (DED) processes [130]. In the thermal images, the region of superheated molten metal in proximity to the laser-material interface, namely the melt pool, is known to contain primary process information [3]. Characteristics of the melt pool, including stability, dimension, thermal distribution, and dynamic behaviors, directly reflect process stability and part quality. Most of the existing studies in the literature used four major features extracted from the melt pool (i.e., its size, shape, temperature intensity, and thermal profile) to monitor the process [14-17, 131, 132]. Primary purpose of these monitoring approaches is linking process parameters to the melt pool size, characterizing the interdependence between the melt pool height and laser power, estimating the motion of the melt pool's free surface in uninterrupted cladding, etc. There are also methods developed using physics-based differential equations that account for thermo-physical characteristics of the process [18, 19]. The major limitations of these methods include, (1) the deviation of simulated thermal history from reality and (2) the lack of capacity for capturing the uncertainty during the fabrication [20].

Online process monitoring for AM systems is still in its preliminary stage, and most of the existing studies focus on studying the effect of process parameters and material properties on process signatures (e.g., the melt pool, the powder bed, the slice). In other words, most of the monitoring methods in the literature are concerned with *in situ* data measurement and feature

extraction techniques based on *sensing systems* rather than online anomaly detection. On the other hand, statistical process monitoring refers to automated change/anomaly detection based on monitoring statistics with a known distribution under normal operation conditions. A few of existing studies proposed automated approaches to detect anomalies in an online manner [133, 134].

In this paper, the research objective is to develop an online monitoring technique to quickly detect and diagnose anomalies during the build of AM parts as shown in Figure 5.1 . Based on the features extracted from thermal image streams using multilinear principal component analysis (MPCA), we propose a dual statistical process monitoring approach, which combines image feature extraction and dimension reduction methods to identify the local defects/anomalies (i.e., porosity) in AM processes. Note that in melt pool signal analysis there are numerous challenges including large data volume, low signal-to-noise ratio, ill-structured data (e.g., misalignment among different melt pools), and missing data measurements. To address these challenges, we propose an MPCA-based image processing methodology: (1) We define an identical square-shaped support based on the historical thermal images that covers the entire melt pools in their respective images as the Area of Interest (AOI). AOI contains the most important information in the melt pool and encompasses synonymous/commensurate thermal features for all images. Thus, the extracted information of thermal history is robust against the varying shapes and drifting locations melt pools during the fabrication. (2) Subsequently, image filtering technique (i.e., convolution) is applied to the discrete temperature measurement arrays so that missing data measurements can be estimated. The convolution approach was extensively used for the estimation of randomly missing values of 3-D discrete data (e.g., images)[135, 136]. (3) We further propose an MPCA-based dimensionality reduction procedure. MPCA is one of the well-known low-rank

tensor decomposition methods, which maintains the natural tensor data structure and reduces data dimension in a more effective way than its traditional counterparts, such as the classical principal component analysis (PCA) and its 2D variant (2D PCA)[137]. (4) A dual control charting system leveraging a T^2 and a Q chart is proposed to simultaneously monitor the extracted MPCA features and the residual after extracting MPCA, respectively.

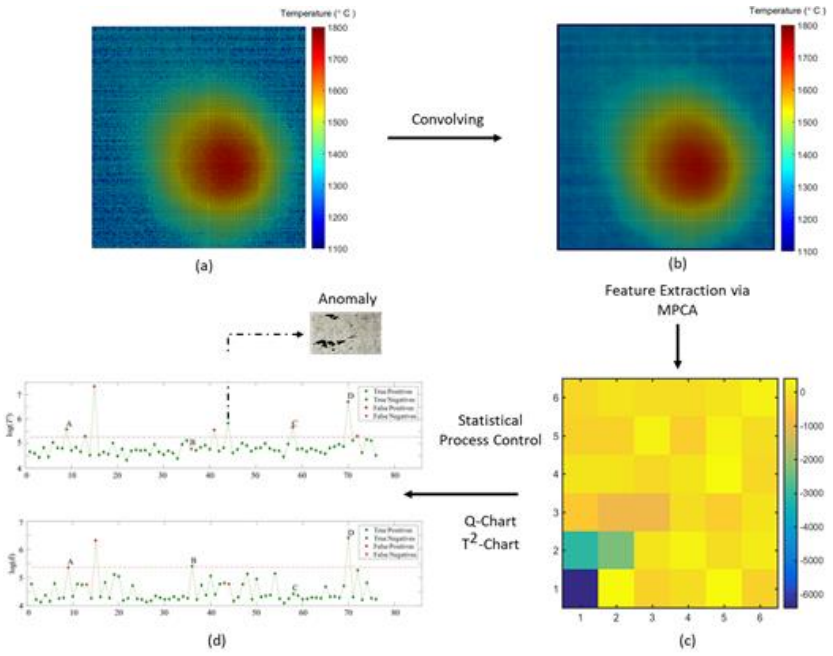

Figure 4.1 Demonstration of online anomaly detection procedure using a dual control charting system based on extracted MPCA features and residuals, where (a) represents the original Area of Interest (AOI), (b) demonstrates the convoluted AOI, (c) accounts for reduced features, and (d) indicates the dual control chart system.

The rest of the chapter is organized as follows. Section 2 provides a detailed literature review on the existing process signature quantification and modeling techniques as well as online process monitoring using the salient process related features. Section 3 proposes the feature extraction and control charting methodology for *in situ* process monitoring based on thermal image

streams. A case study based on building a Ti-6Al-4V thin wall is illustrated in Section 4 to illustrate the effectiveness of the proposed methodology. Last, Section 5 discusses the conclusions and the potential directions for future research.

4.2 Literature review

We investigate the papers regarding to process sensing systems as well as online process monitoring algorithms used in DED processes. The literature review is divided into two main subsections: (1) process sensing methods using monitoring AM processes and (2) online process monitoring and control algorithms. Subsequently, the contribution of the proposed methodology is summarized.

4.2.1 Process sensing systems

The variation in microstructure of the AM parts is governed by the thermos-physical process, which can be reflected by the melt pool. Since the melt pool is the initiation of the part solidification, its characteristics contain significant information about the process quality and microstructural properties [6, 138]. In the literature, *in situ* sensing systems are commonly used to capture the melt pool information in AM processes. Grasso and Colosimo [3] categorize the sensing systems for process signature (e.g., melt pool, scan path, slice) quantification and monitoring into three main groups: (1) non-contact temperature measurements (i.e., pyrometer and Infra-Red (IR) imaging system) [39, 139-141], (2) imaging in the visible range [142-144], and (3) low-coherence interferometric imaging [145, 146]. Moreover, they propose another categorization that groups sensing systems to co-axial and off-axial systems. In this section, the categorization proposed by Grasso and Colosimo [2] is adopted and the sensing systems have been summarized as follows.

4.2.1.1 Non-contact temperature measurements

There are a number of studies for co-axial sensing during AM processes. For example, Clijsters *et al.* [39] propose an anomaly detection in the selective laser melting (SLM) process using melt pool characteristics such as the size captured via co-axial pyrometer sensing systems. They found that the measured metrics of the melt pool, as process signatures, can be firmly linked to defects in the part such as porosity. In addition, Song and Mazumder [60] propose a predictive control model to control the melt pool temperature. They utilized a control system that contains a dual color pyrometer to monitor the melt pool temperature and a real-time controller with constraints to control the laser power [147]. Moreover, Kruth *et al.* [25, 148] describe the applications of hardware used for online monitoring of thermal driven laser processes. They showed that online monitoring of the radiation emitted from laser spots can be used to evaluate the process quality and detect process anomalies such as degradation, balling, surface roughness, etc. There are also a number of prior studies for off-axis sensing during AM processes. Krauss *et al.* [149] developed a layer-wise monitoring approach to monitor the process stability and the resulting part quality based on the temperature distribution captured via off-axis mounted uncooled thermal detector. Although their presented method is able to detect the defects such as delamination in the latent layers, their detection power for part defects will vanish at some point due to difference in thermal diffusivity. Furthermore, Bi *et al.* [59] use multiple measurement systems (e.g., photodiode, pyrometer, CCD camera) to identify and analyze the infrared (IR) temperature signal irradiated from the melt pool, which can be used for quality control and closed loop control. Another study conducted by Lane *et al.* [144] that monitors the melt pool region of laser powder bed fusion (LPBF) using high speed *in situ* thermographic measurements. The major outcomes of the research by Lane *et al.* are summarized as follow. First, they find that there is a need for

statistical analysis to compare the obtained results from thermography and FE method. Second, they observe variation in the size of the melt pool contours based on the location of the build stripes. Third, they find that temperatures on the edges of the scan lines are lower than the center due to reheating by laser.

However, there are potential risks of some sensing systems. It is possible that the melt pool being imaged using an IR camera is an artifact due to the aspect and focus of the camera. Furthermore, calibrating the IR thermal camera requires defining the material emissivity, which may change at higher temperatures. In this study, a dual-wavelength co-axial pyrometer is used to obtain the temperature field for the melt pool. The use of the pyrometer reduces the risk of motion blur since the pyrometer has a specified exposure time (2.0274 ms) that occurs at a specified acquisition rate. The scan rate of the laser was 12.7 mm/s meaning that during the exposure time the build was moving approximately at 26 μm [3]. Since the melt pool dimensions are a few orders of magnitude larger, the effect of any motion blur will be slight. Moreover, it has been shown in previous studies that two-color pyrometers are accurate to measure melt pool temperature on LENS systems [51, 150]. Craig *et al.* [150] show that pyrometer integrated with LENS MR-7 system can measure the critical deposit parameters including peak temperature and cooling rate.

4.2.1.2 Imaging in the visible range

There are a few studies that use imaging in visible range to monitor the AM processes. For example, Yadroitsev *et al.* [143] developed an approach to investigate the evolution of the microstructure in the biomedical products after performing various heat treatment operations. They employed an online co-axial optical monitoring system with charge-coupled device (CCD) camera to measure the surface thermal distribution and the melt pool size of Ti-6Al-4V alloy. The outcome of their study is that the melt pool width and depth are strongly correlated with the changes in

temperature compared to scanning parameters. Furthermore, Gestel [142] utilized co-axial optical monitoring system to capture the peak and averaged intensity of melt pool as well as melt pool contours. The proposed technique has shown the capability to address some of the challenges associated with calibration of the equipment. Kleszczynski *et al.* [151] utilize CCD camera coupled with tilt and shift lens to improve process stability in laser based manufacturing (LBM). They developed two approaches based on correlation between image analysis and acceleration measurement in the sensing system that succeed in detecting process instabilities, leading to ball formation and accentuating critical layers.

4.2.1.3 Low-coherence interferometric imaging

There are also prior studies using interferometry techniques for sensing AM process signatures. With respect to low coherence interferometry (LCI) sensing systems, Neef *et al.* [146] integrate co-axial LCI sensing system SLM setup to analyze the surface topology and detect deviations as well as anomalies in the part based on melt pool signal characteristics. They found that LCI sensor has the capability of detecting and documenting anomalies during the fabrication for every single layer. Moreover, Kanko *et al.* [145] proposed morphology-based defect detection approach in SLM setup coupled with inline coherent imaging (ICI) system. They discovered that ICI measurements recognize the variation in melt pool signals, which eventually contributes to enhancing track quality and identifying fault signatures.

4.2.2 Online process monitoring and control

Online process monitoring and control topics in AM have been extensively studied in metal-based AM processes (e.g., laser powder bed fusion (LPBF), and direct energy deposition (DED)). There are extensive studies in the literature that concentrate on online process monitoring

and control from *in situ* data collection and feature extraction level [3, 4, 7, 130, 152, 153]. Most of the existing studies presented the effect of process parameters on the process signature. However, the online process monitoring term in statistical analysis refers to the identification of anomalies (out-of-control observations) using robust alarm rules. Only a few papers have developed robust statistical methods for online anomaly detection in AM processes [133, 134, 154].

A study by Krauss *et al.* [155] focused on monitoring the temperature distribution of a single layer and its evolution during the time using off-axial thermography setup at a fixed location. Their proposed monitoring and control algorithm is able to detect the process errors, pores, and other types of irregularities based on the thermal distribution during the process. In addition, Schilp *et al.* [156] proposed FEM-based micro and macro scale modelling for thermographic monitoring. They compared the temperature distribution of experimental data with simulation-based results and adjusted the transient temperature field to enhance part quality based on simulation-based methods. Schilp *et al.* reported that process monitoring in macroscale simulation cannot account for randomness of the defects in the parts, but it can contribute to predicting systematic errors and part deformation. Additionally, they found that microscale simulations are not suitable for complex geometries. However, layer-wise process monitoring/microscale simulation is capable of identifying random defects during the manufacture based on the cool down behavior.

As mentioned in the previous paragraph, most studies emphasize using sensing systems to capture the measurable features of the various processes and link them to process instabilities and anomalies. However, the lack of robust monitoring methods to discover defects during the process is a prevalent drawback for the majority of the existing research. In recent years, using statistical process monitoring techniques to detect defects in an automated manner has garnered much

interest in additive manufacturing due to the availability of solid data collection systems. For example, Grasso *et al.* [134] utilized melt pool captured by high-speed off-axial camera as a quantified measure of the SLM process. The pixel intensity profiles are used to characterize the variability in the image stream, and vectorized PCA is used for dimension reduction. Subsequently, *k*-means clustering method has been utilized to detect and locate the defects automatically. Moreover, Grasso *et al.* [133] developed a methodology that integrates acquired images from off-axial IR sensing system with a data analytics approach to identify the plausible variations from the stable behavior of the hard-to-process material i.e., zinc powder in SLM process. Measurable signatures of the process in their study have been set to be the plume properties. Grasso *et al.* used a few layers as training set for Hoteling's T^2 control chart, which can characterize the dynamic behavior of the process. Authors have developed a new automated approach to identify the region of interest (ROI) for each image as well as statistical monitoring tool. They have shown that their proposed method outperforms other methods regarding to the choice of threshold to separate the ROI from the spatters.

4.2.3 Contributions of the proposed methodology

Melt pool characteristics have not been previously utilized extensively to detect or predict the porosity of AM parts. Recently, Khanzadeh *et al.* [74] developed a state-of-the-art methodology that demonstrates the implementation of two-dimensional (2-D) modeling of the melt pool to detect anomalies in additively manufactured thin walls utilizing melt pool morphological characteristics. Khanzadeh *et al.* [154, 157] further developed a methodology based on unsupervised machine learning to characterize the thermo-physical dynamics of the DED process based on melt pool signals to predict porosity during the build. In their study, they utilized the thermal profile of top surface of the melt pool to predict the porosity. X-ray computed tomography

(CT) is used to experimentally locate porosity within the Ti-6Al-4V thin wall specimen, which is then used to validate the predicted porosity locations based on melt pool analysis. Results showed that the porosity prediction accuracy of the proposed method based on the thermal profile of the melt pool is almost 96%. Another study by Khanzadeh *et al.* [158] investigated the relationship between the melt pool characteristics and the defect occurrence in an as-built additive manufacturing part. They used morphological features of the melt pool (i.e., features extracted via Functional Principal Component Analysis (FPCA)) to propose a real-time porosity detection method. The numerical results showed that using morphological features of the melt pool along with supervised learning techniques render 98.44% detection accuracy. The benefits of the newly proposed feature extraction method against the aforementioned method are represented in Figure 5.2.

The studies by Grasso *et al.* [134] and Khanzadeh *et al.*[158] used Traditional Principal Component Analysis (PCA) and FPCA for tensor objects (i.e., IR images), respectively. Traditional Principal Component Analysis (e.g., PCA, vectorized PCA) uses the vector form of tensor objects (e.g., images, videos, EEG signals) and applies spectral decomposition of a large variance-covariance matrix. Although theoretical properties of vectorized PCA are convenient to understand, applying the vectorized PCA to tensor data is sometimes infeasible, especially when the sample size is small compared to the dimension of the vectorized data [159]. In other words, in small sample size cases, resultant parameters from vectorized PCA (i.e., eigenvectors and eigenvalues) become unreliable and unpredictable. For instance, for a set of $p \times q$ data matrices, vectorized PCA constructs $pq \times pq$ variance-covariance matrix to perform the spectrum decomposition; however, MPCA only requires $p \times p$ and $q \times q$ mode-wise variance-covariance matrices, saving a lot of variation and leading to computation simplicity as shown in Figure 5.2.

Additionally, Grasso *et al.* [133, 134] used information from each layer in a sequential manner that may not capture all types of patterns for process monitoring and anomaly detections. Although data reduction approaches such as traditional PCA and MPCA are suitable to reduce the dimensionality, they may ignore some variation left unexplained by the extracted PCs, hence using the residual will add more accuracy to the anomaly detection approaches.

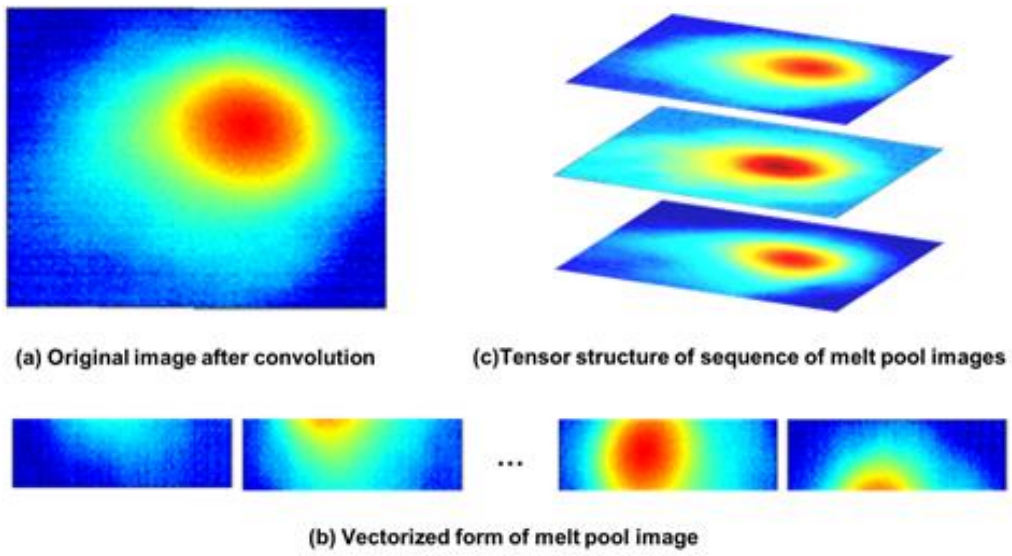

Figure 4.2 Illustrating benefits of MPCA against, where (a) original image size: 130 × 130, (b) N-slice vector structure. PCA covariance is represented by a high-dimensional matrix (130N × 130N), and (c) tensor structure. MPCA covariance is represented by two smaller matrices (130 × 130).

In summary, the technical contributions of this study to the existing literature are as follows:

- We develop a novel data preprocessing and image filtering procedure using convolution to predict the missing values of the temperature measurements for thermal images.

- We utilize MPCA for the data reduction and feature extraction of the thermal images, which are second-order tensors. MPCA can achieve better performance than 2DPCA with reduced computational complexity.
- A dual control charting system is proposed to combine a Hoteling's T^2 chart and a Q chart to simultaneously monitor the extracted low dimensional features and the residual in the tensor which is left unexplained by MPCA, respectively.

This work is significant since the existing approaches for anomaly detection and monitoring mainly rely on *in situ* sensing systems, which are not able to detect the anomalies via robust and automated alarm rules with quantifiable error rates. The anomaly detection method proposed in this study outperforms the unsupervised [157] and supervised learning methods [158] previously used, and it enables us to detect anomalies in an online manner. The proposed anomaly detection method provides high accuracy measurements with appropriate choice of empirical Type I error using cross validation. The proposed methodology is among the handful of studies available in literature that provides a theoretical foundation for qualification and certification of AM products via thermal profile of the melt pool.

4.3 Methodology: In situ monitoring based on thermal image streams

In this section, we propose an MPCA-based online monitoring of defects in the AM parts based on a dual control charting system that consists of Hoteling's T^2 and Q charts. More specifically, we propose a data preprocessing methodology to capture the Area of Interest (AOI) for all the thermal images (tensor structure), and image processing is applied to extract smooth thermal profile of AOI from the captured thermal images. Extracted data points from the high-dimensional structure of the melt pool images are modeled with tensors. Subsequently, low-rank tensor decomposition is employed to extract monitoring statistics for our dual control chart system.

Using tensors for data representation and processing results in a very low computational complexity, whereas most compressed sensing methods such as thermal image sensing systems are usually plagued by high computational complexity [160]. In this study, we formulate a stack of AOIs as a tensor structure. The details of the melt pool thermal image processing are shown below.

Since the proposed method deals with data represented in the forms of scalars, vectors, matrices, and higher-order tensors, we use mathematical notation following the rules below:

- scalars are represented by italic lower-case/uppercase letters ($a, b, \cdots; \alpha, \beta, \cdots, A, B, \ldots$),
- vectors are denoted by bold-face lower-case letters ($\boldsymbol{a}$, $\boldsymbol{b}$, ...) (italic shaped),
- matrices are written as bold-face capitals (**A, B, . . .**), and
- tensors correspond to calligraphic letters ($\mathcal{A}, \mathcal{B}, \ldots$).

4.3.1 Data preprocessing

Each thermal image is represented with a matrix of a columns and b rows, and the values of a and b are determined by the resolution and field of view of the imaging systems. The row and column can be indexed by x and y, respectively, and thus $\mathbf{T}(x, y)$ represents the temperature measurement at the x^{th} row and y^{th} column. The melting temperature t_γ is pre-specified based on the material properties. The elements in the matrix **T** with temperatures greater than t_γ are extracted to define the region of the melt pool surface, i.e., $\mathbf{T} = \{(x, y): \mathbf{T}(x, y) \geq t_\gamma\}$. Applying the aforementioned procedure to the images in thermal history of the fabricated part, all the regions of

the melt pool surfaces can be extracted, denoted by $\mathbf{T}_j$, $j=1, 2, \ldots, k$, where $\mathbf{T}_j$ represents the j^{th} melt pool in the thermal history of the part. We define the Area of Interest (AOI) so that it includes all the $\mathbf{T}_j'$s during the fabrication as shown in Figure 5.3, denoted by $\boldsymbol{\mathcal{A}}_j$, where $\boldsymbol{\mathcal{A}}_j$ is a second-order tensor. More specifically, Figure 5.3 shows the surface of melt pool in AOI domain. We first centralize the thermal images based on the location of their respective peak temperature, denoted by $t_{\max}$, and then extract the AOIs (i.e., the smallest square that contains all the melt pools).

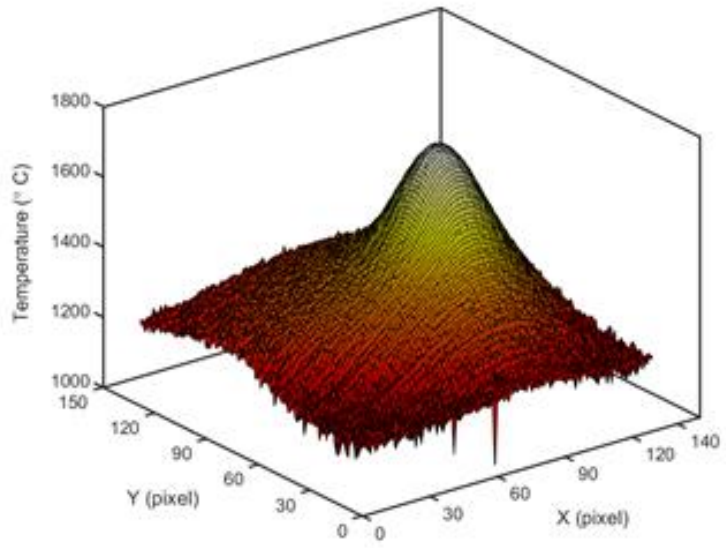

Figure 4.3 3-D representation of the change in temperature for the melt pool as a function of position for the defined Area of Interest, AOI. The AOI is extracted from the thermal image stream from the 2-color pyrometer.

4.3.2 Basic tensor definitions and operators

The collected thermal images within the AOI for each melt pool are represented by $p \times p$ matrices (p is the number of rows/columns for the AOI), $\{\boldsymbol{\mathcal{A}}_j \in \mathbb{R}^{p\times p}\}_{j=1}^{k}$. Conventional techniques such as Principle Component Analysis (PCA) represent each observation $\boldsymbol{\mathcal{A}}_j$ by a long column vector, denoted by $vec\,(\boldsymbol{\mathcal{A}}_j)$, and construct a design matrix $\mathbf{X} = [vec\,(\boldsymbol{\mathcal{A}}_1), \ldots, vec\,(\boldsymbol{\mathcal{A}}_k)]'$,

which results in a $k \times p^2$ matrix. Directly applying data analysis method to the vectorized design matrix $\mathbf{X}$ may lead to the issue of high dimensionality. To resolve this issue, multilinear subspace learning for tensor data has been applied to extract useful information from multidimensional data such as images and videos [161-163]. In this paper, we apply tensor-based methods to make full use of the spatial correlation in the thermal images for feature extraction. To model the obtained AOIs as a tensor and analyze them using tensor-based approaches, the basic notation, definitions, and operators are adopted from multilinear algebra, pattern recognition and adaptive learning literature [137].

Definition 1. Tensor is a generalization of a matrix to higher-order dimensions, referred as ways or modes.

Vectors and matrices can be expressed as special cases of tensors with one and two modes, respectively. An N^{th}-order tensor is denoted by $\boldsymbol{\mathcal{A}} \in \mathbb{R}^{I_1 \times I_2 \times I_3 \times \ldots \times I_N}$ and is described by N indices $i_n, n = 1, 2, \ldots, N$, where each i_n accounts for the n-mode of $\boldsymbol{\mathcal{A}}$.

Definition 2. The n-mode product of a tensor $\boldsymbol{\mathcal{A}}$ by a matrix $\mathbf{U} \in \mathbb{R}^{J_n \times I_n}$, can be expressed as $\boldsymbol{\mathcal{A}} \times_n \mathbf{U}$, which is a tensor by components: $(\boldsymbol{\mathcal{A}} \times_n \mathbf{U})(i_1, \ldots, i_{n-1}, j_n, i_{n+1}, \ldots, i_N) = \sum_{i_n} \boldsymbol{\mathcal{A}}(i_1, \ldots, i_N) \times \mathbf{U}(j_n, i_n)$.

Definition 3. The inner product of two tensors (e.g.,$\boldsymbol{\mathcal{A}}, \boldsymbol{\mathcal{B}} \in \mathbb{R}^{I_1 \times I_2 \times I_3 \times \ldots \times I_N}$) and the Frobenius norm of a tensor can be defined as below:

$$< \boldsymbol{\mathcal{A}}, \boldsymbol{\mathcal{B}} > = \sum_{i_1} \sum_{i_2} \ldots \sum_{i_N} \boldsymbol{\mathcal{A}}(i_1, i_2, \ldots, i_N) \cdot \boldsymbol{\mathcal{B}}(i_1, i_2, \ldots, i_N) \tag{4.1}$$

$$\left|\left|\boldsymbol{\mathcal{A}}\right|\right|_F = \sqrt{< \boldsymbol{\mathcal{A}}, \boldsymbol{\mathcal{A}} >}. \tag{4.2}$$

Definition 4. Unfolding $\boldsymbol{\mathcal{A}}$ using *n*-mode vectors can be expressed as a matrix $\mathbf{A}_{(n)} \in \mathbb{R}^{I_n \times (I_1 \times \cdots \times I_{n-1} \times I_{n+1} \times \cdots \times I_N)}$. For example, Figure 4.4 demonstrates the schematic 1-mode/column mode unfolding of one layer of AOIs, which can be illustrated as third-order tensors. Note that unfolding is an operation that converts a tensor into a matrix.

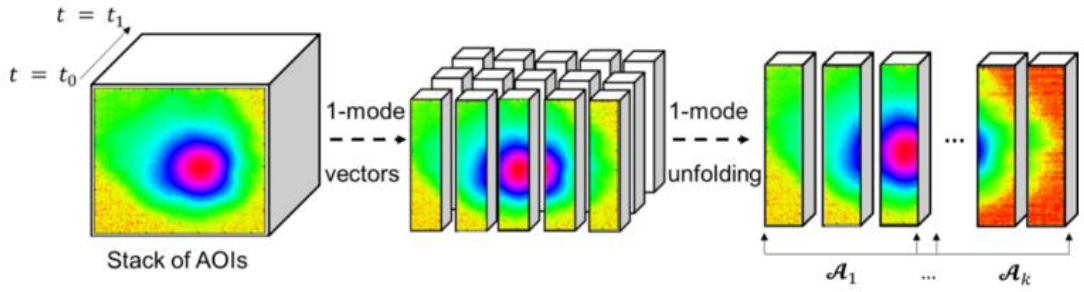

Figure 4.4 Schematic illustration of the 1-mode vectors and 1-mode unfolding of a layer of AOIs.

4.3.3 Low dimensional feature extraction using MPCA

Multilinear Principle Component Analysis (MPCA), introduced by Lu *et al.* [137], is one of the various low-rank decomposition approaches that can be used for dimension reduction and feature extraction for image data. In this study, each of the AOIs is represented as a tensor object, i.e., $\boldsymbol{\mathcal{A}}_j \in \mathbb{R}^{p \times p}$ for $j = 1, \ldots, k$, where *k* is the sample size, and p denotes the number of rows and columns. The main idea of MPCA is to construct a set of orthogonal projection matrices that lead to low-dimensional tensors to represent the majority of the variability in the original tensor.

Let $\{\boldsymbol{\mathcal{A}}_j : j = 1, \cdots, k\}$ be the set of defect-free AOIs extracted from thermal images through the data acquisition and preprocessing procedure. A set of m $(m < k)$ tensors (i.e., AOIs) is randomly selected as the training set. In this study, each tensor object $\boldsymbol{\mathcal{A}}_j \in \mathbb{R}^{p \times p}$ takes values in

two tensor subspaces. The total scatter/variation of these tensors is defined as $\psi_{\boldsymbol{\mathcal{A}}} = \sum_{j=1}^{m} \left|\left|\boldsymbol{\mathcal{A}}_j - \bar{\boldsymbol{\mathcal{A}}}\right|\right|_F^2$ where $\bar{\boldsymbol{\mathcal{A}}} = \frac{1}{m}\sum_{j=1}^{m} \boldsymbol{\mathcal{A}}_j$. The MPCA approach is applied to find a set of multilinear transformation matrices $\{\tilde{\mathbf{U}}^{(n)} \in \mathbb{R}^{p\times p_n}, n = 1,2\}$ that projects the AOIs from the original tensor space $\mathbb{R}^p \otimes \mathbb{R}^p$ onto a lower-dimensional, tensor subspace $\mathbb{R}^{p_1} \otimes \mathbb{R}^{p_2}$ ($\otimes$ denotes Kronecker product) ($p_1 < p$ and $p_2 < p$). The purpose of using MPCA is to determine two mapping matrices that maximizes the total scatter in the tensor subspace, denoted by $\psi_{\boldsymbol{\mathcal{Y}}}$, i.e., $\{\tilde{\mathbf{U}}^{(n)} \in \mathbb{R}^{p\times p_n}, n = 1,2\} = \arg_{\tilde{\mathbf{U}}^{(1)},\tilde{\mathbf{U}}^{(2)}} \max \psi_{\boldsymbol{\mathcal{Y}}}$,where low-dimensional demonstration of tensor objects is denoted by $\boldsymbol{\mathcal{Y}}$.

To obtain the projection matrices for second-order tensor, two optimization sub-problems are required to be solved because second-order tensor subspace consists of two projection matrices to two vector subspaces. The iterative procedure is adopted from [137, 164] to obtain the projection matrices, as illustrated in the algorithm below.

Algorithm. Feature extraction via MPCA

Input. Set of AOIs $\boldsymbol{\mathcal{A}} = \{\boldsymbol{\mathcal{A}}_j \in \mathbb{R}^{p\times p}, j = 1,2,\cdots,m\}$.

Output: Low-dimensional demonstration of training tensor objects $\boldsymbol{\mathcal{Y}} = \{\boldsymbol{\mathcal{Y}}_j \in \mathbb{R}^{p_1\times p_2}, j = 1,2,\cdots,k\}$ while the maximum variation is obtained.

1. **Preprocessing.** Center the input AOIs as $\tilde{\boldsymbol{\mathcal{A}}} = \{\tilde{\boldsymbol{\mathcal{A}}}_j = \boldsymbol{\mathcal{A}}_j - \bar{\boldsymbol{\mathcal{A}}}, j = 1,2,\cdots,k\}$.

2. **Initialization** [Full Projection]. Full Projection Truncation (FPT) is applied to initialize the iterative solution for MPCA.

Compute the spectrum decomposition of $\boldsymbol{\phi}^{(n)^*} = \sum_{j=1}^{m} \widetilde{\mathbf{A}}_{j(n)} \cdot \widetilde{\mathbf{A}}'_{j(n)}$, where $\widetilde{\mathbf{A}}_{j(n)}$ is the n-mode of unfolded matrix of $\boldsymbol{\mathcal{A}}_j$. We initialize $\widetilde{\mathbf{U}}^{(n)}$ as a matrix that comprises the eigenvectors of the p_n most significant eigenvalues ($n = 1, 2$) of $\boldsymbol{\phi}^{(n)^*}$.

3. **Local optimization.**

- Calculate $\{\widetilde{\boldsymbol{\mathcal{Y}}}_j = \widetilde{\boldsymbol{\mathcal{A}}}_j \times_1 \widetilde{\mathbf{U}}^{(1)'} \times_2 \widetilde{\mathbf{U}}^{(2)'}, j = 1,2, \dots, m\}$.
- Initialize total scatter $\psi_{\boldsymbol{y_0}} = \sum_{j=1}^{m} ||\widetilde{\boldsymbol{\mathcal{Y}}}_j||_{\boldsymbol{F}}^{2}$.
- For i = 1 : r (i.e., r is the number of iterations)
  - For n = 1 : 2 (i.e., n is the number of order for original tensor)

    Set the $\widetilde{\mathbf{U}}^{(n)}$ such that contains p_n eigenvectors of the matrix

$$\boldsymbol{\phi}^{(n)} = \sum_{j=1}^{m} (\widetilde{\mathbf{A}}_{j(n)} - \overline{\mathbf{A}}_{(n)}) \cdot \widetilde{\mathbf{U}}^{(n)} \cdot \widetilde{\mathbf{U}}^{(n)'} \cdot (\widetilde{\mathbf{A}}_{j(n)} - \overline{\mathbf{A}}_{(n)})' \text{, where } \overline{\mathbf{A}}_{(n)} = \frac{\sum_{j=1}^{m} \widetilde{\mathbf{A}}_{j(n)}}{m}$$

  - Compute $\{\widetilde{\boldsymbol{\mathcal{Y}}}_j,\ j = 1,2, \dots, m\}$ and $\psi_{\boldsymbol{y_i}}$.

Stopping criterion. If $\psi_{\boldsymbol{y}_i} - \psi_{\boldsymbol{y}_{i-1}} < \theta$, proceed to next step and set $\widetilde{\mathbf{U}}^{(n)^*} = \widetilde{\mathbf{U}}^{(n)}$, which represents the optimized projection matrices. Otherwise, go back to 3. (Note that θ is a pre-specified small number (e.g., $\theta = 10^{-6}$)).

4. **Projection for a new observation**. The tensor low dimensional features as well as residuals using projection can be represented as:

4.1 Calculate low dimensional features: $\{\boldsymbol{\mathcal{Y}}_j = \boldsymbol{\mathcal{A}}_j \times_1 \tilde{\mathbf{U}}^{(1)^{*\prime}} \times_2 \tilde{\mathbf{U}}^{(2)^{*\prime}}, j = 1,2,\dots,m\}$.

4.2 Calculate residuals $\{\boldsymbol{\mathcal{E}}_j = \boldsymbol{\mathcal{A}}_j - \boldsymbol{\mathcal{Y}}_j \times_1 \tilde{\mathbf{U}}^{(1)^{*\prime}} \times_2 \tilde{\mathbf{U}}^{(2)^{*\prime}}, j = 1,2,\dots,m\}$

- Monitoring features. For a new AOI $\boldsymbol{\mathcal{A}}_{new} \in \mathbb{R}^{p \times p}$, the monitoring features and residuals can be obtained by:

$$\boldsymbol{\mathcal{Y}}_{new} = \boldsymbol{\mathcal{A}}_{new} \times_1 \tilde{\mathbf{U}}^{(1)^{*\prime}} \times_2 \tilde{\mathbf{U}}^{(2)^{*\prime}} \rightarrow \boldsymbol{\mu}\text{: vectorized } \boldsymbol{\mathcal{Y}}_{new}.$$

$$\boldsymbol{\mathcal{E}}_{new} = \boldsymbol{\mathcal{A}}_{new} - \boldsymbol{\mathcal{Y}}_{new} \times_1 \tilde{\mathbf{U}}^{(1)^{*\prime}} \times_2 \tilde{\mathbf{U}}^{(2)^{*\prime}} \rightarrow \delta\text{: the Frobenius norm of vectorized } \boldsymbol{\mathcal{E}}_{new}.$$

The number of low-dimensional monitoring features is determined based on the total variation explained by those features. We choose the first t features with maximum scatters such that the cumulative scatter/variation (i.e., ρ) exceeds a specified value. Cumulative proportion of variation can be computed by equation as follows [165]:

$$\rho = \frac{\|\boldsymbol{\mathcal{A}} \times_1 \tilde{\boldsymbol{\Lambda}}^{(1)} \times_2 \tilde{\boldsymbol{\Lambda}}^{(2)}\|_F^2}{\|\boldsymbol{\mathcal{A}}\|_F^2}, \text{ where } \begin{cases} \tilde{\boldsymbol{\Lambda}}^{(1)} = \tilde{\mathbf{U}}^{(1)} (\tilde{\mathbf{U}}^{(1)\prime} \tilde{\mathbf{U}}^{(1)})^{-1} \tilde{\mathbf{U}}^{(1)\prime} \\ \tilde{\boldsymbol{\Lambda}}^{(2)} = \tilde{\mathbf{U}}^{(2)} (\tilde{\mathbf{U}}^{(2)\prime} \tilde{\mathbf{U}}^{(2)})^{-1} \tilde{\mathbf{U}}^{(2)\prime}. \end{cases} \quad (4.3)$$

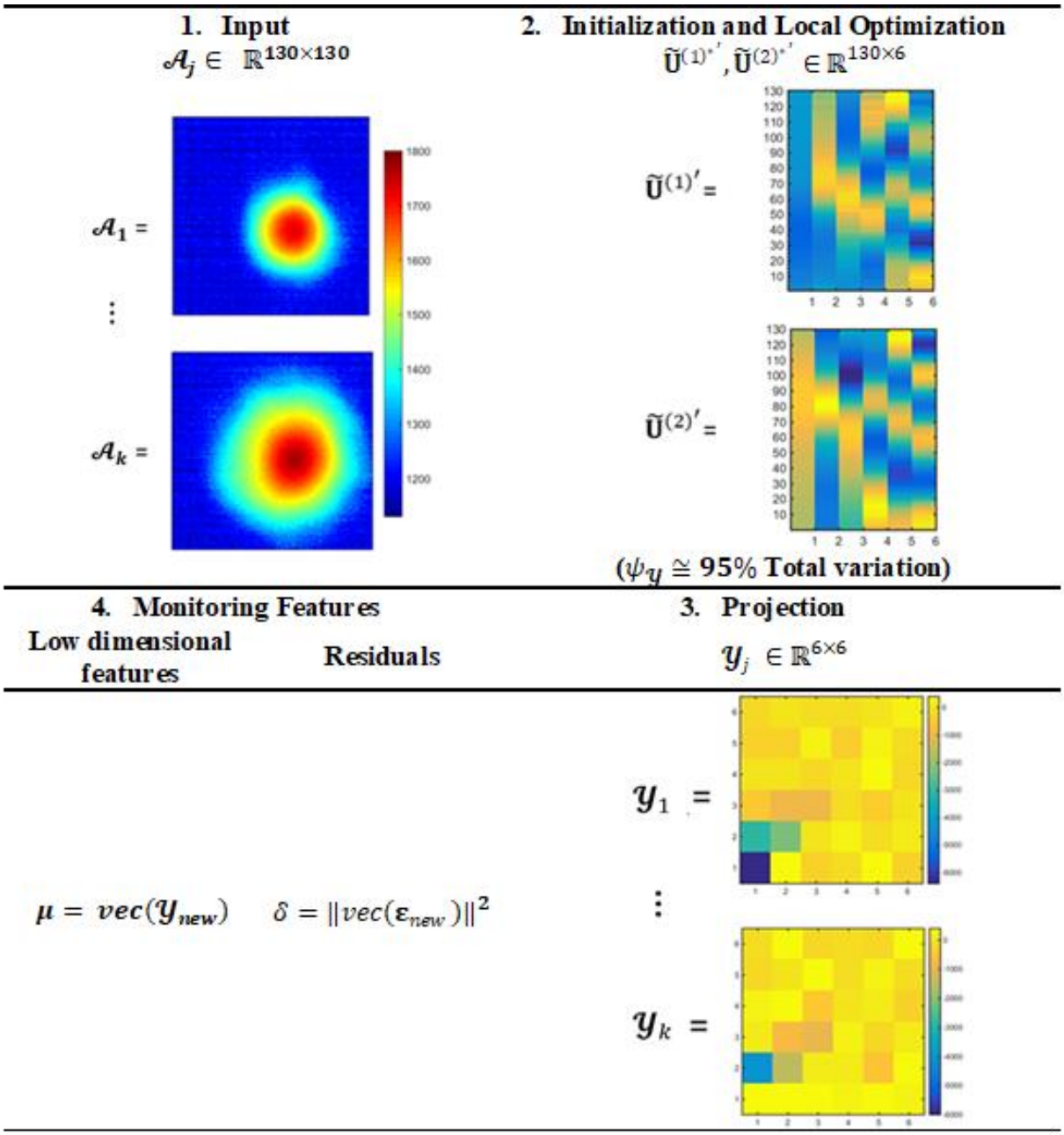

Figure 4.5 Applying the MPCA algorithm to thermal data and extracting monitoring features.

Figure 4.5 demonstrates the process of employing the MPCA algorithm to the captured AOIs. The significance of the procedure is that we can represent a high dimensional image (tensor object) by a low dimensional vector. For example, the dimensionality of AOI originally is 130×130 and using the mentioned algorithm diminishes to 6×6 (i.e., 0.213% of the original dimension).

4.3.4 Statistical process monitoring using dual control charts

After extracting features from high dimensional AOIs, the multivariate control charts (e.g., Hoteling's T^2, multivariate exponentially weighted moving average (MEWMA), etc.) can be performed on the extracted features to detect anomalies during the process. Although features extracted via MPCA embrace most of the information in the AOI, appending the remaining information in residuals could account for information not included in the low-dimensional features so as to improve the performance of the proposed monitoring approach. In this study, we perform low-dimensional feature monitoring as well as residual monitoring: the former is designed to detect any process shift that occurs in the extracted principal components, and the latter is to detect any shift that occurs in the covariance structure of the thermal images We monitor the residuals using a *Q*-chart adopted from [166, 167]. The class labels for each AOI sample are defined as binary variables based on X-ray computed tomography, which takes the value of 1 if the AOI is identified as porosity/out-of-control, and 0 normal (in-control), the samples of in-control and out-of-control AOIs are illustrated in Figure 4.6.

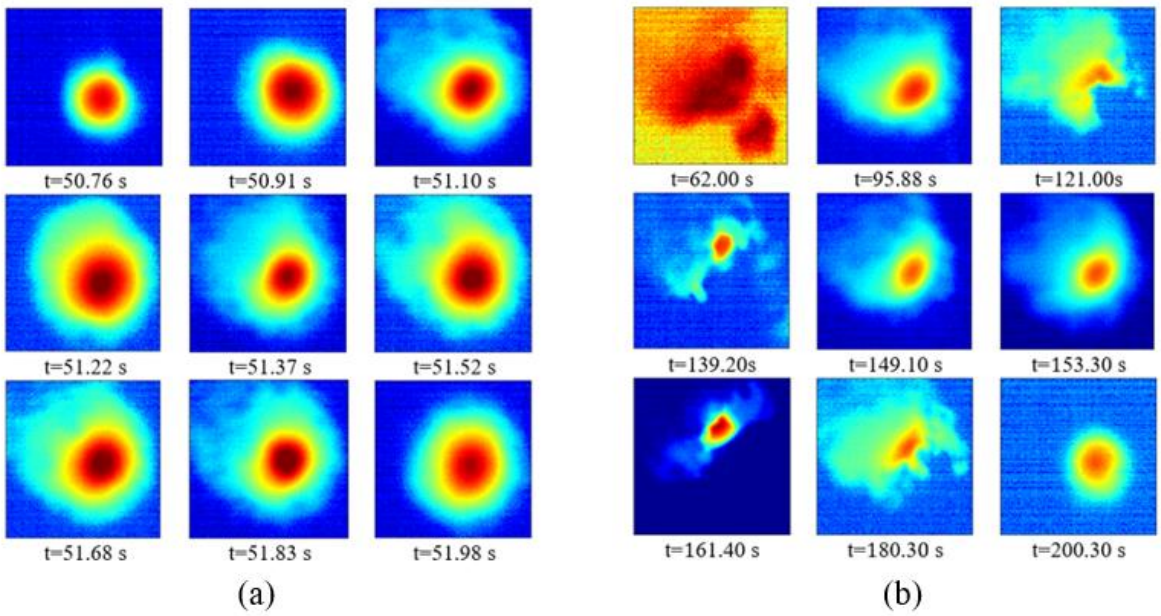

Figure 4.6 Demonstrating AOI samples where (a) in-control AOIs and (b) out-of-control AOIs during the build (unit of the color bar is in℃).

In this section, we concentrate on the Phase II analysis in statistical process monitoring. First, we utilize a sample of m AOIs that are related to normal/in-control thermal images to estimate the parameters of MPCA model, and compute the control limits of Hoteling's T^2 and Q-charts based on pre-specified false alarm rates. For each new thermal image observation, the estimated parameters of MPCA model are applied to its AOI, then the low-dimensional features and residual are extracted. Then, based on the computed monitoring statistics Hoteling's T^2 and Q charts are constructed. As mentioned in Figure 4.6, let $\boldsymbol{\omega_\mu}$ and δ denote the p_1p_2-dimension vector and a positive value, which account for the low-dimensional features and residual for new thermal images, respectively. The Hoteling's T^2 monitoring statistic is computed by:

$$T^2 = \frac{m(m-p_1p_2)(\boldsymbol{\omega_\mu}-\bar{\boldsymbol{\omega}}_{\boldsymbol{\mu}})'\mathbf{S}^{-1}(\boldsymbol{\omega_\mu}-\bar{\boldsymbol{\omega}}_{\boldsymbol{\mu}})}{p_1p_2(m^2-1)} \tag{4.4}$$

where $\bar{\boldsymbol{\omega}}_{\boldsymbol{\mu}}$ and $\mathbf{S}$ are the estimated mean vector and variance-covariance matrix of the low-dimensional features using m in-control samples [168]. Moreover, δ is calculated as the Q-chart monitoring statistics.

If the low-dimensional features and residuals follow normal distributions, $N_{\boldsymbol{\mu}}(\boldsymbol{\omega}_{\boldsymbol{\mu}}, \boldsymbol{\Sigma}_{\boldsymbol{\mu}})$ and $N(\tau, \sigma_{\tau}^2)$, respectively, T^2 will follow an F-distribution with $p_1 p_2$ and $m - p_1 p_2$ degrees of freedom, and the distribution of τ/l will be a Chi-square distribution with f degrees of freedom. The parameters of l and f are estimated by solving the equations obtained from the method of moments [167]: $E(\tau) = lf$ and $var(\tau) = 2l^2 f$. Based on the obtained results from aforementioned statistics, control limits of dual control charts can be estimated with confidence level of $(1 - \alpha)$ for each of the distributions. If the normality condition of the low-dimensional features and residuals is not satisfied, the empirical distribution of statistics can be determined using historical in-control samples. Hence, the $(1 - \alpha)100^{th}$ percentile of the Phase I data can be obtained from empirical distributions to be set as control limits. Note that the confidence level of monitoring low-dimensional features and residuals simultaneously based on dual control charts could be approximated as $(1 - (1 - \alpha)^2)$. The decision rule of the control charting system based on dual control charts is as follows:

1) If either of the two monitoring statistics exceeds their respective control limits, the process is regarded as out of control;

2) Otherwise the process is in control.

4.4 Case study

The case study validates the accuracy of the proposed online process monitoring methodology based on the features extracted from thermal images and dual control charting system. The details and results of the case study are discussed in the following sections.

4.4.1 Experimental setup

OPTOMEC LENS 750 machine equipped with thermal image monitoring system (Figure 4.7 (a)) is used to fabricate a single track Ti-6Al-4V thin wall (Figure 4.7 (b)). Process design parameters used to manufacture the Ti-6Al-4V thin-wall are demonstrated in Table 4.1.A single thin-wall build (length = 47.81mm, height =27.56mm, thickness = 1.78mm) results in 4.7GB of image stream data [70]. Our sample was examined for the presence of any process-induced porosity (at the micron-scale) using a high resolution X-ray computed tomography system (Skyscan 1172) – capable of revealing internal features to a resolution of 1 μm. The sample was mounted vertically on a high-precision stage and incrementally rotated by 0.5° degree for a full 360° rotation. As the sample rotated, X-ray beams were transmitted through the specimen at a voltage of 100 KV and a current of 100 μ. Filtering was done using an Al+Cu filter. Each point in the sample was exposed for 1400 ms with pixel size set of 3 μm. The cross section images of the sample are then reconstructed by a modified Feldkamp cone-beam algorithm to create a complete 3D representation of external and/or internal surfaces, including defects. Further analysis of the acquired CT scans and image reconstruction were performed using the Volume Graphics software package (VGStudioMax and a corresponding free viewer program called myVGL), with a ring artifacts reduction to 8 and beam hardening correction to 70%. Outputs of the X-ray CT characterization were used to manually label the AOIs as normal and abnormal (i.e., in-control and out-of-control) samples. The sample was also inspected using a field emission gun scanning

electron microscopy (FEG SEM, Zeiss SUPRA™ 40) for intra-part defect characterization. The sample was sputter-coated with gold to provide conductive coating that enhances the images under SEM. Outputs of the X-ray CT characterization, containing size, morphology, and location of the detected defects, were used to label the AOIs as normal and abnormal (i.e., in-control and out-of-control) samples. The sample was also inspected using a field emission gun scanning electron microscopy (FEG SEM, Zeiss SUPRA™ 40) for intra-part defect characterization. The sample was sputter-coated with gold to provide conductive coating that enhances the images under SEM.

Table 4.1 LENS process design parameters for AM thin wall.

Power	300 W	Substrate (stainless steel)	3.175 mm
Scan speed	12.7 mm/s	Starting offset from substrate	130.391mm
Powder feed rate	0.06 g/s	Determination of layer thickness	0.508 mm
Determination of hatch spacing	0.508 mm	Nozzle diameter	0.889 mm

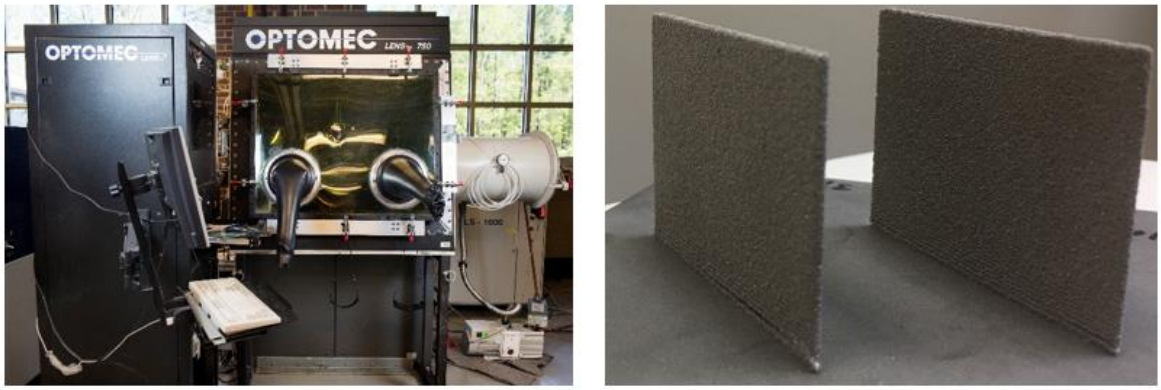

(a) (b)

Figure 4.7 (a) LENS machine used to fabricate the Ti-6Al-4V thin wall and (b) fabricated Ti-6Al-4V thin walls.

Dynamic and time-varying behavior of melt pool is recorded by the built-in thermal imaging system, and then used to develop the statistical process monitoring based on the thermal distribution of the AOIs. The thermal monitoring system is equipped with a dual-wavelength pyrometer (Stratonics, Inc.) and an IR camera (Sierra-Olympic Technologies, Inc. Viento320), which were used to capture thermal profile from the top view and side view of the melt pool during the fabrication (see Figure 4.8). In this study, the thermal images obtained from the pyrometer (Figure 4.8 (a)) are used for AOI extracting and process monitoring. The thermal history observed from the side view, collected from IR camera (Figure 4.8 (b)), is not used in this study. In this study, data recorded from dual-wavelength pyrometer camera is utilized for capturing the melt pool characteristics. Using pyrometer camera maintains some superiorities and features including [70]: (1) the pyrometer sensor reduces the risk of motion blur because of a specified exposure time (2.0274 ms) that occurs at a specified collection rate. (2) the scan rate of the laser is 12.7 mm/s meaning that during the exposure time the build moves approximately at 26 μm [38]. (3) CMOS detector has been used in the pyrometer with array size and pixel pitch being 752×480 and 6.45μm, respectively. (4) the temperature range in the pyrometer varies from 1000-2500℃. (5) Exposure time and pixel clock are set to be 2.0274 ms and 5 MHz, respectively. The nominal image collection rate of the pyrometer is approximately 6.4 Hz (see 8 (b)).

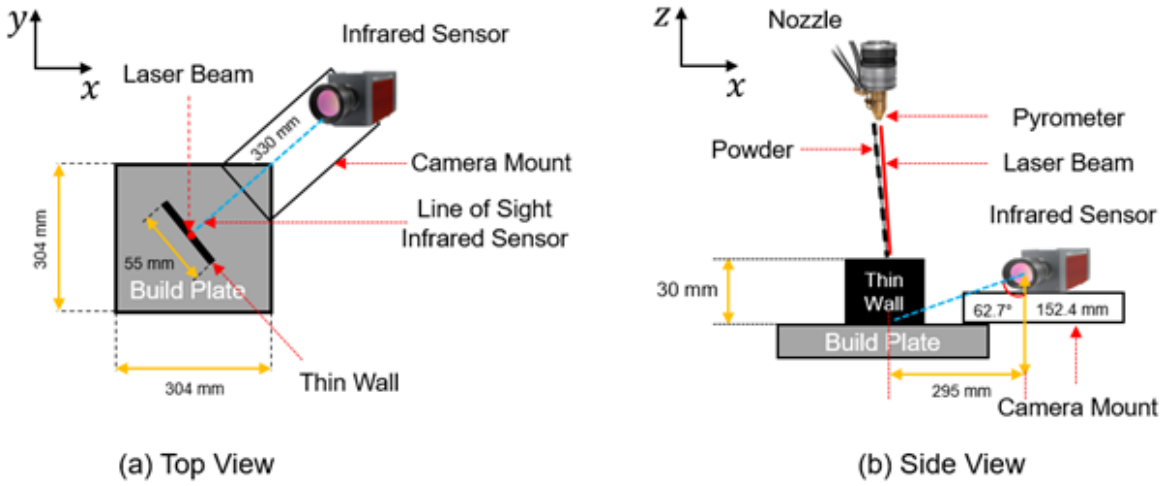

Figure 4.8 Images of (a) top view of IR camera and (b) side view of the pyrometer and their orientation with respect to the substrate and thin wall within the build chamber [70, 157, 158].

4.4.2 Anomaly detection using MPCA-extracted low dimensional features

The number of thermal images captured using co-axial pyrometer camera is $K = 1564$ that each is represented by a 480 × 752 matrix. The area of interest (AOI) for each thermal image is extracted according to the data pre-processing procedure described in section 3.2, which is a 130 × 130 matrix (2^{nd}-order tensor) and embraces the melt pool. As an instance 2D representation for a few of AOI is delineated in Figure 4.9. Although data preprocessing diminished the size of the image from 480 × 752 matrix to 130 × 130 (i.e. ~95.32% decrease), the dimension of data is still fairly high. Hence, MPCA is applied to reduce the size of AOI further. Note that 36% of the in-control data (~560 AOIs) are chosen randomly to estimate the parameters of the low rank tensor decomposition. Subsequently, using the projection matrices obtained from training process of MPCA, the low dimensional features of each image is extracted. Therefore, MPCA converts 130 × 130 tensor to a 25 × 36 matrix, and thus the two operations in total reduce the size of the original

thermal image by the rate of ~99.75%. Additionally, the Frobenius norm of the residual tensor is used to represent the information in each image which is not extracted by MPCA.

Another 36% of the in-control data is utilized for the Phase I analysis of the control charts. Low dimensional features ($\boldsymbol{\mu}$, i.e., column vectors with 25 × 36 components) and norm of the residual (δ) from in-control images are used to calculate upper control limit (UCL) for dual control charts, respectively. At last, the features and residuals from the remaining 28% of the data (~435 AOIs) are plotted on the corresponding control charts to detect the anomalies based on thermal images.

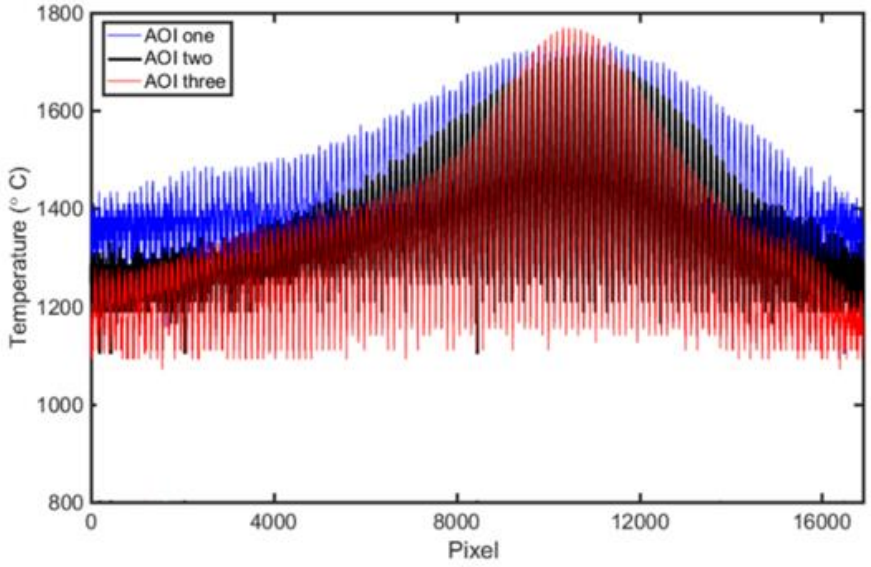

Figure 4.9 Representation of AOI sample in 2D graphs.

Parameter tuning in MPCA and model validation for dual control chart system is performed via cross validation. In particular, the MPCA models and Phase I of process monitoring are trained based on randomly selected subset of in-control samples (i.e., 36% for each with no

overlap) and tested based on the remaining set, which is 28% of the thermal images. Note that in tensor decomposition using MPCA, the percentage of the variation kept in each mode is tuned to obtain better performance, and the best performance is observed using 93.5% of variation in each mode. Moreover, the maximum number of iterations in MPCA is another parameter required to be tuned, which is directly linked to computational time. In this study taking into account the computational time, 20 iterations are found to be reasonable.

The above-mentioned procedure is repeated for multiple times to ensure that each in-control AOI is selected for both training and testing set. Moreover, various empirical estimates of $(1-\alpha)100$ % of monitoring features and residuals are calculated as the control limits of the dual control charts, respectively. Note that during the randomization and training process, outliers from in-control samples have been detected and eliminated to update the control limits. Finally, in each iteration the out-of-control (abnormal AOI) and in-control (normal AOI) samples from testing set are plotted on T^2 and Q charts, as shown in Figure 4.10. Subsequently, the confusion matrix is constructed to calculate the measures that are required to evaluate the accuracy of the proposed in-process monitoring method. The components of the confusion matrix are TP, FN, FP, and TN which denote the number of true positive, false negative, false positive, and true negative, respectively. If the out-of-control samples detected by control charts are actually anomalies, it will be denoted by TP (such as data point A in Figure 4.10). On the contrary, if an anomaly is not detected, it is expressed by FN (such as data point B in Figure 4.10). If the normal AOIs are incorrectly detected as out-of-control, it is labeled as FP (such as data point C in Figure 4.10). Lastly, if normal AOIs are labeled as in-control samples, it is denoted as TN (such as data point D in Figure 4.10). Furthermore, precision, recall, and F_{Score} account for the accuracy of each process monitoring trial. Using the defined values, the evaluation measures are calculated as follows:

$$\text{Accuracy} = \frac{\text{TP+TN}}{\text{TP+TN+FP+FN}} \qquad \text{Recall} = \frac{\text{TP}}{\text{TP+FN}}$$

$$\text{Precision} = \frac{\text{TP}}{\text{TP+FP}} \qquad \text{F}_{\text{Score}} = \frac{2\times\text{Recall}\times\text{Precison}}{\text{Recall +Precision}}$$

The components of confusion matrix and accuracy evaluation measures for one iteration example are summarized in Table 4.2, which corroborates the accuracy of process monitoring using T^2 charts, Q charts, and dual control charts. In terms of confusion matrix for simultaneous monitoring, the information from both charts is incorporated to improve the accuracy of anomaly detection. For example, the thermal image with respect to data point B in Figure 4.10 corresponds to an anomaly in the process, and in the T^2 chart it is regarded as an in-control AOI incorrectly. However, data point B in the Q chart exceeds the control limit, and combining these dual control charts will result in recognizing B as an out-of-control AOI. The results show that monitoring residuals and low dimensional features simultaneously renders slightly higher rate of accuracy compared to monitoring each of them individually. For instance, using dual control charts contributes to detect one more anomaly compared to applying only T^2chart.

Table 4.2 Constructing the confusion matrix for process monitoring using $T^2$and Q chart.

Monitoring method	**TP**	**TN**	**FP**	**FN**	**Accuracy**	**Recall**	**Precision**	**F_{Score}**	**α**
T^2 chart	60	332	37	3	90.74	95.24	61.86	0.750	0.0199
Q chart	16	365	4	47	88.19	25.40	80.00	0.386	0.0199
Dual control charts	61	332	37	2	90.97	96.83	62.24	0.759	0.0199
Total number of AOIs in testing set							432		
Total number of abnormal AOIs in testing set							63		

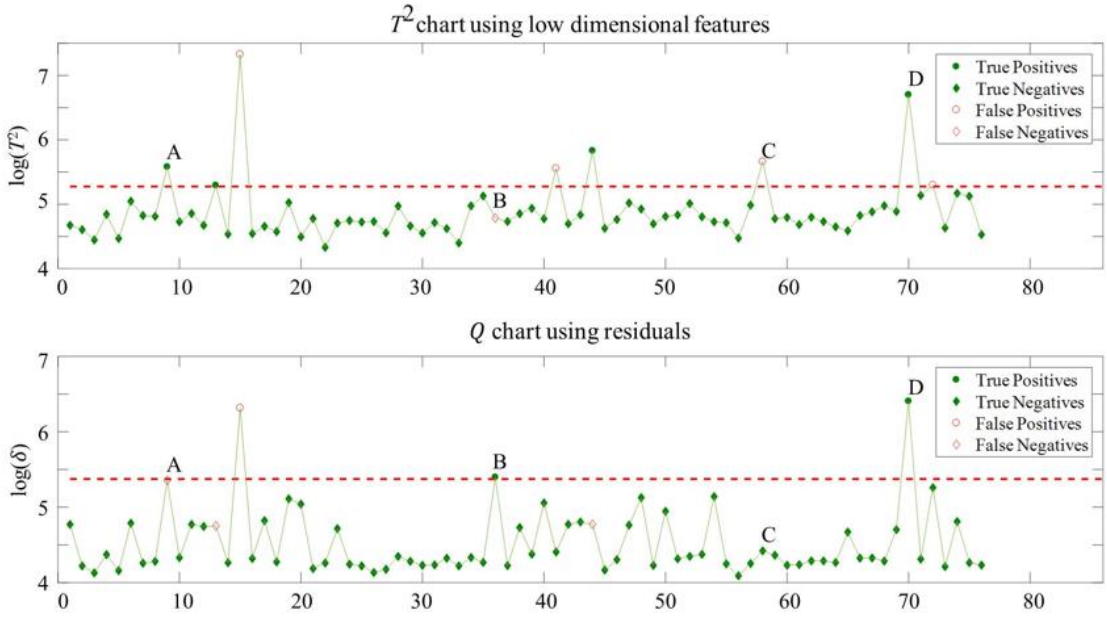

Figure 4.10 An illustration of the proposed dual control chart system, where data points A, B, C, and D in T^2 chart are detected as TP, FN, FP, and TP, respectively. Moreover, FP, TP, TN, and TP are expressed by the same sequence of data points in Q chart. Note that x-axis expresses the index for thermal images in the testing set.

4.4.3 Model selection

Leveraging the tuning parameters of MPCA and calculating the control limits for T^2chart or Q chart by choosing the various empirical Type I error rates, the above-mentioned procedure for process monitoring is repeated for 800 experiments, and the distributions of accuracy measures for multiple Type I error rates are reported in the boxplots in Figure 4.11- Figure 4.14. The results show that the accuracy of anomaly detection slightly increases by decreasing empirical α from 0.055 to 0.005, as demonstrated in Figure 4.11. In addition, comparing the accuracy of anomaly detection using both charts with only using T^2chart indicates the predominance of using T^2 and Q charts simultaneously. Moreover, as presented in Figure 4.12, decreasing empirical α from 0.055 to 0.005 increases the recall for detection approach. In general, using both low dimensional

features and residuals results in greater recall than only using low dimensional features. The trend for precision of the process monitoring method follows the same trend as its accuracy, and using both low dimensional features and residuals outperforms using only low dimensional features (see Figure 4.13). Furthermore, the F_{Score} boxplot for low dimensional features shows increasing trend up to $\alpha = 0.015$, but it decreases at the close. However, the F_{Score} boxplot for low dimensional features and residuals moves in increasing direction, as illustrated in Figure 4.14. Therefore, $\alpha = 0.020$ is an appropriate choice for the proposed process monitoring method due to high true positive rate or recall in either simultaneous monitoring or low dimensional feature monitoring.

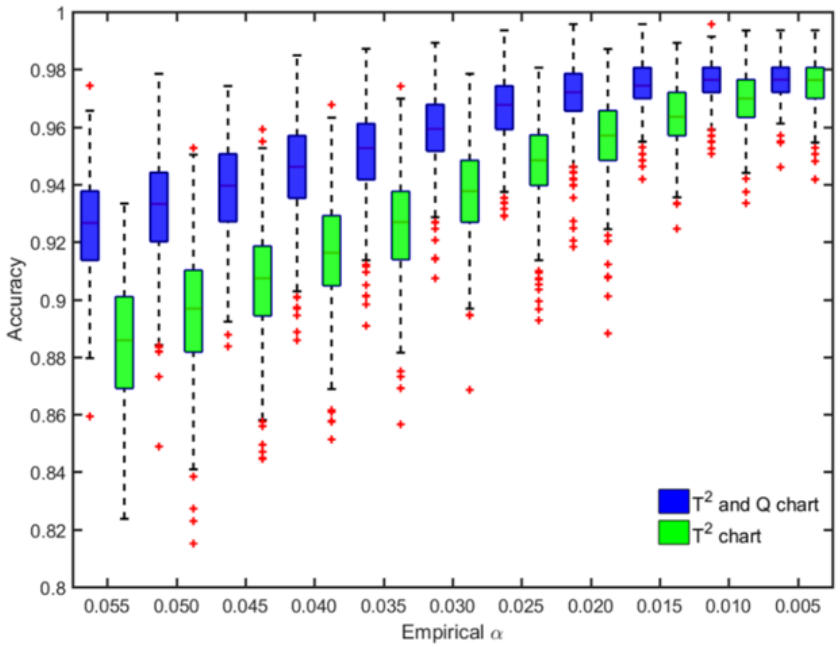

Figure 4.11 Comparing the accuracy for process monitoring method using T^2chart and dual control charts in anomaly detection, where the green box plot indicates the accuracy for T^2chart and the blue one accounts for dual control chart.

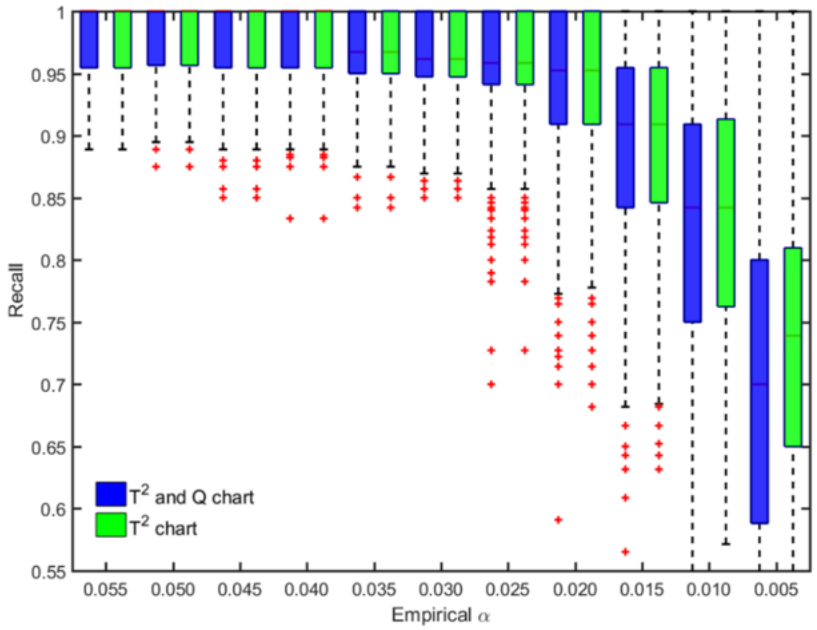

Figure 4.12 Comparing the recall for process monitoring method using T^2chart and dual control charts in anomaly detection, where the green box plot indicates the recall for T^2chart and the blue one accounts for dual control chart.

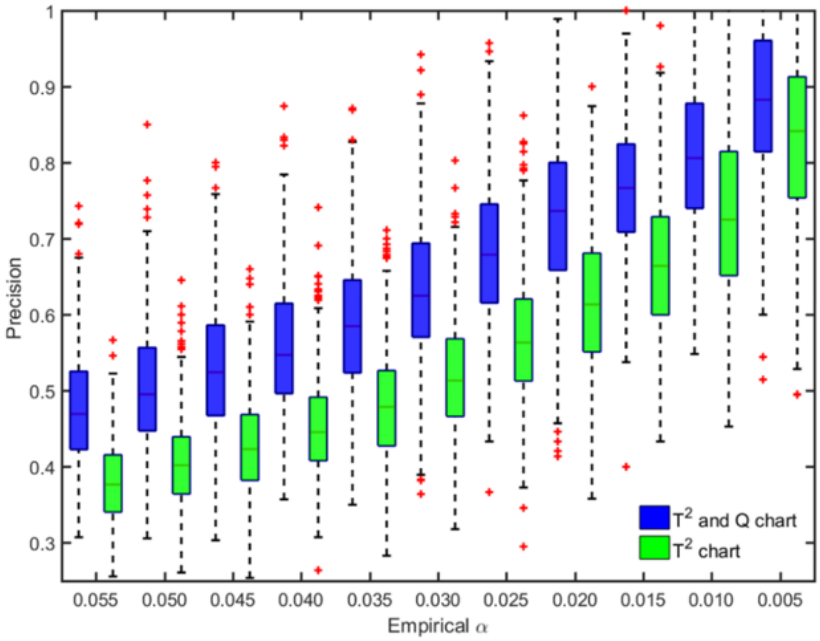

Figure 4.13 Comparing the precision for process monitoring method using T^2chart and dual control charts in anomaly detection, where the green box plot indicates the precision for T^2chart and the blue one accounts for dual control chart.

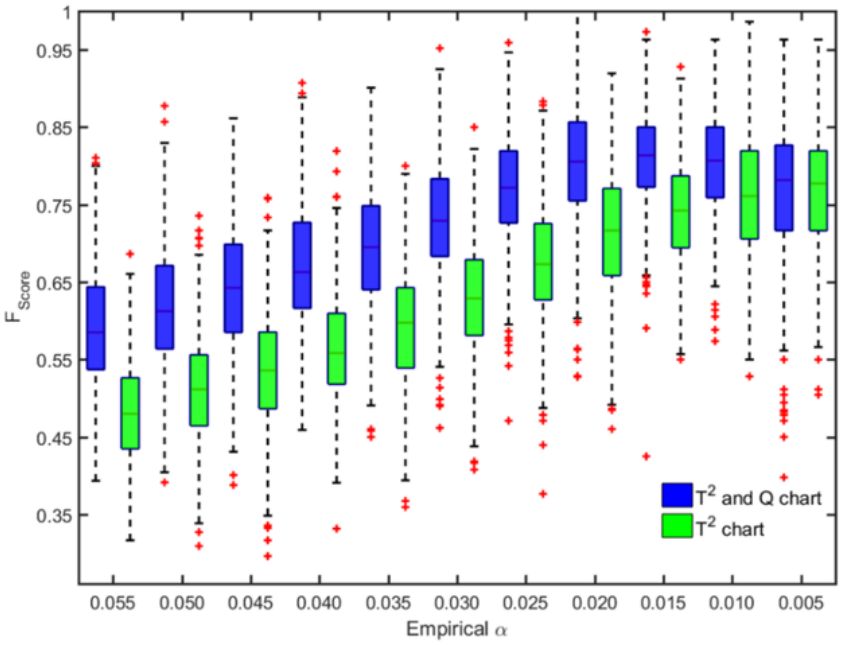

Figure 4.14 Comparing the F_{Score} for process monitoring method using T^2chart and dual control charts in anomaly detection, where the green box plot indicates the F_{Score} for T^2chart and the blue one accounts for dual control chart.

4.5 Summary and conclusion

The occurrence of defects such as porosity and mini-cracks is a paramount issue in AM processes, which leads to compromised performance of the final parts. This study proposes an anomaly detection scheme via statistical process monitoring of low dimensional features as well as residuals extracted from thermal image streams.

Most of the existing studies focus on using sensing systems to capture the measurable features of the different processes and relate them to defects in the part. Our study proposes a robust online process monitoring approach to detect the anomalies in real time, which is a significant improvement in AM process that enables us to perform potential process adjustment action during the build. Major findings of this study and future avenues are summarized below:

1. In the developed scheme, thermal image streams are first preprocessed to extract area of interest (AOI). Since MPCA maintains the natural tensor data structure and parsimonious usage of parameters in selecting the principal component subspaces, a novel MPCA-based feature extraction procedure is proposed which converts high-dimensional AOI streams to low dimensional vectors and single values (residuals). This diminishes the effect of high dimensionality in data. Finally, dual control charts (i.e., $T^2$and Q charts) are developed for *real-time* anomaly detection.

2. Although T^2 monitoring chart based on features extracted via MPCA is able to detect majority of the anomalies, appending the remaining information in residuals by using the *Q* chart can account for information not included in the low-dimensional features so as to improve the performance of the proposed monitoring approach.

3. Performance of the discussed anomaly detection method is assessed for both T^2chart and dual control charts ($T^2$and Q). The results show that using dual control charts improves the accuracy of the anomaly detection. Furthermore, cross validation for empirical α as well as training and testing sets for plotting the control charts is conducted to compare the performance of control charts by leveraging the extracted features. Numerical experiments show that control charts with $\alpha = 0.02$ vastly outperform the other values based on the measures in confusion matrices.
4. The proposed methodology can be applied for other AM processes that share analogous energy-material interactions. Moreover, the anomaly detection procedure can be applied for parts fabricated with various process conditions and complex geometries. Anomaly

characteristics are important signatures for developing process feedback and control systems.

5. The proposed methodology provides avenue for incorporating machine learning techniques with monitoring and sensing systems to distinguish types of anomalies and perform correction actions accordingly.

CHAPTER V

FAST PREDICTION OF THERMAL HISTORY FOR DIRECT LASER DEPOSITION PROCESSES USING NETWORK-BASED TENSOR REGRESSION

5.1 Introduction

Additive manufacturing (AM) has been recognized as thoroughgoing method in the manufacturing industry. In recent decades, most of the developments in AM target the non-structural applications. However, one of the issues that prevents wider approbation of AM technology is deficiency in understanding of its process-structure-property relationships [3]. Hence, several numerical and simulation-based models have been proposed to tackle with dependency of the microstructure properties of part on heuristic iteration. Thermal behavior during melting it is regarded as one of the most informative thermo-physical dynamics of AM process as the temperature history can subsequently be utilized as input to predict microstructural properties of the part. Compared to conventional processes, alloys used in AM processes cause a complex thermal history including directional heat extraction, and repeated melting and rapid solidification [169], which lead to complexity and uncertainty in thermal history prediction and characterization of AM processes. Hence, there is a need for development of validated models to accurately predict the structure and properties of the fabricated materials.

Our objective is to develop a tensor-network design for efficient thermal history prediction of AM processes in a layer-wise manner using thermal image streams, which can subsequently be used to characterize the microstructure and mechanical properties of the AM parts. Since the melt

pools of the previously deposited layers can possibly experience different thermal history (e.g., rapidly heating, melting, cooling, and partial re-melting), the local and global microstructural evolution and mechanical properties of the next layer/layers can be directly related to the previous layer/layers' thermal history [170]. Therefore, it is essential to investigate the in-situ thermal behavior of deposited layers to obtain the desired microstructural and excellent mechanical properties. In this study, the papers pertaining to the common paths for thermal prediction of metal-based AM processes are divided into two main groups: (1) simulation and physics-based models (2) data-driven models. In general, lack of understanding and control over the physical mechanisms in metal additive manufacturing (AM) leads to high degrees of inconsistency in the properties/performance of the manufactured parts [171]. Understanding the AM processes can be attained through modeling and simulation methods. However, most of the existing physics-based models are not able to provide comprehensive understanding of AM processes because they are (1) limited to small sample size, (2) computationally inefficient and inaccurate in predicting process outputs, which are important in in-process control and optimization, (3) incompatible with experimental results because of underlying assumptions or insufficient physics, and (4) not taking into account the uncertainty related to time-series features during the build, which impacts the thermal history and evolution of the microstructure in AM processes [172]. Another stream of research have been utilized for thermal history prediction of AM processes is data-driven approaches. The need for seamless integration of in-process sensing and data-driven approaches to track the dynamic of the process and mitigate the poor repeatability and reliability in AM has been explicitly stated in roadmap reports published in the last 5 years by various US agencies, such as NIST and DoD [173]. Although in-process sensors are increasingly integrated into commercial systems, there is a persistent gap in analytical approaches to synthesize this data and extract

patterns that correlate with specific process conditions or build status [174]. Data-driven approaches have the capability to devise features and train tools learn from examples. However, they demand considerable amount of data to generate results are circumspect. To address those challenges, we propose a tensor-on-tensor regression to establish a relationship between two consecutive layers' thermal history using a generalized multilinear regression method, termed the higher order partial least squares (HOPLS).The proposed method can be regarded as a process-guided data-driven method, which combines both process design information and sensing capability. In this study, the thermal image stream is used to develop a thermal history prediction methodology of AM processes in a layer-wise manner because it is referred as one of the most explanatory lineaments of microstructural evolution and thermo-physical dynamics in directed laser deposition (DLD) processes [16].

The rest of the paper is organized as follows. Section 2 proposes a layer-wise scheme for thermal history prediction of freeform shapes using network-tensor flow. A case study based on building a Ti-6Al-4V double-track thin-wall is illustrated in Section 3 to illustrate the effectiveness of the proposed prediction methodology. Last, Section 4 discusses the conclusions and the potential directions for future research.

5.2 Methodology: Layer-track scheme for thermal history prediction of freeform shapes using network-tensor flow

In this section, we develop tensor-variate regression model to predict the thermal history of each layer based on the thermal history of preceding layer. Higher-order tensors (multiway arrays) are denoted by calligraphic letters, matrices (two-way arrays) are written as bold-face capitals and vectors as boldface lower case letters. Also, Scalars are denoted by italic lower-case/uppercase letters.

5.2.1 Data preprocessing and network-tensor structure modeling

Thermal images obtained using thermal image monitoring system contains a columns and b rows, where a and b are the indicator of resolution and field of view for the imaging system. Temperature measurement at x^{th} row and y^{th} column is represented by $\mathbf{T}(x, y)$, where x and y are the indices for row and column, respectively. Based on the material properties, the melting temperature is defined to be t_γ. To specify the thermal profile of melt pool, the elements of matrix $\mathbf{T}$ greater than t_γ, are chosen, i.e., $\mathbf{T} = \{ (x, y)\colon \mathbf{T}(x, y) \geq t_\gamma \}$. By applying the aforesaid procedure to the images in the thermal history of the part, thermal profile of all melt pools for each layer and track can be extracted, denoted by $\mathbf{T}_{ijk}, \begin{cases} i = 1,2, \dots, l \\ j = 1,2, \dots, t \\ k = 1,2, \dots, n \end{cases}$, where $\mathbf{T}_{ijk}$ expresses the k^{th} melt pool image at i^{th} layer and j^{th} track at thermal history of the part (see Figure 5.1. AOI is defined as the smallest square so that it contains all the $\mathbf{T}_{ijk}$'s in the thermal history, which denoted by $\boldsymbol{\mathcal{A}}_{ijk}$. Note that $\boldsymbol{\mathcal{A}}_{ijk}$ is a second-order tensor, i.e., $\boldsymbol{\mathcal{A}}_{ijk} \in \mathbb{R}^{c \times c}$, where $c \times c$ is the dimension of the defined AOI. As shown in Figure 5.1 (b), $\boldsymbol{\mathcal{A}}_{ijk}$s are assembled to construct a node in network-tensor structure. More specifically according to Figure 5.1 (a), each node in the network structure is stack of second-order tensors, which means each node is a third-order tensor, denoted by $\boldsymbol{\mathcal{N}}_{ij} \in \mathbb{R}^{c \times c \times n}, \boldsymbol{\mathcal{N}}_{ij} = [\boldsymbol{\mathcal{A}}_{ij1} \vdots \boldsymbol{\mathcal{A}}_{ij2} \vdots \cdots \vdots \boldsymbol{\mathcal{A}}_{ijn}]$. To represent a freeform shape with accessible thermal images in a network-tensor structure, transitions between layers and tracks can be illustrated as shown in Figure 5.1 (b), which describes the design and fabrication procedure of the AM part. In other words, each layer have been printed in consecutive tracks, and subsequently next layer have been built upon the previous layer in the same fashion. Hence, there is a link among consecutive tracks and layers as shown in Figure 5.1 (b). Solving the input and output flow equations in such structure of network is a challenging burden and leads to various issues including

problem complexity, computational cost, lack of prediction accuracy, etc. Therefore, in this study we propose a layer-wise transition model by clustering the tracks in each layer, as shown in Figure 5.1 (c). Note that transforming track and layer transition model to only layer transition model not only will diminish the computational cost, but also will provide an opportunity to develop an efficient prediction model. For that reason, nodes of tracks in each layer in Figure 5.1 (b) are assembled to construct a single node, which is a fourth-order tensor, denoted by $\boldsymbol{\mathcal{X}}^{(i)} \in \mathbb{R}^{c\times c\times n\times t}, \boldsymbol{\mathcal{X}}^{(i)} = [\boldsymbol{\mathcal{N}}_{i1} \vdots \boldsymbol{\mathcal{N}}_{i2} \vdots \cdots \vdots \boldsymbol{\mathcal{N}}_{it}]$. As a result, the freeform shape in can be represented in layer-tensor structure. This model enables us to capture the changeover the layers, and also allows us to create a thermal history prediction model in a layer-wise manner, which eventually can be applied to predict the thermal profile of a specific location in the part. Statistical representation of the aforementioned model is a tensor-on-tensor regression. To estimate the parameters of tensor-on-tensor regression, higher-order partial least squares (HOPLS), introduced by Zhao *et al.* [175] is applied.

5.2.2 Parameter estimation for thermal history prediction model using higher-order partial least squares

In this study, HOPLS performs a sequential set of joint Tucker decomposition on pairs of $\boldsymbol{\mathcal{X}}^{(i-1)}$ and $\boldsymbol{\mathcal{X}}^{(i)}$, where the extracted latent variables are required to apprehend the maximum covariance between pairs of $\boldsymbol{\mathcal{X}}^{(i-1)}$ and $\boldsymbol{\mathcal{X}}^{(i)}$.

Algorithm. Layer-wise Thermal History Prediction of Freeform Shapes via HOPLS.

Input. A random set of tensor pairs i.e., $\boldsymbol{M}$ from $\boldsymbol{S} = \left\{\left(\boldsymbol{\mathcal{X}}^{(i-1)}, \boldsymbol{\mathcal{X}}^{(i)}\right)\right\}_{i=2}^{l}$, where l is the number of layers for freeform shape, $\boldsymbol{M} \subseteq \mathbf{S}, n(\boldsymbol{M}) = d$, and $d \leq l$.

Output. A Thermal History Prediction Model i.e., $\widehat{\boldsymbol{\mathcal{X}}}^{(i)} = \widehat{\boldsymbol{\beta}}\boldsymbol{\mathcal{X}}^{(i-1)}$.

Step1. Tucker Decomposition. We denote the selected random set by $\boldsymbol{M} = (\boldsymbol{\mathcal{V}}\ \boldsymbol{\mathcal{W}})$, where $\boldsymbol{\mathcal{V}}$ and $\boldsymbol{\mathcal{W}}$ are fifth-order tensors i.e., $\boldsymbol{\mathcal{V}}, \boldsymbol{\mathcal{W}} \in \mathbb{R}^{d\times c\times c\times n\times t}$. HOPLS decomposes $\boldsymbol{\mathcal{V}}$ and $\boldsymbol{\mathcal{W}}$ into a sum of *rank*-$(1, H_1, H_2, H_3, H_4)$ and *rank*-$(1, K_1, K_2, K_3, K_4)$ Tucker blocks, respectively. The rearranged model of each tensor using Tucker decomposition is shown as follows:

$$\boldsymbol{\mathcal{V}} = \sum_{\mathrm{r}=1}^{\mathrm{R}} \boldsymbol{\mathcal{G}}_{\mathrm{r}}^{\boldsymbol{\mathcal{V}}} \times_1 \mathbf{t}_{\mathrm{r}} \times_2 \mathbf{P}_{\mathrm{r}}^{(1)} \times_3 \mathbf{P}_{\mathrm{r}}^{(2)} \times_4 \mathbf{P}_{\mathrm{r}}^{(3)} \times_5 \mathbf{P}_{\mathrm{r}}^{(4)} + \epsilon_{\boldsymbol{\mathcal{V}}} \tag{5.1}$$

$$\boldsymbol{\mathcal{W}} = \sum_{\mathrm{r}=1}^{\mathrm{R}} \boldsymbol{\mathcal{G}}_{\mathrm{r}}^{\boldsymbol{\mathcal{W}}} \times_1 \mathbf{t}_{\mathrm{r}} \times_2 \mathbf{Q}_{\mathrm{r}}^{(1)} \times_3 \mathbf{Q}_{\mathrm{r}}^{(2)} \times_4 \mathbf{Q}_{\mathrm{r}}^{(3)} \times_5 \mathbf{Q}_{\mathrm{r}}^{(4)} + \epsilon_{\boldsymbol{\mathcal{W}}} \tag{5.2}$$

where R and $\mathrm{t}_{\mathrm{r}} \in \mathbb{R}^d$ are presenting the number of latent vectors and corresponding rth latent column vector. In addition, rth core tensors for $\boldsymbol{\mathcal{V}}$ and $\boldsymbol{\mathcal{W}}$ are demonstrated by $\boldsymbol{\mathcal{G}}_{\mathrm{r}}^{\boldsymbol{\mathcal{V}}} \in \mathbb{R}^{1\times H_1\times H_2\times H_3\times H_4}$ and $\boldsymbol{\mathcal{G}}_{\mathrm{r}}^{\boldsymbol{\mathcal{W}}} \in \mathbb{R}^{1\times K_1\times K_2\times K_3\times K_4}$. $\left\{\mathbf{P}_{\mathrm{r}}^{(\mathrm{j})} \in \mathbb{R}^{c\times H_{\mathrm{j}}}\right\}_{\mathrm{j}=1}^{4}$ and $\left\{\mathbf{Q}_{\mathrm{r}}^{(\mathrm{j})} \in \mathbb{R}^{c\times K_{\mathrm{j}}}\right\}_{\mathrm{j}=1}^{4}$ are the rth projection matrices for corresponding rth latent column vector. Hence, the above-mentioned formula can be represented in a succinct format written as follows:

$$\boldsymbol{\mathcal{V}} = \boldsymbol{\mathcal{G}}^{\boldsymbol{\mathcal{V}}} \times_1 \mathbf{T} \times_2 \mathbf{P}^{(1)} \times_3 \mathbf{P}^{(2)} \times_4 \mathbf{P}^{(3)} \times_5 \mathbf{P}^{(4)} + \epsilon_{\boldsymbol{\mathcal{V}}} \tag{5.3}$$

$$\boldsymbol{\mathcal{W}} = \boldsymbol{\mathcal{G}}^{\boldsymbol{\mathcal{W}}} \times_1 \mathbf{T} \times_2 \mathbf{Q}^{(1)} \times_3 \mathbf{Q}^{(2)} \times_4 \mathbf{Q}^{(3)} \times_5 \mathbf{Q}^{(4)} + \epsilon_{\boldsymbol{\mathcal{W}}} \tag{5.4}$$

where $\mathbf{T} = [\mathbf{t}_1, \mathbf{t}_2, \dots, \mathbf{t}_{\mathrm{R}}]$ denotes the latent matrix constructed by concatenating latent column vectors. Similarly, $\mathbf{P}^{(\mathrm{j})} = \left[\mathbf{P}_1^{(\mathrm{j})}, \mathbf{P}_2^{(\mathrm{j})}, \dots, \mathbf{P}_{\mathrm{R}}^{(\mathrm{j})}\right]$ and $\mathbf{Q}^{(\mathrm{j})} = \left[\mathbf{Q}_1^{(\mathrm{j})}, \mathbf{Q}_2^{(\mathrm{j})}, \dots, \mathbf{Q}_{\mathrm{R}}^{(\mathrm{j})}\right]$ $\forall\, \mathrm{j} = 1,2,3,4$ are obtained by concatenating projection matrices, which are called loading matrices. Moreover, super block diagonal structure of core tensors are shown as $\boldsymbol{\mathcal{G}}^{\boldsymbol{\mathcal{V}}} = diag(\boldsymbol{\mathcal{G}}_1^{\boldsymbol{\mathcal{V}}}, \boldsymbol{\mathcal{G}}_2^{\boldsymbol{\mathcal{V}}}, \dots, \boldsymbol{\mathcal{G}}_{\mathrm{R}}^{\boldsymbol{\mathcal{V}}}) \in \mathbb{R}^{R\times RH_1\times RH_2\times RH_3\times RH_4}$ and $\boldsymbol{\mathcal{G}}^{\boldsymbol{\mathcal{W}}} = diag(\boldsymbol{\mathcal{G}}_1^{\boldsymbol{\mathcal{W}}}, \boldsymbol{\mathcal{G}}_2^{\boldsymbol{\mathcal{W}}}, \dots, \boldsymbol{\mathcal{G}}_{\mathrm{R}}^{\boldsymbol{\mathcal{W}}}) \in \mathbb{R}^{R\times RK_1\times RK_2\times RK_3\times RK_4}$. Furthermore, $\epsilon_{\boldsymbol{\mathcal{V}}}$ and $\epsilon_{\boldsymbol{\mathcal{W}}}$ account for residuals while extracting R components.

Note that the Tucker decompositions in aforementioned procedure are not unique due to permutation, rotation, and scaling problems[176]. This issue can be attenuated by adding supplementary constraints including:

1) $\mathcal{G}_{\mathrm{r}}^{\mathcal{V}}$ and $\mathcal{G}_{\mathrm{r}}^{\mathcal{W}}$ are all-orthogonal.

2) $\mathbf{P}_r^{(\mathrm{j})'}\,\mathbf{P}_r^{(\mathrm{j})} = \mathbf{I}$ and $\mathbf{Q}_r^{(\mathrm{j})'}\,\mathbf{Q}_r^{(\mathrm{j})} = \mathbf{I} \quad \forall\, \mathrm{j} = 1,2,3,4.$

3) $\| \mathbf{t}_{\mathrm{r}} \|_F = 1.$

Step 2. Sequential optimization via deflation procedure.

2.1. Initialization. Extract set of factors i.e., $\left\{\mathbf{t}_1, \left\{\mathbf{P}_1^{(\mathrm{j})}\right\}_{\mathrm{j}=1}^{4}, \left\{\mathbf{Q}_1^{(\mathrm{j})}\right\}_{\mathrm{j}=1}^{4}\right\}$ for the first subtensor components by solving the following optimization procedure:

$$\mathcal{G}^{\mathcal{V}} = \mathcal{V} \times_1 \mathbf{t}_1 \times_2 \mathbf{P}_1^{(1)'} \times_3 \mathbf{P}_1^{(2)'} \times_4 \mathbf{P}_1^{(3)'} \times_5 \mathbf{P}_1^{(4)'} \tag{5.5}$$

$$\mathcal{G}^{\mathcal{W}} = \mathcal{W} \times_1 \mathbf{t}_1 \times_2 \mathbf{Q}_1^{(1)'} \times_3 \mathbf{Q}_1^{(2)'} \times_4 \mathbf{Q}_1^{(3)'} \times_5 \mathbf{Q}_1^{(4)'} \tag{5.6}$$

$$\max_{\left\{\left\{\mathbf{P}_1^{(\mathrm{j})}\right\}_{\mathrm{j}=1}^{4}, \left\{\mathbf{Q}_1^{(\mathrm{j})}\right\}_{\mathrm{j}=1}^{4}\right\}} \| \left[\langle \mathcal{V}, \mathcal{W} \rangle_{\{1;1\}}; \mathbf{P}_1^{(1)'}, \mathbf{P}_1^{(2)'}, \mathbf{P}_1^{(3)'}, \mathbf{P}_1^{(4)'}, \mathbf{Q}_1^{(1)'}, \mathbf{Q}_1^{(2)'}, \mathbf{Q}_1^{(3)'}, \mathbf{Q}_1^{(4)'} \right] \|_F^2 \tag{5.7}$$

Based on definition $\langle \mathcal{V}, \mathcal{W} \rangle_{\{1;1\}}$ is a first mode cross-covariance tensor, hence

$$\mathbf{C} = \langle \mathcal{V}, \mathcal{W} \rangle_{\{1;1\}} = \mathrm{COV}_{\{1;1\}}(\mathcal{V}, \mathcal{W}) \in \mathbb{R}^{c \times c \times n \times t \times c \times c \times n \times t} \tag{5.8}$$

Therefore, the resultant optimization problem for initialization step is as following:

$$\max_{\left\{\left\{\mathbf{P}_1^{(\mathrm{j})}\right\}_{\mathrm{j}=1}^{4}, \left\{\mathbf{Q}_1^{(\mathrm{j})}\right\}_{\mathrm{j}=1}^{4}\right\}} \| \left[\mathbf{C}; \mathbf{P}_1^{(1)'}, \mathbf{P}_1^{(2)'}, \mathbf{P}_1^{(3)'}, \mathbf{P}_1^{(4)'}, \mathbf{Q}_1^{(1)'}, \mathbf{Q}_1^{(2)'}, \mathbf{Q}_1^{(3)'}, \mathbf{Q}_1^{(4)'} \right] \|_F^2$$

$$s.t. \quad \mathbf{P}_1^{(\mathrm{j})'}\,\mathbf{P}_1^{(\mathrm{j})} = \mathbf{I}_{H_{\mathrm{j}}}\,, \mathbf{Q}_1^{(\mathrm{j})'}\,\mathbf{Q}_1^{(\mathrm{j})} = \mathbf{I}_{K_{\mathrm{j}}} \tag{5.9}$$

The abovementioned optimization is equivalent to approximation of the best subspace of the first mode cross-covariance tensor i.e., $\mathbf{C}$. Consequently, the loadings $\left\{\left\{\mathbf{P}_1^{(\mathrm{j})}\right\}_{\mathrm{j}=1}^{4}, \left\{\mathbf{Q}_1^{(\mathrm{j})}\right\}_{\mathrm{j}=1}^{4}\right\}$ can be estimated via Tucker Decomposition of $\mathbf{C}$. The higher order orthogonal iteration (HOOI) [176] is employed along with Tucker Decomposition to facilitate the convergence and compute an orthonormal basis of the dominant subspace [175]. Since objective of this algorithm is to predict

$\boldsymbol{\mathcal{W}}$ using predictor variable $\boldsymbol{\mathcal{V}}$, $\mathbf{t}_1$ must be estimated from predictor $\boldsymbol{\mathcal{V}}$. Hence, the latent vector $\mathbf{t}_1$ can be calculated by solving another optimization problem using HOOI algorithm and computed loading matrices in aforementioned optimization procedure. The optimization model for estimation of $\mathbf{t}_1$ can be written as: $\min_{\{\mathbf{t}_1\}} \| \boldsymbol{\mathcal{V}} - \left[\boldsymbol{\mathcal{G}}^{\mathcal{V}}; \mathbf{t}_1, \mathbf{P}_1^{(1)}, \mathbf{P}_1^{(2)}, \mathbf{P}_1^{(3)}, \mathbf{P}_1^{(4)}\right] \|_{\mathrm{F}}^2$,where output of this optimization model is the latent vector $\mathbf{t}_1$ such that it maximizes explained variation of $\boldsymbol{\mathcal{V}}$ for a given set of loading matrices i.e., $\left\{\mathbf{P}_1^{(\mathrm{j})}\right\}_{\mathrm{j}=1}^{4}$. Based on HOOI algorithm [176], $\mathbf{t}_1$ can be obtained by employing singular value decomposition (SVD) on the matrix $\left[\left(\boldsymbol{\mathcal{V}} \times_2 \mathbf{P}_1^{(1)'} \times_3 \mathbf{P}_1^{(2)'} \times_4 \mathbf{P}_1^{(3)'} \times_5 \mathbf{P}_1^{(4)'}\right)\right]$ and selecting first leading left singular vector , which can be shown as:

$$\mathbf{t}_1 = \mathrm{SVD}\left(\left[\left(\boldsymbol{\mathcal{V}} \times_2 \mathbf{P}_1^{(1)'} \times_3 \mathbf{P}_1^{(2)'} \times_4 \mathbf{P}_1^{(3)'} \times_5 \mathbf{P}_1^{(4)'}\right)_{(1)}\right]\right) \tag{5.10}$$

Subsequently, the residuals after extracting first component can be calculated as follows:

$$\epsilon_{\boldsymbol{\mathcal{V}}_1} = \boldsymbol{\mathcal{V}} - \boldsymbol{\mathcal{G}}^{\mathcal{V}} \times_1 \mathbf{t}_1 \times_2 \mathbf{P}_1^{(1)} \times_3 \mathbf{P}_1^{(2)} \times_4 \mathbf{P}_1^{(3)} \times_5 \mathbf{P}_1^{(4)} \tag{5.11}$$

$$\epsilon_{\boldsymbol{\mathcal{W}}_1} = \boldsymbol{\mathcal{W}} - \boldsymbol{\mathcal{G}}^{\mathcal{W}} \times_1 \mathbf{t}_1 \times_2 \mathbf{Q}_1^{(1)} \times_3 \mathbf{Q}_1^{(2)} \times_4 \mathbf{Q}_1^{(3)} \times_5 \mathbf{Q}_1^{(4)} \tag{5.12}$$

2.2. Deflation procedure.

for $r = 1 :$ R (i.e., R is the number of the latent vectors)

if $\| \epsilon_{\boldsymbol{\mathcal{V}}_r} \|_{\mathrm{F}} > \theta$ **and** $\| \epsilon_{\boldsymbol{\mathcal{W}}_r} \|_{\mathrm{F}} > \theta$

then (note that θ is a pre-defined small number)

set $\mathbf{C}_{\mathrm{r}} = \left\langle \epsilon_{\boldsymbol{\mathcal{V}}_r}, \epsilon_{\boldsymbol{\mathcal{V}}_r} \right\rangle_{\{1;1\}} = \mathrm{COV}_{\{1;1\}}\left(\epsilon_{\boldsymbol{\mathcal{V}}_r}, \epsilon_{\boldsymbol{\mathcal{V}}_r}\right)$ **then optimize**

$$\max \| [\, \mathbf{C}_{\mathrm{r}} ; \mathbf{P}_r^{(1)'}, \mathbf{P}_r^{(2)'}, \mathbf{P}_r^{(3)'}, \mathbf{P}_r^{(4)'}, \mathbf{Q}_r^{(1)'}, \mathbf{Q}_r^{(2)'}, \mathbf{Q}_r^{(3)'}, \mathbf{Q}_r^{(4)'}] \|_{\boldsymbol{F}}^{\mathbf{2}} ; \; \boldsymbol{s.t.} \;\; \mathbf{P}_r^{(\mathrm{j})'} \mathbf{P}_r^{(\mathrm{j})} = \mathbf{I}_{H_{\mathrm{j}}}, \mathbf{Q}_r^{(\mathrm{j})'} \mathbf{Q}_r^{(\mathrm{j})} = \mathbf{I}_{K_{\mathrm{j}}}$$

Output 1. $\left\{\left\{\mathbf{P}_r^{(\mathrm{j})}\right\}_{\mathrm{j}=1}^{4},\ \left\{\mathbf{Q}_r^{(\mathrm{j})}\right\}_{\mathrm{j}=1}^{4}\right\}$ **then optimize**

$$\min \| \epsilon_{\boldsymbol{\mathcal{V}}_r} - \left[\boldsymbol{\mathcal{G}}^{\boldsymbol{\mathcal{V}}_\mathrm{r}}; \mathbf{t}_r, \mathbf{P}_r^{(1)}, \mathbf{P}_r^{(2)}, \mathbf{P}_r^{(3)}, \mathbf{P}_r^{(4)}\right] \|_{\mathrm{F}}^2$$

Output 2. $\mathbf{t}_r = \mathrm{SVD}\left(\left[\left(\epsilon_{\boldsymbol{\mathcal{V}}_r} \times_2 \mathbf{P}_r^{(1)'} \times_3 \mathbf{P}_r^{(2)'} \times_4 \mathbf{P}_r^{(3)'} \times_5 \mathbf{P}_r^{(4)'}\right)_{(1)}\right]\right)$

set

$$\boldsymbol{\mathcal{G}}^{\boldsymbol{\mathcal{V}}_\mathrm{r}} = \epsilon_{\boldsymbol{\mathcal{V}}_r} \times_1 \mathbf{t}_\mathrm{r} \times_2 \mathbf{P}_r^{(1)'} \times_3 \mathbf{P}_r^{(2)'} \times_4 \mathbf{P}_r^{(3)'} \times_5 \mathbf{P}_r^{(4)'}$$

$$\boldsymbol{\mathcal{G}}^{\boldsymbol{\mathcal{W}}_\mathrm{r}} = \epsilon_{\boldsymbol{\mathcal{W}}_r} \times_1 \mathbf{t}_\mathrm{r} \times_2 \mathbf{Q}_r^{(1)'} \times_3 \mathbf{Q}_r^{(2)'} \times_4 \mathbf{Q}_r^{(3)'} \times_5 \mathbf{Q}_r^{(4)'}$$

Deflation: $\epsilon_{\boldsymbol{\mathcal{V}}_{r+1}} = \epsilon_{\boldsymbol{\mathcal{V}}_r} - \boldsymbol{\mathcal{G}}^{\boldsymbol{\mathcal{V}}_\mathrm{r}},; \epsilon_{\boldsymbol{\mathcal{W}}_{r+1}} = \epsilon_{\boldsymbol{\mathcal{W}}_r} - \boldsymbol{\mathcal{G}}^{\boldsymbol{\mathcal{W}}_\mathrm{r}}$ **else**

Terminate;

Final Output. Appropriate number of parameters $(\mathrm{R}, \mathbf{P}^{(\mathrm{j})}, \mathbf{Q}^{(\mathrm{j})}, \{\boldsymbol{\mathcal{G}}^{\boldsymbol{\mathcal{V}}_\mathrm{r}}, \boldsymbol{\mathcal{G}}^{\boldsymbol{\mathcal{W}}_\mathrm{r}}\}_{\mathrm{r}=1}^{\mathrm{R}}, \mathbf{T})$ are needed for the prediction model.

Step 3. Prediction Model. Prediction of thermal history of a new layer $\boldsymbol{\mathcal{W}}^{\mathrm{New}}$ based on previous layer $\boldsymbol{\mathcal{V}}^{\mathrm{New}}$ can be expressed by two steps:

Extracting low-dimensional latent space $\mathbf{T}^{\mathrm{New}}$ from $\boldsymbol{\mathcal{V}}^{\mathrm{New}}$ based on model parameters obtained from Step 2 i.e., $\{\boldsymbol{\mathcal{G}}^{\boldsymbol{\mathcal{V}}_\mathrm{r}}\}_{\mathrm{r}=1}^{\mathrm{R}}$, $\mathbf{P}^{(\mathrm{j})}, \mathrm{j} = 1,2,3,4$.

Predicting $\boldsymbol{\mathcal{W}}^{\mathrm{New}}$ with $\mathbf{T}^{\mathrm{New}}$, $\{\boldsymbol{\mathcal{G}}^{\boldsymbol{\mathcal{W}}_\mathrm{r}}\}_{\mathrm{r}=1}^{\mathrm{R}}$, and $\mathbf{Q}^{(\mathrm{j})}$; $\widehat{\boldsymbol{\mathcal{W}}}_{(1)}^{\mathrm{New}} \approx \mathbf{T}^{\mathrm{New}}\mathbf{Q}^{*'} = \boldsymbol{\mathcal{V}}_{(1)}^{\mathrm{New}}\mathbf{Z}\,\mathbf{Q}^{*'}$ where $\mathbf{Z}$ and $\mathbf{Q}^{*'}$ are R column matrices that can be represented as:

$$\mathrm{z_r} = \left(\mathbf{Q}_\mathrm{r}^{(1)} \otimes \mathbf{Q}_\mathrm{r}^{(2)} \otimes \mathbf{Q}_\mathrm{r}^{(3)} \otimes \mathbf{Q}_\mathrm{r}^{(4)}\right) \boldsymbol{\mathcal{G}}_{(1)}^{\boldsymbol{\mathcal{V}}_\mathrm{r}\ +} \tag{5.13}$$

$$\mathrm{q_r^*} = \boldsymbol{\mathcal{G}}_{(1)}^{\boldsymbol{\mathcal{W}}_\mathrm{r}} \left(\mathbf{P}_\mathrm{r}^{(1)} \otimes \mathbf{P}_\mathrm{r}^{(2)} \otimes \mathbf{P}_\mathrm{r}^{(3)} \otimes \mathbf{P}_\mathrm{r}^{(4)}\right)' \tag{5.14}$$

Note that "+" in $\boldsymbol{\mathcal{G}}_{(1)}^{\boldsymbol{\mathcal{V}}_\mathrm{r}\ +}$ accounts for *Moore-Penrose pseudoinverse*.

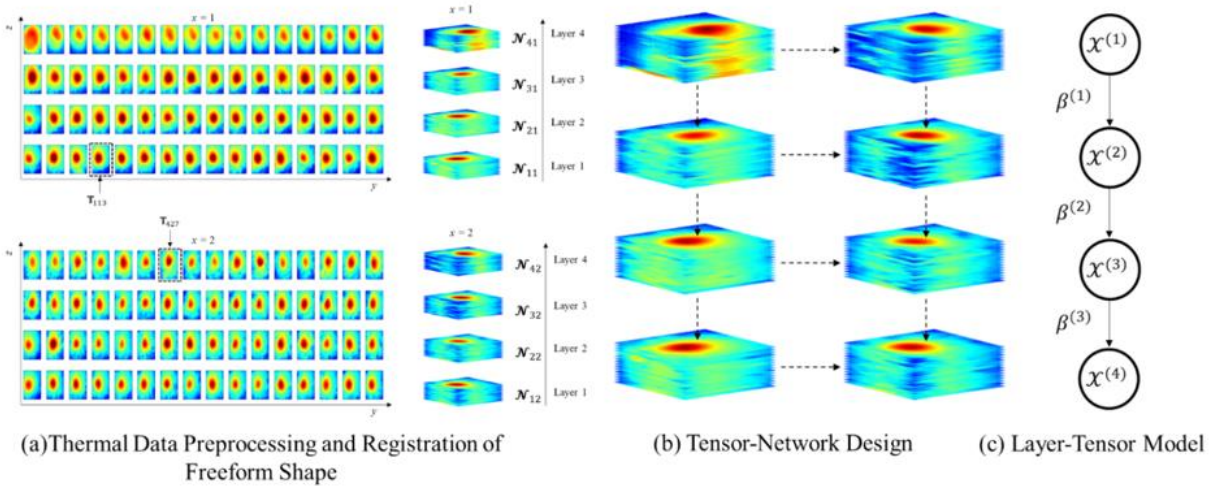

(a)Thermal Data Preprocessing and Registration of Freeform Shape (b) Tensor-Network Design (c) Layer-Tensor Model

Figure 5.1 Demonstration of layer-wise thermal history prediction model formulation where (a) shows schematic illustration of the preprocessing procedure for thermal modeling of freeform shape using tensor structure. (b) presents the network-tensor model for freeform shape based on thermal history of layer and track combination, where each node is a 3-mode tensor, (c) illustrates the layer-tensor model at which nodes are 4-mode tensor due to stack of tracks, hence arrows indicate the coefficients of tensor on tensor regression model.

5.3 Case Study: HOPLS-based layer-wise thermal history prediction of double-track wall

This section describes the numerical experiments conducted to predict the thermal history of each layer in AM parts based on the thermal images obtained within the fabrication process. Two indices including Q^2 and root mean square errors of prediction [177] are used to evaluates the accuracy of the proposed layer-wise HOPLS-based thermal history prediction. Note that index Q^2 is defined as $Q^2 = 1 - \frac{\|\mathcal{W} - \widehat{\mathcal{W}}\|_F^2}{\|\mathcal{W}\|_F^2}$, where $\widehat{\mathcal{W}}$ presents thermal history prediction of particular layer based on preceding layer via the model learned from training data. Q^2 usually varies from 0 and 1. A larger $Q^2$and a smaller RMSEP specify a better prediction performance. An OPTOMEC laser engineered net shaping (LENS) 750 system is utilized to create a double-track Ti-6Al-4V while thermal images and their spatial information are recorded with built-in

thermal imaging system. Process parameters and design conditions and experimental set-up of thermal monitoring system can be found [178]). Note that the thermal images captured by co-axial pyrometer thermal sensing system do not originally hold tensor form, and they possess multiway data structures i.e.,$\mathbf{T}_{ijk} \in \mathbb{R}^{480\times752}$ where $i = 1,2,\dots,78, j = 1,2,$ and $k = 1,2,\dots,16$ denote number of layers, tracks, and images in thermal history of double-track wall. According to the data preprocessing procedure described in section 2.1, the area of interest (AOI) for each thermal image is obtained, which denoted by $\boldsymbol{\mathcal{A}}_{ijk} \in \mathbb{R}^{30\times30}$ and is a second-order tensor.

Based on the aforementioned network-tensor structure in section 2.1, paragon of double-track Ti-6Al-4V wall is built via concatenated thermal images as shown in Figure 5.1 (b), where each node is stack of AOIs denoted by $\boldsymbol{\mathcal{N}}_{ij} \in \mathbb{R}^{30\times30\times16}$. Moreover as demonstrated in Figure 5.1 (c), nodes related to tracks in each layer are clustered in a single node, which is demonstrated by a fourth-order tensor i.e., $\boldsymbol{\mathcal{X}}^{(i)} \in \mathbb{R}^{30\times30\times16\times2}$. Consequently, the thermal history of double-track wall can be represented by 76 linked nodes, where each nodes contains the thermal of history each layer. Since in this study we are investigating a layer-wise prediction model, the thermal history of two consecutive layers are formulated as pairs of independent and dependent variables i.e., $\boldsymbol{S} = \left\{\left(\boldsymbol{\mathcal{X}}^{(i-1)}, \boldsymbol{\mathcal{X}}^{(i)}\right)\right\}_{i=2}^{76} \in \mathbb{R}^{75\times30\times30\times16\times2}$. To build a layer-wise thermal history prediction model and diminish the random fluctuation, we randomly partition $\boldsymbol{S}$ into 15 sets, where $\bigcup_{\mathrm{k}=1}^{15}\mathbf{M}_{\mathrm{k}} = \boldsymbol{S}$, $\mathbf{M}_{\mathrm{k}}\cap\mathbf{M}_{\mathrm{k}'} = \phi \;\; \forall\, \mathrm{k}, \mathrm{k}' = 1,2,\dots,15 \;;\; \mathrm{k} \neq \mathrm{k}'$ and $\mathbf{M}_{\mathrm{k}}, \mathbf{M}_{\mathrm{k}'}$. More specifically, $\mathbf{M}_{\mathrm{k}} = (\boldsymbol{\mathcal{V}}\, \boldsymbol{\mathcal{W}})$ is a set of tensor pair, where $\boldsymbol{\mathcal{V}}, \boldsymbol{\mathcal{W}} \in \mathbb{R}^{5\times30\times30\times16\times2}$. The tuning process for the HOPLS is accomplished by randomly selecting a set from 15 sets and applying the five-fold cross validation on the chosen set. Subsequently, the parameters for layer-wise thermal history prediction model are estimated. At last, remainder of sets are utilized to validate the efficiency of HOPLS in layer-wise prediction,

an extensive comparative exploration has been performed on thermal history of double-track Ti-6Al-4V to evaluate the prediction performance under varying conditions. For example, by applying the above-mentioned prediction scheme on $\mathbf{M}_1 = (\boldsymbol{\mathcal{V}}\ \boldsymbol{\mathcal{W}}) = \{(\boldsymbol{\mathcal{X}}^{(20)}, \boldsymbol{\mathcal{X}}^{(21)}), (\boldsymbol{\mathcal{X}}^{(47)}, \boldsymbol{\mathcal{X}}^{(48)}), (\boldsymbol{\mathcal{X}}^{(63)}, \boldsymbol{\mathcal{X}}^{(64)}), (\boldsymbol{\mathcal{X}}^{(68)}, \boldsymbol{\mathcal{X}}^{(69)}), (\boldsymbol{\mathcal{X}}^{(69)}, \boldsymbol{\mathcal{X}}^{(70)})\}$, the number of latent vectors (R) and loadings ($\{H_1, H_2, H_3, H_4, K_1, K_2, K_3, K_4\}$) are determined. Based on the model learned from training data, the optimal parameter for the number of latent vectors (R) is determined to be two, where cumulative percent variance explained by these first two latent vectors is calculated to be 99.43%, on the average. Moreover, the best values for number of loadings are $\{H_1 = H_2 = H_3 = H_4 = 2\}$ and $\{K_1 = K_2 = K_3 = K_4 = 2\}$ while 99.965% and 99.966% of cumulative percent variance for $\boldsymbol{\mathcal{V}}$ and $\boldsymbol{\mathcal{W}}$ have been captured, respectively. In addition, the correlation between two tensors by projecting them into a latent subspace and independent loading subspaces, is 0.97759. On the average, HOPLS prediction performance indices (i.e., $\boldsymbol{Q^2} = 0.999$ and RMSEP = 31.212 ℃) demonstrate significant efficiency in prediction of layer-wise thermal history prediction. For instance, Figure 5.2 demonstrates the RMSEP for applying the learned model on layers {5, 6, 7, 8, 9} to predict thermal history of layers {6, 7, 8, 9, 10}, where it varies from 10 ℃ to 62 ℃. This does not imply a significant prediction inaccuracy in this particular study. However, RMSEPs for handful of AOIs indicate nearly significant dissimilarity compared to actual AOIs, which anomaly/porosity detection techniques can corroborate the reasons behind these inaccuracies.

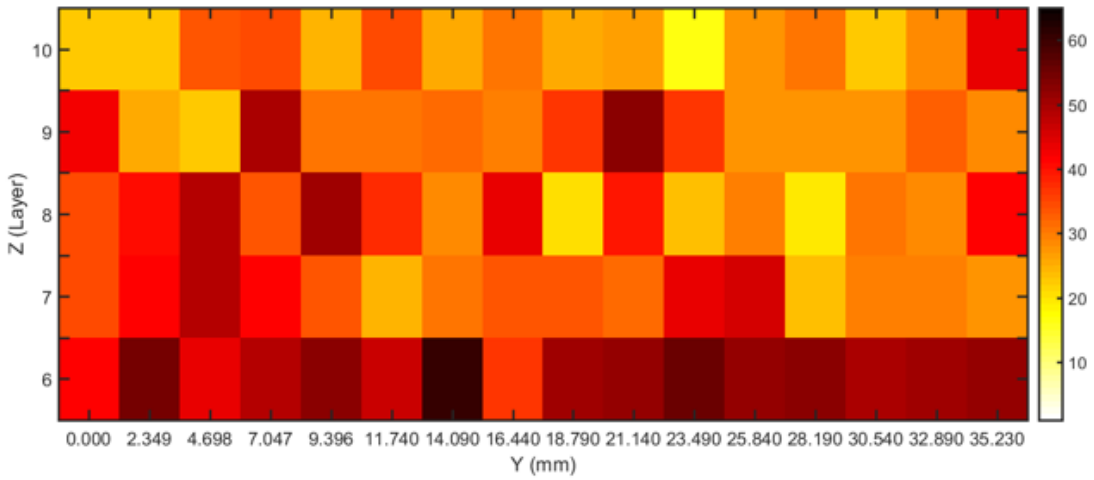

Figure 5.2 Demonstrating RMSEP for each AOI in layers 6 to 10.

5.4 Summary and conclusion

In-situ thermal behavior exploration of consecutive deposited layers is imperative to acquire the desired microstructural and excellent mechanical properties. Most of the existing physics-based models are not competent to yield detailed interpretation and intelligence of AM processes. Compared to conventional processes, alloys used in AM processes lead to complexity and uncertainty in thermal history prediction and characterization of AM processes. Major findings of this paper compared to the existing state-of-the-art studies on thermal history prediction of AM parts are as follows:

We develop a novel tensor-network structure to account for design and fabrication procedure of freeform shapes in AM process. Also, we propose a thermal history prediction model that enable us to predict the thermal history of each layer, which eventually can be used to predict the temperature distribution of melt pool in each specific location within the layer and track.

We utilize HOPLS to establish a layer-wise relationship in the thermal history of the AM part, which has superior properties compared to available prediction models (e.g., N-PLS)

including robustness to noise, ease of interpretation, computationally efficient, flexibility to tuning parameters, and robustness to large number of variables with small sample size.

Predictability and root mean square errors of prediction (RMSEP) for proposed HOPLS-based thermal history prediction method are calculated, which indicate proficient prediction performance. Statistics obtained in this study (i.e., RMSEP, Q^2) can be used for layer-wise and location-based anomaly detection. Furthermore, incorporating the proposed approach with recently developed machine learning approaches can lead to surrogate modeling of AM parts with various process conditions and complex geometries.

The study in this chapter can be potentially extended in the following directions. Firstly, the modeling accuracy (i.e. Q2 and RMSEP) can be potentially varying with respect to different layers, tracks, and locations. A thorough study on the modeling accuracy variability can be very helpful for practitioners to understand the fidelity of the predicted results. Secondly, the proposed model implicitly assumes that the thermal history is collected under normal operating conditions. It will be interesting to investigate how the model changes when there is a process anomaly occurring in some of the training/testing layers. Thirdly, it will be interesting to benchmark the RMSEP of the proposed method with the RMSEP obtained from using the grand mean of thermal distribution for prediction. An improved RMSEP will validate that the HOPLS can accurately capture some statistical relationship between the neighboring layers/tracks.

CHAPTER VI

CONCLUSION AND FUTURE RESEARCH

6.1 Chapter Structure

This chapter completes the dissertation by outlining the research summary and enumerating the future research directions. Each of the listed items have a subsection dedicated to them.

6.2 Research Summary

Additive manufacturing (AM) continues to demonstrate potential for full-scale production and repair of complex and highly-customized parts; arguably, this potential can leverage the U.S. to become a leader in advanced manufacturing, resulting in serious economic impact for automotive, aerospace, biomedical, and other major industries. However, to achieve effective and economical production of functional metallic components via AM, a number of crucial technical challenges must be addressed, including: (1) accurate prediction of the anomalies of additively-manufactured metallic parts; (2) predictive modeling of their behavior during their build and while in service; (3) control of the manufacturing process to produce functional parts with targeted properties and performance characteristics; and (4) establishing process/testing standards for characterizing post-fabricated mechanical properties.

This dissertation in additive manufacturing (AM) was accompanied by the fields of machine and statistical learning of big data; specifically, in-situ and online monitoring of process signatures for porosity detection in AM parts are now used as functional parts within many industrial sectors

such as tooling, dental, medical, and aerospace. This dissertation offers novel analytical and theoretical skillset for effectively addressing the major problems in AM as demonstrated here:

- Thermo-physical dynamics of Directed Energy Deposition (DED) processes using unsupervised machine learning methods.
- Porosity prediction: Supervised-learning of thermal history for direct laser deposition.
- Dual process monitoring of metal-based additive manufacturing using tensor decomposition of thermal image streams.
- Quantifying geometric accuracy with unsupervised machine learning.
- Fast Prediction of Thermal History for Direct Laser Deposition Processes Using Network-based Tensor Regression

6.3 Future Research

The presented dissertation is only the beginning for an emerging research trend: in-situ monitoring and qualification of AM parts using machine and statistical learning. The list of future research avenues are as following:

1) **Sensing and real-time process control for complex shapes.**

The objective of this study is to model the AM parts with complex shape using a network frame and detect different type of defects based on reduced tensor-based features. The outcome of this research can be used to track the dynamic of the AM process and mitigate the poor repeatability and reliability.

2) **Investigating feasibility of using AM for repairment.**

The preliminary study for this topic is to determine whether or not interrupting the build of a part created with laser powder bed fusion (LPBF) process has any effect on the mechanical and micro-structure properties of the part by looking at the surface integrity.

3) Reliability assessment of AM parts based on fatigue performance.

The overarching goal of this research is to use existing in-situ defect detection algorithm and fatigue-life prediction models for in-situ qualification of AM parts using the characteristics (i.e. size and location) of detected defects. Toward achieving this goal, the research objectives of this study are to:

- Expand in-situ defect detection technique toward multi-track parts fabricated using LENS machine.
- Quantify the reliability of fabricated parts based on their fatigue performance and determine the most dangerous defects—in terms of size and location—formed during the process.

The main motivation of the proposed study has arisen from a crucial need for in-situ qualification and certification of parts fabricated using AM techniques. With the advances of closed loop, controllable AM machines, developing a real-time algorithm for performance-based qualification and certification is of immediate importance. For metal AM techniques, fatigue certification requirements proved to be some of the most challenging ones to meet. Fatigue performance of a part may not necessarily be dominated by the largest defect; rather a combination of defect characteristics (i.e. size, shape, location, and distribution) typically compete together for initiating cracks. For instance, an AM part consisting of high intra-part void density (i.e. large voids or a cluster of voids) located far from the surface still does not exceed the dominating and detrimental influence of a near-surface void with regards to fatigue performance. Thus, a

successful in-situ qualification and certification algorithm requires not only the ability to identify the formation of defects during the build process, but also to link the characteristics of detected defects to the performance and durability of fabricated parts**.** With the high national interest in AM, the area of process monitoring and mechanical behavior of AM parts is of immediate importance as it allows end-users the ability to 'design for AM' and to gain trust in part mechanical performance during application.

REFERENCES

[1] A. Emelogu, M. Marufuzzaman, S. M. Thompson, N. Shamsaei, and L. Bian, "Additive manufacturing of biomedical implants: A feasibility assessment via supply-chain cost analysis," *Additive Manufacturing*, vol. 11, pp. 97-113, 2016.

[2] T. Wohlers, *Wohlers report 2016*. Wohlers Associates, Inc, 2016.

[3] M. Grasso and B. M. Colosimo, "Process defects and in situ monitoring methods in metal powder bed fusion: a review," *Measurement Science and Technology*, vol. 28, no. 4, p. 044005, 2017.

[4] G. Tapia and A. Elwany, "A review on process monitoring and control in metal-based additive manufacturing," *Journal of Manufacturing Science and Engineering*, vol. 136, no. 6, p. 060801, 2014.

[5] N. Shamsaei, A. Yadollahi, L. Bian, and S. M. Thompson, "An overview of Direct Laser Deposition for additive manufacturing; Part II: Mechanical behavior, process parameter optimization and control," *Additive Manufacturing*, vol. 8, pp. 12-35, 2015.

[6] S. M. Thompson, L. Bian, N. Shamsaei, and A. Yadollahi, "An overview of Direct Laser Deposition for additive manufacturing; Part I: Transport phenomena, modeling and diagnostics," *Additive Manufacturing*, vol. 8, pp. 36-62, 2015.

[7] S. K. Everton, M. Hirsch, P. Stravroulakis, R. K. Leach, and A. T. Clare, "Review of in-situ process monitoring and in-situ metrology for metal additive manufacturing," *Materials & Design*, vol. 95, pp. 431-445, 2016.

[8] Y. Huang, M. C. Leu, J. Mazumder, and A. Donmez, "Additive manufacturing: current state, future potential, gaps and needs, and recommendations," *Journal of Manufacturing Science and Engineering*, vol. 137, no. 1, p. 014001, 2015.

[9] W. Gao *et al.*, "The status, challenges, and future of additive manufacturing in engineering," *Computer-Aided Design*, vol. 69, pp. 65-89, 2015.

[10] G. Ameta, P. Witherell, S. Moylan, and R. Lipman, "Tolerance Specification and Related Issues for Additively Manufactured Products," in *ASME 2015 International Design Engineering Technical Conferences & Computers and Information in Engineering Conference, IDETC/CIE 2015*, 2015.

[11] S.-A. Tahan and S. Levesque, "Exploiting the process capability of profile tolerance according GD&T ASME-Y14. 5M," in *Computers & Industrial Engineering, 2009. CIE 2009. International Conference on*, 2009, pp. 1285-1290: IEEE.

[12] T. Hua, C. Jing, L. Xin, Z. Fengying, and H. Weidong, "Research on molten pool temperature in the process of laser rapid forming," *journal of materials processing technology*, vol. 198, no. 1, pp. 454-462, 2008.

[13] M. Seifi, A. Salem, J. Beuth, O. Harrysson, and J. J. Lewandowski, "Overview of materials qualification needs for metal additive manufacturing," *JoM*, vol. 68, no. 3, pp. 747-764, 2016.

[14] A. J. Pinkerton and L. Li, "Modelling the geometry of a moving laser melt pool and deposition track via energy and mass balances," *Journal of Physics D: Applied Physics*, vol. 37, no. 14, p. 1885, 2004.

[15] H. Qi, J. Mazumder, and H. Ki, "Numerical simulation of heat transfer and fluid flow in coaxial laser cladding process for direct metal deposition," *Journal of applied physics*, vol. 100, no. 2, p. 024903, 2006.

[16] N. Chandrasekhar, M. Vasudevan, A. Bhaduri, and T. Jayakumar, "Intelligent modeling for estimating weld bead width and depth of penetration from infra-red thermal images of the weld pool," *Journal of Intelligent Manufacturing*, vol. 26, no. 1, pp. 59-71, 2015.

[17] L. Tang and R. G. Landers, "Melt Pool Temperature Control for Laser Metal Deposition Processes—Part I: Online Temperature Control," *Journal of manufacturing science and engineering*, vol. 132, no. 1, p. 011010, 2010.

[18] J.-D. Kim and Y. Peng, "Melt pool shape and dilution of laser cladding with wire feeding," *Journal of Materials Processing Technology*, vol. 104, no. 3, pp. 284-293, 2000.

[19] M. Picasso and A. Hoadley, "Finite element simulation of laser surface treatments including convection in the melt pool," *International Journal of Numerical Methods for Heat & Fluid Flow*, vol. 4, no. 1, pp. 61-83, 1994.

[20] L. Tang, T. E. Sparks, J. Ruan, R. G. Landers, and F. W. Liou, "Online Melt Pool Temperature Control for Laser Metal Deposition Processes," 2009.

[21] C. Gáspár, "Multigrid technique for biharmonic interpolation with application to dual and multiple reciprocity method," *Numerical Algorithms*, vol. 21, no. 1, pp. 165-183, 1999.

[22] D. Hale, "Image-guided blended neighbor interpolation," *CWP Report*, vol. 634, p. 634, 2009.

[23] D. T. Sandwell, "Biharmonic spline interpolation of GEOS-3 and SEASAT altimeter data," *Geophysical research letters*, vol. 14, no. 2, pp. 139-142, 1987.

[24] J. Mireles, S. Ridwan, P. A. Morton, A. Hinojos, and R. B. Wicker, "Analysis and correction of defects within parts fabricated using powder bed fusion technology," *Surface Topography: Metrology and Properties*, vol. 3, no. 3, p. 034002, 2015.

[25] J.-P. Kruth, J. Duflou, P. Mercelis, J. Van Vaerenbergh, T. Craeghs, and J. De Keuster, "On-line monitoring and process control in selective laser melting and laser cutting," in *Proceedings of the 5th Lane Conference, Laser Assisted Net Shape Engineering*, 2007, vol. 1, pp. 23-37.

[26] F. Tajeripour and S. Fekri-Ershad, "Porosity detection by using improved local binary pattern," in *Proc. of the 11th WSEAS Intl. Conf. on Signal Processing, Robotics and Automation (ISPRA'12)*, 2012, vol. 1, pp. 116-121.

[27] E. Eren, S. Kurama, and I. Solodov, "Characterization of porosity and defect imaging in ceramic tile using ultrasonic inspections," *Ceramics International*, vol. 38, no. 3, pp. 2145-2151, 2012.

[28] O. Abraham, B. Piwakowski, G. Villain, and O. Durand, "Non-contact, automated surface wave measurements for the mechanical characterisation of concrete," *Construction and Building Materials*, vol. 37, pp. 904-915, 2012.

[29] V. Garnier, B. Piwakowski, O. Abraham, G. Villain, C. Payan, and J. F. Chaix, "Acoustic techniques for concrete evaluation: improvements, comparisons and consistency," *Construction and Building Materials*, vol. 43, pp. 598-613, 2013.

[30] M. Goueygou, Z. Lafhaj, and F. Soltani, "Assessment of porosity of mortar using ultrasonic Rayleigh waves," *NdT & E International*, vol. 42, no. 5, pp. 353-360, 2009.

[31] Z. Lafhaj, M. Goueygou, A. Djerbi, and M. Kaczmarek, "Correlation between porosity, permeability and ultrasonic parameters of mortar with variable water/cement ratio and water content," *Cement and Concrete Research*, vol. 36, no. 4, pp. 625-633, 2006.

[32] F. Soltani, M. Goueygou, Z. Lafhaj, and B. Piwakowski, "Relationship between ultrasonic Rayleigh wave propagation and capillary porosity in cement paste with variable water content," *NDT & E International*, vol. 54, pp. 75-83, 2013.

[33] T. Kowaluk and A. Woźniak, "Study of porosity measurement using the computer tomograph," *Pomiary Automatyka Robotyka*, vol. 16, no. 12, pp. 82-86, 2012.

[34] C. Meola and C. Toscano, "Flash thermography to evaluate porosity in carbon fiber reinforced polymer (CFRPs)," *Materials*, vol. 7, no. 3, pp. 1483-1501, 2014.

[35] J. M. Wells, "Quantitative XCT evaluation of porosity in an aluminum alloy casting," in *Shape casting: 2nd international symposium. ISBN*, 2007, pp. 978-0.

[36] X. Cai, A. A. Malcolm, B. S. Wong, and Z. Fan, "Measurement and characterization of porosity in aluminium selective laser melting parts using X-ray CT," *Virtual and Physical Prototyping*, vol. 10, no. 4, pp. 195-206, 2015.

[37] J. Schwerdtfeger, R. F. Singer, and C. Körner, "In situ flaw detection by IR-imaging during electron beam melting," *Rapid Prototyping Journal*, vol. 18, no. 4, pp. 259-263, 2012.

[38] K.-C. Fan, S.-H. Chen, J.-Y. Chen, and W.-B. Liao, "Development of auto defect classification system on porosity powder metallurgy products," *NDT & E International*, vol. 43, no. 6, pp. 451-460, 2010.

[39] S. Clijsters, T. Craeghs, S. Buls, K. Kempen, and J.-P. Kruth, "In situ quality control of the selective laser melting process using a high-speed, real-time melt pool monitoring system," *The International Journal of Advanced Manufacturing Technology*, vol. 75, no. 5-8, pp. 1089-1101, 2014.

[40] J. Hunt, "Steady state columnar and equiaxed growth of dendrites and eutectic," *Materials science and engineering*, vol. 65, no. 1, pp. 75-83, 1984.

[41] P. Kobryn and S. Semiatin, "The laser additive manufacture of Ti-6Al-4V," *JOM Journal of the Minerals, Metals and Materials Society*, vol. 53, no. 9, pp. 40-42, 2001.

[42] P. A. Kobryn and S. Semiatin, "Microstructure and texture evolution during solidification processing of Ti–6Al–4V," *Journal of Materials Processing Technology*, vol. 135, no. 2, pp. 330-339, 2003.

[43] J. Gockel, J. Beuth, and K. Taminger, "Integrated control of solidification microstructure and melt pool dimensions in electron beam wire feed additive manufacturing of Ti-6Al-4V," *Additive Manufacturing*, vol. 1, pp. 119-126, 2014.

[44] S. A. Khairallah, A. T. Anderson, A. Rubenchik, and W. E. King, "Laser powder-bed fusion additive manufacturing: Physics of complex melt flow and formation mechanisms of pores, spatter, and denudation zones," *Acta Materialia*, vol. 108, pp. 36-45, 2016.

[45] M. Shiomi, A. Yoshidome, F. Abe, and K. Osakada, "Finite element analysis of melting and solidifying processes in laser rapid prototyping of metallic powders," *International Journal of Machine Tools and Manufacture*, vol. 39, no. 2, pp. 237-252, 1999.

[46] D. Hu and R. Kovacevic, "Modelling and measuring the thermal behaviour of the molten pool in closed-loop controlled laser-based additive manufacturing," *Proceedings of the Institution of Mechanical Engineers, Part B: Journal of Engineering Manufacture*, vol. 217, no. 4, pp. 441-452, 2003.

[47] M. R. Boddu, R. G. Landers, and F. W. Liou, "Control of laser cladding for rapid prototyping—A review," in *Proceedings of the Solid Freeform Fabrication Symposium*, 2001, pp. 6-8.

[48] P. Vetter, T. Engel, and J. Fontaine, "Laser cladding: the relevant parameters for process control," in *Proc. SPIE*, 1994, vol. 2207, pp. 452-462.

[49] A. Nassar, T. Spurgeon, and E. Reutzel, "Sensing defects during directed-energy additive manufacturing of metal parts using optical emissions spectroscopy," in *Solid Freeform Fabrication Symposium Proceedings*, 2014: University of Texas Austin, TX.

[50] S. Siddique *et al.*, "Computed tomography for characterization of fatigue performance of selective laser melted parts," *Materials & Design*, vol. 83, pp. 661-669, 2015.

[51] A. R. Nassar, J. S. Keist, E. W. Reutzel, and T. J. Spurgeon, "Intra-layer closed-loop control of build plan during directed energy additive manufacturing of Ti–6Al–4V," *Additive Manufacturing*, vol. 6, pp. 39-52, 2015.

[52] Y. Ding, J. Warton, and R. Kovacevic, "Development of sensing and control system for robotized laser-based direct metal addition system," *Additive Manufacturing*, vol. 10, pp. 24-35, 2016.

[53] J. Heigel, P. Michaleris, and E. Reutzel, "Thermo-mechanical model development and validation of directed energy deposition additive manufacturing of Ti–6Al–4V," *Additive manufacturing*, vol. 5, pp. 9-19, 2015.

[54] A. Birnbaum, P. Aggarangsi, and J. L. Beuth, "Process scaling and transient melt pool size control in laser-based additive manufacturing processes," in *Solid Freeform Fabrication Proceedings*, 2003, pp. 328-339: Proc. 2003 Solid Freeform Fabrication Symposium, Austin.

[55] I. H. Ahn *et al.*, "Characteristic length of the solidified melt pool in selective laser melting process," *Rapid Prototyping Journal*, vol. 23, no. 2, pp. 370-381, 2017.

[56] C. Doumanidis and Y.-M. Kwak, "Geometry modeling and control by infrared and laser sensing in thermal manufacturing with material deposition," *TRANSACTIONS-AMERICAN SOCIETY OF MECHANICAL ENGINEERS JOURNAL OF MANUFACTURING SCIENCE AND ENGINEERING*, vol. 123, no. 1, pp. 45-52, 2001.

[57] Q. Wang, J. Li, M. Gouge, A. R. Nassar, P. P. Michaleris, and E. W. Reutzel, "Physics-Based Multivariable Modeling and Feedback Linearization Control of Melt-Pool Geometry and Temperature in Directed Energy Deposition," *Journal of Manufacturing Science and Engineering*, vol. 139, no. 2, p. 021013, 2017.

[58] S. Li *et al.*, "Melt-pool motion, temperature variation and dendritic morphology of Inconel 718 during pulsed-and continuous-wave laser additive manufacturing: A comparative study," *Materials & Design*, vol. 119, pp. 351-360, 2017.

[59] G. Bi, A. Gasser, K. Wissenbach, A. Drenker, and R. Poprawe, "Identification and qualification of temperature signal for monitoring and control in laser cladding," *Optics and lasers in engineering*, vol. 44, no. 12, pp. 1348-1359, 2006.

[60] L. Song and J. Mazumder, "Feedback control of melt pool temperature during laser cladding process," *IEEE Transactions on Control Systems Technology,* vol. 19, no. 6, pp. 1349-1356, 2011.

[61] M. Tang, P. C. Pistorius, and J. L. Beuth, "Prediction of lack-of-fusion porosity for powder bed fusion," *Additive Manufacturing,* vol. 14, pp. 39-48, 2017.

[62] R. Cunningham, S. P. Narra, C. Montgomery, J. Beuth, and A. Rollett, "Synchrotron-based X-ray microtomography characterization of the effect of processing variables on porosity formation in laser power-bed additive manufacturing of Ti-6Al-4V," *Jom,* vol. 69, no. 3, pp. 479-484, 2017.

[63] J. Dilip *et al.*, "Influence of processing parameters on the evolution of melt pool, porosity, and microstructures in Ti-6Al-4V alloy parts fabricated by selective laser melting," *Progress in Additive Manufacturing,* pp. 1-11, 2017.

[64] E. Soylemez, J. L. Beuth, and K. Taminger, "Controlling melt pool dimensions over a wide range of material deposition rates in electron beam additive manufacturing," in *Proceedings of 21st Solid Freeform Fabrication Symposium, Austin, TX, Aug*, 2010, pp. 9-11.

[65] A. K. R. JAFARI-MARANDI, "Webpage clustering–taking the zero step: a case study of an Iranian website," *Journal of Web Engineering,* vol. 13, no. 3&4, pp. 333-360, 2014.

[66] D. Pratiwi, "The use of self organizing map method and feature selection in image database classification system," *arXiv preprint arXiv:1206.0104*, 2012.

[67] E. Merényi, M. J. Mendenhall, and P. O'Driscoll, "Advances in Self-Organizing Maps and Learning Vector Quantization," 2016.

[68] R. K. Patel and V. Giri, "Analysis and Interpretation of Bearing Vibration Data Using Principal Component Analysis and Self-Organizing Map," *International Journal of Advanced Design and Manufacturing Technology*, vol. 9, no. 1, 2016.

[69] B. Fritzke, "Growing grid—a self-organizing network with constant neighborhood range and adaptation strength," *Neural processing letters,* vol. 2, no. 5, pp. 9-13, 1995.

[70] G. J. Marshall, S. M. Thompson, and N. Shamsaei, "Data indicating temperature response of Ti–6Al–4V thin-walled structure during its additive manufacture via Laser Engineered Net Shaping," *Data in brief,* vol. 7, pp. 697-703, 2016.

[71] J. Hsieh, *Computed tomography: principles, design, artifacts, and recent advances*. SPIE press, 2003.

[72] L. De Chiffre, S. Carmignato, J.-P. Kruth, R. Schmitt, and A. Weckenmann, "Industrial applications of computed tomography," *CIRP Annals-Manufacturing Technology,* vol. 63, no. 2, pp. 655-677, 2014.

[73] J. P. Kruth, M. Bartscher, S. Carmignato, R. Schmitt, L. De Chiffre, and A. Weckenmann, "Computed tomography for dimensional metrology," *CIRP Annals-Manufacturing Technology,* vol. 60, no. 2, pp. 821-842, 2011.

[74] M. Khanzadeh, L. Bian, N. Shamsaei, and S. M. Thompson, "Porosity Detection of Laser Based Additive Manufacturing Using Melt Pool Morphology Clustering," in *Solid Freeform Fabrication* Austin,TX, 2016, pp. 1487-1494.

[75] M. Mahesh, Y. Wong, J. Fuh, and H. Loh, "Benchmarking for comparative evaluation of RP systems and processes," *Rapid Prototyping Journal,* vol. 10, no. 2, pp. 123-135, 2004.

[76] A. Criminisi, I. Reid, and A. Zisserman, "Single view metrology," *International Journal of Computer Vision,* vol. 40, no. 2, pp. 123-148, 2000.

[77] J. Hiller and P. Hornberger, "Measurement accuracy in X-ray computed tomography metrology: Toward a systematic analysis of interference effects in tomographic imaging," *Precision Engineering,* vol. 45, pp. 18-32, 2016.

[78] J. K. Davidson, J. J. Shah, and A. Mujezinović, "Method and apparatus for geometric variations to integrate parametric computer aided design with tolerance analyses and optimization," ed: Google Patents, 2005.

[79] R. Malkin, M. Caleap, and B. W. Drinkwater, "A numerical database for ultrasonic defect characterisation using array data: robustness and accuracy," *NDT & E International,* vol. 83, pp. 94-103, 2016.

[80] B. Schleich, N. Anwer, L. Mathieu, and S. Wartzack, "Skin model shapes: A new paradigm shift for geometric variations modelling in mechanical engineering," *Computer-Aided Design,* vol. 50, pp. 1-15, 2014.

[81] P. K. Rao, Z. Kong, C. E. Duty, R. J. Smith, V. Kunc, and L. J. Love, "Assessment of dimensional integrity and spatial defect localization in additive manufacturing using spectral graph theory," *Journal of Manufacturing Science and Engineering,* vol. 138, no. 5, p. 051007, 2016.

[82] J. G. Zhou, D. Herscovici, and C. C. Chen, "Parametric process optimization to improve the accuracy of rapid prototyped stereolithography parts," *International Journal of Machine Tools and Manufacture,* vol. 40, no. 3, pp. 363-379, 2000.

[83] S. Campanelli, G. Cardano, R. Giannoccaro, A. Ludovico, and E. L. Bohez, "Statistical analysis of the stereolithographic process to improve the accuracy," *Computer-Aided Design,* vol. 39, no. 1, pp. 80-86, 2007.

[84] S. Onuh and K. Hon, "Improving stereolithography part accuracy for industrial applications," *The International Journal of Advanced Manufacturing Technology,* vol. 17, no. 1, pp. 61-68, 2001.

[85] H. Chen, H. Chen, Y. F. Zhao, and Y. F. Zhao, "Process parameters optimization for improving surface quality and manufacturing accuracy of binder jetting additive manufacturing process," *Rapid Prototyping Journal*, vol. 22, no. 3, pp. 527-538, 2016.

[86] R.-J. Wang, L. Wang, L. Zhao, and Z. Liu, "Influence of process parameters on part shrinkage in SLS," *The International Journal of Advanced Manufacturing Technology*, vol. 33, no. 5, pp. 498-504, 2007.

[87] A. Noriega, D. Blanco, B. Alvarez, and A. Garcia, "Dimensional accuracy improvement of FDM square cross-section parts using artificial neural networks and an optimization algorithm," *The International Journal of Advanced Manufacturing Technology*, vol. 69, no. 9-12, pp. 2301-2313, 2013.

[88] J. Gao, N. Gindy, and D. Clark, "Extraction/conversion of geometric dimensions and tolerances for machining features," *The International Journal of Advanced Manufacturing Technology*, vol. 26, no. 4, pp. 405-414, 2005.

[89] M. Khanzadeh, R. J. Marandi, M. S. Tootooni, L. Bian, B. Smith, and P. Rao, "Profiling and Optimizing the Geometric Accuracy of Additively Manufactured Components via Self-Organizing Map," in *Solid Freeform Fabrication* Austin, TX, 2016, pp. 1303-1313.

[90] W. King *et al.*, "Laser powder bed fusion additive manufacturing of metals; physics, computational, and materials challenges," *Applied Physics Reviews*, vol. 2, no. 4, p. 041304, 2015.

[91] D. Pal, N. Patil, M. Nikoukar, K. Zeng, K. H. Kutty, and B. E. Stucker, "An integrated approach to cyber-enabled additive manufacturing using physics based, coupled multi-scale process modeling," in *Proceedings of SFF Symposium, Austin, TX, Aug*, 2013, pp. 12-14.

[92] R. Paul, S. Anand, and F. Gerner, "Effect of thermal deformation on part errors in metal powder based additive manufacturing processes," *Journal of Manufacturing Science and Engineering*, vol. 136, no. 3, p. 031009, 2014.

[93] C.-P. Jiang, Y.-M. Huang, and C.-H. Liu, "Dynamic finite element analysis of photopolymerization in stereolithography," *Rapid Prototyping Journal*, vol. 12, no. 3, pp. 173-180, 2006.

[94] Q. Huang, J. Zhang, A. Sabbaghi, and T. Dasgupta, "Optimal offline compensation of shape shrinkage for three-dimensional printing processes," *IIE Transactions*, vol. 47, no. 5, pp. 431-441, 2015.

[95] J. Barnfather, M. Goodfellow, and T. Abram, "A performance evaluation methodology for robotic machine tools used in large volume manufacturing," *Robotics and Computer-Integrated Manufacturing*, vol. 37, pp. 49-56, 2016.

[96] A. Cooke and J. Soons, "Variability in the geometric accuracy of additively manufactured test parts," in *21st annual international solid freeform fabrication symposium, Austin, Texas, USA*, 2010, pp. 1-12.

[97] S. Moylan, A. Cooke, K. Jurrens, J. Slotwinski, and M. A. Donmez, "A review of test artifacts for additive manufacturing," *National Institute of Standards and Technology (NIST), Gaithersburg, MD, Report No. NISTIR*, vol. 7858, 2012.

[98] J. Huang and C.-H. Menq, "Automatic CAD model reconstruction from multiple point clouds for reverse engineering," *Journal of Computing and Information Science in Engineering*, vol. 2, no. 3, pp. 160-170, 2002.

[99] H. Woo, E. Kang, S. Wang, and K. H. Lee, "A new segmentation method for point cloud data," *International Journal of Machine Tools and Manufacture*, vol. 42, no. 2, pp. 167-178, 2002.

[100] R. Schnabel, R. Wahl, and R. Klein, "Efficient RANSAC for point-cloud shape detection," in *Computer graphics forum*, 2007, vol. 26, no. 2, pp. 214-226: Wiley Online Library.

[101] G. Liu, Y. Wong, Y. Zhang, and H. Loh, "Modelling cloud data for prototype manufacturing," *Journal of materials processing technology*, vol. 138, no. 1, pp. 53-57, 2003.

[102] W. Sun, C. Bradley, Y. Zhang, and H. T. Loh, "Cloud data modelling employing a unified, non-redundant triangular mesh," *Computer-Aided Design*, vol. 33, no. 2, pp. 183-193, 2001.

[103] R. Fabio, "From point cloud to surface: the modeling and visualization problem," *International Archives of Photogrammetry, Remote Sensing and Spatial Information Sciences*, vol. 34, no. 5, p. W10, 2003.

[104] F. Mémoli and G. Sapiro, "A theoretical and computational framework for isometry invariant recognition of point cloud data," *Foundations of Computational Mathematics*, vol. 5, no. 3, pp. 313-347, 2005.

[105] A. M. Aboutaleb, M. A. Tschopp, P. K. Rao, and L. Bian, "Multi-Objective Accelerated Process Optimization of Part Geometric Accuracy in Additive Manufacturing," *Journal of Manufacturing Science and Engineering*, vol. 139, no. 10, p. 101001, 2017.

[106] M. S. Tootooni, A. Dsouza, R. Donovan, P. K. Rao, Z. J. Kong, and P. Borgesen, "Classifying the Dimensional Variation in Additive Manufactured Parts From Laser-Scanned Three-Dimensional Point Cloud Data Using Machine Learning Approaches," *Journal of Manufacturing Science and Engineering*, vol. 139, no. 9, p. 091005, 2017.

[107] M. S. Tootooni, A. Dsouza, R. Donovan, P. K. Rao, Z. J. Kong, and P. Borgesen, "Assessing the Geometric Integrity of Additive Manufactured Parts From Point Cloud Data Using Spectral Graph Theoretic Sparse Representation-Based Classification," in *ASME 2017 12th International Manufacturing Science and Engineering Conference collocated with the JSME/ASME 2017 6th International Conference on Materials and Processing*, 2017, pp. V002T01A042-V002T01A042: American Society of Mechanical Engineers.

[108] A. Dsouza, "Experimental evolutionary optimization of geometric integrity in Fused Filament Fabrication (FFF) Additive Manufacturing (AM) process," State University of New York at Binghamton, 2016.

[109] Y. Zhang and K. Chou, "A parametric study of part distortions in fused deposition modelling using three-dimensional finite element analysis," *Proceedings of the Institution of Mechanical Engineers, Part B: Journal of Engineering Manufacture*, vol. 222, no. 8, pp. 959-968, 2008.

[110] T. Kanungo, D. M. Mount, N. S. Netanyahu, C. D. Piatko, R. Silverman, and A. Y. Wu, "An efficient k-means clustering algorithm: Analysis and implementation," *IEEE transactions on pattern analysis and machine intelligence*, vol. 24, no. 7, pp. 881-892, 2002.

[111] K.-B. Kim, D. K. Hsu, and D. J. Barnard, "Estimation of porosity content of composite materials by applying discrete wavelet transform to ultrasonic backscattered signal," *NDT & E International*, vol. 56, pp. 10-16, 2013.

[112] Y. Nikishkov, G. Seon, and A. Makeev, "Structural analysis of composites with porosity defects based on X-ray computed tomography," *Journal of Composite Materials*, vol. 48, no. 17, pp. 2131-2144, 2014.

[113] K. Tserpes, A. Stamopoulos, and S. G. Pantelakis, "A numerical methodology for simulating the mechanical behavior of CFRP laminates containing pores using X-ray computed tomography data," *Composites Part B: Engineering*, vol. 102, pp. 122-133, 2016.

[114] A.-M. Zelenyak, R. Oster, M. Mosch, P. Jahnke, and M. G. Sause, "Numerical Modeling of Ultrasonic Inspection in Fiber Reinforced Materials with Explicit Microstructure," in *Proc. 19th World Conference on Non-Destructive Testing, Munich, DGZfP*, 2016.

[115] H. Kim, K. C. Claffy, M. Fomenkov, D. Barman, M. Faloutsos, and K. Lee, "Internet traffic classification demystified: myths, caveats, and the best practices," in *Proceedings of the 2008 ACM CoNEXT conference*, 2008, p. 11: ACM.

[116] J. C. Clements, "Convexity-preserving piecewise rational cubic interpolation," *SIAM journal on numerical analysis*, vol. 27, no. 4, pp. 1016-1023, 1990.

[117] A. Razdan, "Knot placement for B-spline curve approximation," *Tempe, AZ: Arizona State University*, 1999.

[118] G. H. Teichert *et al.*, "A comparison of Redlich-Kister polynomial and cubic spline representations of the chemical potential in phase field computations," *Computational Materials Science*, vol. 128, pp. 127-139, 2017.

[119] G. Ralli, D. McGowan, M. Chappell, R. Sharma, G. Higgins, and J. Fenwick, "4D-PET reconstruction of dynamic non-small cell lung cancer [18-F]-FMISO-PET data using adaptive-knot cubic B-splines," in *Biomedical Imaging (ISBI 2017), 2017 IEEE 14th International Symposium on*, 2017, pp. 1189-1192: IEEE.

[120] J. O. Ramsay, *Functional data analysis*. Wiley Online Library, 2006.

[121] S. Geman, E. Bienenstock, and R. Doursat, "Neural networks and the bias/variance dilemma," *Neural computation*, vol. 4, no. 1, pp. 1-58, 1992.

[122] G. M. James, "Variance and bias for general loss functions," *Machine Learning*, vol. 51, no. 2, pp. 115-135, 2003.

[123] S. Mukkamala, G. Janoski, and A. Sung, "Intrusion detection using neural networks and support vector machines," in *Neural Networks, 2002. IJCNN'02. Proceedings of the 2002 International Joint Conference on*, 2002, vol. 2, pp. 1702-1707: IEEE.

[124] G. Stein, B. Chen, A. S. Wu, and K. A. Hua, "Decision tree classifier for network intrusion detection with GA-based feature selection," in *Proceedings of the 43rd annual Southeast regional conference-Volume 2*, 2005, pp. 136-141: ACM.

[125] K. Polat, S. Şahan, and S. Güneş, "Automatic detection of heart disease using an artificial immune recognition system (AIRS) with fuzzy resource allocation mechanism and k-nn (nearest neighbour) based weighting preprocessing," *Expert Systems with Applications*, vol. 32, no. 2, pp. 625-631, 2007.

[126] J. Im and J. R. Jensen, "A change detection model based on neighborhood correlation image analysis and decision tree classification," *Remote Sensing of Environment*, vol. 99, no. 3, pp. 326-340, 2005.

[127] B. Heisele, T. Serre, S. Prentice, and T. Poggio, "Hierarchical classification and feature reduction for fast face detection with support vector machines," *Pattern Recognition*, vol. 36, no. 9, pp. 2007-2017, 2003.

[128] R. Kohavi, "A study of cross-validation and bootstrap for accuracy estimation and model selection," in *Ijcai*, 1995, vol. 14, no. 2, pp. 1137-1145: Stanford, CA.

[129] S. Chowdhury *et al.*, "Botnet detection using graph-based feature clustering," *Journal of Big Data*, vol. 4, no. 1, p. 14, 2017.

[130] M. Mani, S. Feng, B. Lane, A. Donmez, S. Moylan, and R. Fesperman, *Measurement science needs for real-time control of additive manufacturing powder bed fusion processes*. US Department of Commerce, National Institute of Standards and Technology, 2015.

[131] P. Mercelis and J.-P. Kruth, "Residual stresses in selective laser sintering and selective laser melting," *Rapid Prototyping Journal*, vol. 12, no. 5, pp. 254-265, 2006.

[132] M. F. Zäh and S. Lutzmann, "Modelling and simulation of electron beam melting," *Production Engineering*, vol. 4, no. 1, pp. 15-23, 2010.

[133] M. Grasso, A. Demir, B. Previtali, and B. Colosimo, "In situ monitoring of selective laser melting of zinc powder via infrared imaging of the process plume," *Robotics and Computer-Integrated Manufacturing*, vol. 49, pp. 229-239, 2018.

[134] M. Grasso, V. Laguzza, Q. Semeraro, and B. M. Colosimo, "In-process monitoring of selective laser melting: spatial detection of defects via image data analysis," *Journal of Manufacturing Science and Engineering*, vol. 139, no. 5, p. 051001, 2017.

[135] R. Achanta, N. Arvanitopoulos Darginis, and S. Süsstrunk, "Extreme Image Completion," in *IEEE International Conference on Acoustics, Speech and Signal Processing (ICASSP)*, 2017, no. EPFL-CONF-224337.

[136] X. Shen, Y.-C. Chen, X. Tao, and J. Jia, "Convolutional Neural Pyramid for Image Processing," *arXiv preprint arXiv:1704.02071*, 2017.

[137] H. Lu, K. N. Plataniotis, and A. N. Venetsanopoulos, "MPCA: Multilinear principal component analysis of tensor objects," *IEEE Transactions on Neural Networks*, vol. 19, no. 1, pp. 18-39, 2008.

[138] L. Thijs, F. Verhaeghe, T. Craeghs, J. Van Humbeeck, and J.-P. Kruth, "A study of the microstructural evolution during selective laser melting of Ti–6Al–4V," *Acta Materialia*, vol. 58, no. 9, pp. 3303-3312, 2010.

[139] T. Craeghs, F. Bechmann, S. Berumen, and J.-P. Kruth, "Feedback control of Layerwise Laser Melting using optical sensors," *Physics Procedia*, vol. 5, pp. 505-514, 2010.

[140] T. Craeghs, S. Clijsters, E. Yasa, F. Bechmann, S. Berumen, and J.-P. Kruth, "Determination of geometrical factors in Layerwise Laser Melting using optical process monitoring," *Optics and Lasers in Engineering*, vol. 49, no. 12, pp. 1440-1446, 2011.

[141] E. Rodriguez, J. Mireles, C. A. Terrazas, D. Espalin, M. A. Perez, and R. B. Wicker, "Approximation of absolute surface temperature measurements of powder bed fusion additive manufacturing technology using in situ infrared thermography," *Additive Manufacturing*, vol. 5, pp. 31-39, 2015.

[142] C. Van Gestel, "Study of physical phenomena of selective laser melting towards increased productivity," PhD Dissertation, 2015.

[143] I. Yadroitsev, P. Krakhmalev, and I. Yadroitsava, "Selective laser melting of Ti6Al4V alloy for biomedical applications: Temperature monitoring and microstructural evolution," *Journal of Alloys and Compounds*, vol. 583, pp. 404-409, 2014.

[144] B. Lane, S. Moylan, E. P. Whitenton, and L. Ma, "Thermographic measurements of the commercial laser powder bed fusion process at NIST," *Rapid prototyping journal*, vol. 22, no. 5, pp. 778-787, 2016.

[145] J. A. Kanko, A. P. Sibley, and J. M. Fraser, "In situ morphology-based defect detection of selective laser melting through inline coherent imaging," *Journal of Materials Processing Technology*, vol. 231, pp. 488-500, 2016.

[146] A. Neef, V. Seyda, D. Herzog, C. Emmelmann, M. Schönleber, and M. Kogel-Hollacher, "Low coherence interferometry in selective laser melting," *Physics Procedia*, vol. 56, pp. 82-89, 2014.

[147] E. W. Reutzel and A. R. Nassar, "A survey of sensing and control systems for machine and process monitoring of directed-energy, metal-based additive manufacturing," *Rapid Prototyping Journal*, vol. 21, no. 2, pp. 159-167, 2015.

[148] J.-P. Kruth, P. Mercelis, J. Van Vaerenbergh, and T. Craeghs, "Feedback control of selective laser melting," in *Proceedings of the 3rd international conference on advanced research in virtual and rapid prototyping*, 2007, pp. 521-527.

[149] H. Krauss, T. Zeugner, and M. F. Zaeh, "Layerwise monitoring of the selective laser melting process by thermography," *Physics Procedia*, vol. 56, pp. 64-71, 2014.

[150] J. E. Craig, T. Wakeman, R. Grylls, and J. Bullen, "On-line imaging pyrometer for laser deposition processing," *Sensors, Sampling, Simul. Process Control*, pp. 103-110, 2011.

[151] S. Kleszczynski, J. zur Jacobsmühlen, B. Reinarz, J. T. Sehrt, G. Witt, and D. Merhof, "Improving process stability of laser beam melting systems," in *Fraunhofer Direct Digital Manufacturing Conference*, 2014.

[152] M. Mani, B. M. Lane, M. A. Donmez, S. C. Feng, and S. P. Moylan, "A review on measurement science needs for real-time control of additive manufacturing metal powder bed fusion processes," *International Journal of Production Research*, vol. 55, no. 5, pp. 1400-1418, 2017.

[153] T. G. Spears and S. A. Gold, "In-process sensing in selective laser melting (SLM) additive manufacturing," *Integrating Materials and Manufacturing Innovation*, vol. 5, no. 1, p. 2, 2016.

[154] M. Khanzadeh, S. Chowdhury, L. Bian, and M. A. Tschopp, "A Methodology for Predicting Porosity From Thermal Imaging of Melt Pools in Additive Manufacturing Thin Wall Sections," in *ASME 2017 12th International Manufacturing Science and Engineering Conference*, 2017, pp. V002T01A044-V002T01A044: American Society of Mechanical Engineers.

[155] H. Krauss, C. Eschey, and M. Zaeh, "Thermography for monitoring the selective laser melting process," in *Solid Freeform Fabrication Symposium*, 2012.

[156] J. Schilp, C. Seidel, H. Krauss, and J. Weirather, "Investigations on temperature fields during laser beam melting by means of process monitoring and multiscale process modelling," *Advances in Mechanical Engineering*, vol. 6, p. 217584, 2014.

[157] M. Khanzadeh, S. Chowdhury, M. A. Tschopp, H. R. Doude, M. Marufuzzaman, and L. Bian, "In-situ monitoring of melt pool images for porosity prediction in directed energy deposition processes," *IISE Transactions*, pp. 1-19, 2018.

[158] M. Khanzadeh, S. Chowdhury, M. Marufuzzaman, M. A. Tschopp, and L. Bian, "Porosity prediction: Supervised-learning of thermal history for direct laser deposition," *Journal of Manufacturing Systems*, vol. 47, pp. 69-82, 2018.

[159] T.-L. Chen, S.-Y. Huang, H. Hung, and I.-P. Tu, "An Introduction to Multilinear Principal Component Analysis," *Journal of the Chinese Statistical Association*, vol. 52, no. 1, pp. 24-43, 2014.

[160] Z. Zhou, J. Fang, L. Yang, H. Li, Z. Chen, and R. Blum, "Low-Rank Tensor Decomposition-Aided Channel Estimation for Millimeter Wave MIMO-OFDM Systems," *IEEE Journal on Selected Areas in Communications*, 2017.

[161] L. De Lathauwer, B. De Moor, and J. Vandewalle, "A multilinear singular value decomposition," *SIAM journal on Matrix Analysis and Applications*, vol. 21, no. 4, pp. 1253-1278, 2000.

[162] L. De Lathauwer, B. De Moor, and J. Vandewalle, "On the best rank-1 and rank-(r 1, r 2,..., rn) approximation of higher-order tensors," *SIAM journal on Matrix Analysis and Applications*, vol. 21, no. 4, pp. 1324-1342, 2000.

[163] H. Hung, P. Wu, I. Tu, and S. Huang, "On multilinear principal component analysis of order-two tensors," *Biometrika*, vol. 99, no. 3, pp. 569-583, 2012.

[164] R. A. Horn and C. R. Johnson, "Matrix Analysis Cambridge University Press," *New York*, 1985.

[165] G. I. Allen, "Regularized tensor factorizations and higher-order principal components analysis," *arXiv preprint arXiv:1202.2476*, 2012.

[166] H. Yan, K. Paynabar, and J. Shi, "Image-based process monitoring using low-rank tensor decomposition," *IEEE Transactions on Automation Science and Engineering*, vol. 12, no. 1, pp. 216-227, 2015.

[167] P. Nomikos and J. F. MacGregor, "Multivariate SPC charts for monitoring batch processes," *Technometrics*, vol. 37, no. 1, pp. 41-59, 1995.

[168] R. A. Johnson and D. W. Wichern, *Applied multivariate statistical analysis*. Prentice-Hall New Jersey, 2014.

[169] W. E. Frazier, "Metal additive manufacturing: a review," *Journal of Materials Engineering and Performance,* vol. 23, no. 6, pp. 1917-1928, 2014.

[170] J. Ge, J. Lin, Y. Lei, and H. Fu, "Location-related thermal history, microstructure, and mechanical properties of arc additively manufactured 2Cr13 steel using cold metal transfer welding," *Materials Science and Engineering: A,* vol. 715, pp. 144-153, 2018.

[171] M. Mahmoudi *et al.*, "Multivariate Calibration and Experimental Validation of a 3D Finite ElementThermal Model for Laser Powder-Bed Fusion Metal Additive Manufacturing," 2018.

[172] M. Mozaffar *et al.*, "Data-Driven Prediction of the High-Dimensional Thermal History in Directed Energy Deposition Processes via Recurrent Neural Networks," *Manufacturing Letters,* 2018.

[173] M. Mani, B. Lane, A. Donmez, S. Feng, S. Moylan, and R. Fesperman, "NISTIR 8036: Measurement Science Needs for Real-time Control of Additive Manufacturing Powder Bed Fusion Processes," NIST, Gaithersburg, MD2015.

[174] E. Popova, T. M. Rodgers, X. Gong, A. Cecen, J. D. Madison, and S. R. Kalidindi, "Process-Structure Linkages Using a Data Science Approach: Application to Simulated Additive Manufacturing Data," *Integrating Materials and Manufacturing Innovation,* vol. 6, no. 1, pp. 54-68, 2017// 2017.

[175] Q. Zhao *et al.*, "Higher order partial least squares (HOPLS): a generalized multilinear regression method," *IEEE transactions on pattern analysis and machine intelligence,* vol. 35, no. 7, pp. 1660-1673, 2013.

[176] T. G. Kolda and B. W. Bader, "Tensor decompositions and applications," *SIAM review,* vol. 51, no. 3, pp. 455-500, 2009.

[177] H. Kim, J. X. Zhou, H. C. Morse III, and H. Park, "A three-stage framework for gene expression data analysis by L1-norm support vector regression," *International journal of bioinformatics research and applications,* vol. 1, no. 1, pp. 51-62, 2005.

[178] M. Khanzadeh, W. Tian, A. Yadollahi, H. R. Doude, M. A. Tschopp, and L. Bian, "Dual process monitoring of metal-based additive manufacturing using tensor decomposition of thermal image streams," *Additive Manufacturing,* vol. 23, pp. 443-456, 2018.